Distribution Agreement

In presenting this thesis or dissertation as a partial fulfillment of the requirements for an advanced degree from Emory University, I hereby grant to Emory University and its agents the non-exclusive license to archive, make accessible, and display my thesis or dissertation in whole or in part in all forms of media, now or hereafter known, including display on the world wide web. I understand that I may select some access restrictions as part of the online submission of this thesis or dissertation. I retain all ownership rights to the copyright of the thesis or dissertation. I also retain the right to use in future works (such as articles or books) all or part of this thesis or dissertation.

Signature:

Ryan Freeman	Date

Electronic, Optical, and Microwave Studies of Nanomagnetic Systems

By
Ryan Freeman
Doctor of Philosophy
Physics

Sergei Urazhdin, Ph.D
Advisor

Alexander Kozhanov, Ph.D
Committee Member

Eric Weeks, Ph.D
Committee Member

Justin Burton, Ph.D
Committee Member

Hayk Harutyunyan, Ph.D
Committee Member

Accepted:

Lisa A. Tedesco, Ph.D.
Dean of the James T. Laney School of Graduate Studies

Date

Electronic, Optical, and Microwave Studies of Nanomagnetic Systems

By

Ryan Freeman
B.A. with Honors in Physics, Colgate University, 2013

Advisor: Sergei Urazhdin, Ph.D.

An abstract of
A dissertation submitted to the Faculty of the
James T. Laney School of Graduate Studies of Emory University
in partial fulfillment of the requirements for the degree of
Doctor of Philosophy
in Physics
2020

Abstract

This dissertation includes a variety of research projects focused on understanding and manipulating magnetic phenomena at nanoscale. These projects were experimentally driven, but also involve simulations and calculations in mostly a supplementary role. Most of my work is related in some way to the optical, electronic, or microwave generation of spin waves, the dynamical eigenmodes of spin precession that are present in magnetic materials. Future technological applications of spin waves would require the ability to efficiently generate and transport them in nanostructures. This long term technological goal underpins much of the research presented in this thesis.

One of the most common ways to generate spin waves in nanostructures is via the injection of spin angular momentum into a magnetic material, via 'spin currents' generated by various spin-orbit effects. The second chapter of my thesis includes research into the nanoscopic length scales over which spin currents are generated and dissipated. I was able to identify evidence for a previously unrecognized physical effect that contributes to the dissipation of spin currents in materials with large spin-orbit interaction. There is evidence that this spin relaxation mechanism could be the reason why Pt, a material with strong magnetic properties, never reaches a fully magnetic state. The third chapter includes research into the generation of spin waves excited by spin-polarized electrical currents, showing that when electrons scatter in magnetic materials, spin waves are generated in a quantum mechanical process that mirrors the process of photon generation in lasers. The fourth chapter shows the implementation of an anti-reflective coating that drastically increases the signal to noise ratio in common magneto-optical experiments used to study magnetic films excited in the 'ultra-fast' terahertz frequency range. The fifth chapter shows how nanoscale optical antenna can be used to spectroscopically probe high frequency, high wavevector spin waves that are inaccessible by free-space light. The sixth chapter shows experimental results on a recently discovered magneto-electronic effect that is the consequence of both spin-dependent electronic scattering and spin-orbit effects that are modified by the presence of spin waves. The seventh and final chapter includes research on the generation of spin waves in the nonlinear regime, where the damping of spin waves is fully compensated by the effects of spin currents.

Electronic, Optical, and Microwave Studies of Nanomagnetic Systems

By

Ryan Freeman

B.A. with Honors in Physics, Colgate University, 2013

Advisor: Sergei Urazhdin, Ph.D.

A dissertation submitted to the Faculty of the

James T. Laney School of Graduate Studies of Emory University

in partial fulfillment of the requirements for the degree of

Doctor of Philosophy

in Physics

2020

Acknowledgments

My PhD was in many ways the most solitary experience of my life so far. My experiences in grade school and undergrad were very much team-based, whether it was studying late at night with fellow classmates, or the extremely team based environments of my years as a football player. However, as a graduate student, most of my time was spent essentially by myself in a basement, reading physics, doing experiments, and coding. That is not to say that I was totally alone. In fact, because of the solitary environment, the influence of each person involved in my life during my PhD experience was profound.

I would first like to acknowledge my advisor Dr. Sergei Urazhdin. When I first came to Emory, I think I was a bit 'under-developed' academically, and Sergei still took me into his lab. He didn't get frustrated at my lack of experience (or at least he hid it well), but he still had high expectations that ultimately pushed me to treat each individual day as a precious opportunity to do science and become a better physicist. I'm also grateful for each of my committee members, who've each helped in their own way. I'd to thank my wife, Xinru Huang, whom I met at Emory. Xinru makes every day a joy, and without her my PhD would have gone from solitary to lonely. She is goofy and light-hearted, but she is also uncompromising and decisive. Her father once described her as his 'wild stallion', and her tenacity has rubbed off on me, as I had to choose to either become stronger or submit to her fiery will. I'd also like to thank all of my family: my siblings, cousins, aunts, uncles and grandparents, but especially my father, who instilled in me a love for science, physics specifically, from an early age.

During the course of my PhD, several students made day to day life possible. The chill vibes from my labmates Andrei, Guanxiong, and Dylan helped cool my intensity at times. Guga sometimes made Emory feel less foreign and more like the liberal arts environment that I came of age in during my undergrad at Colgate University. My college friends Sean, Nick, and Alex have always been a great sounding boards for whatever I've got going on in life. Skanda was my heavy metal buddy. He came to nearly countless metal shows with me, helping me viscerally expel the frustrations of the day and lose more than a little hearing along the way. Yannic, Mike, and Robert helped me learn that my athletic life can continue with Jiu Jitsu and Golf long after my Football career has ended. And I've gotta give a huge shout out to Joe Natale. I had a wrestling tournament at the reception to my wedding in 2018. One of my friends (who will go nameless) backed out of the tournament when he saw the intimidating muscle mass of his opponent. Joe essentially jumped out of his suit into athletic wear and was ready to go! He got his ass beat by a much larger opponent, but he fought bravely and nobly. The true spirit of a warrior. Bushido.

My PhD would have been impossible without the influence of all of these people, and the others that I've ashamedly forgotten to acknowledge here. But I also have to have to acknowledge myself. I'm not sure if it

was the PhD or just being a 20 something year old in America, but its been rough at times, and I hung in there. At my lowest points, when I most wanted to give up, that's when I held on the hardest and leaned into the punches. I know a lot of people that I've met in my life that would've either given up or accepted mediocrity if they were in my shoes. My advice to any incoming graduate students is to have faith in your future self. Even if you aren't 'good enough' when you first start grad school, there is enough time that if you commit and believe in yourself, you can get better every day and eventually accomplish quite a lot.

Contents

List of Figures

Citations to Previously Published Work

Chapter 2 contains research from one publication:

1. R. Freeman, A. Zholud, Z. Dun, H. Zhou, S. Urazhdin, "Evidence of Dyakonov-Perel-like Spin Relaxation in Pt" *Physical Review Letters* **120**, 067204, (2018)

Chapter 3 contains research from one publication:
2. A. Zholud, R. Freeman, R. Cao, A. Srivastava, S. Urazhdin, "Spin transfer due to quantum fluctuations of magnetization", *Physical Review Letters* **119**, 257201, (2017)

Chapter 4 contains research from one publication:
3. M. Pancaldi, R. Freeman, M. Hudl, M.C. Hoffmann, S. Urazhdin, P. Vavassori, S. Bonetti, "Anti-reflection coating design for metallic terahertz meta-materials", *Optics Express* **26**, 3, (2018)

Chapter 5 contains research from one article, submitted for publication:
4. R.Freeman, R. LeMasters, T. Kalejaiye, F. Weng, G. Chen, J. Ding, M. Wu, V. Demidov, S. Demokritov, H. Harutyunyan, S. Urazhdin, "Brillouin light scattering of spin waves inaccessible with free-space light", submitted to *Physical Review Letters*, (2020)

Chapter 7 contains research from two publications:
5. B. Divinskiy, V. Demidov, S. Urazhdin, R.Freeman, A. Rinkevich, S. Demokritov, "Excitation and Amplification of Spin Waves by Spin-Orbit Torque", *Advanced Materials*, (2018)
6. B. Divinskiy, V. Demidov, S. Urazhdin, R.Freeman, A.B. Rinkevich, S. Demokritov, "Controllable excitation of quasi-linear and bullet modes in a spin-Hall nano-oscillator", *Applied Physics Letters*, (2019)

Published work not included in this dissertation:
7. G. Chen, R. Freeman, A. Zholud, S. Urazhdin, "Observation of anomalous non-Ohmic transport in current-driven nanostructures", *Physical Review X*, (2020)

Chapter 1

Introduction: Crash Course in Magnetism

My goal for this section is to briefly introduce magnetism in a way that is digestible for new graduate students. This will not be a comprehensive text on all of the physics that underlies magnetic phenomena, as there are many great textbooks that do that much more effectively than I could [1, 16, 18–20]. However, those books are generally both massive and dense. In my graduate student career, I would find myself getting so focused on the details in a particular chapter of these textbooks that I would fail to see how the various models and effects came together to relate to my projects, or magnetism as a whole. I also personally feel that seeing phenomena explained with both mathematical rigor *and* linguistic analogies is essential for creating a working knowledge of a subject. For this reason, I've decided to organize this background section in a way that hopefully connects the dots between the fundamental physics of magnetism, and the magnetic systems that will be the focus of this thesis. I will first explain magnetism in individual atoms, then how magnetic ordering occurs in magnetic films. After working through the fundamentals of how magnetic ordering occurs, I will introduce the concepts of spin waves, the magnetic excitations that are central to much of this thesis, and conclude by discussing how spin waves are excited experimentally.

1.1 Magnetism in atoms

First and foremost, magnetic ordering is due to the alignment of the angular momentum of electrons. The angular momentum of electrons has generally two components, the orbital angular momentum $\vec{L}$ of electrons, due to their motion around the atom, and their intrinsic angular momentum, or spin, $\vec{S}$. The orbital angular

momentum of the electron is analogous to angular momentum as defined in classical mechanics: $\vec{L} = \vec{r} \times \vec{p}$, but with the classical position and momentum replaced with their quantum counterparts, the quantum operators $\hat{r}$ and $\hat{p}$. The spin of an electron has no classical counterpart. Both types of electronic angular momentum are quantized. In most cases, the orbital moment of an electron interacts significantly more strongly with other orbital moments than with spin moments and vice versa. Consequently, the total angular momentum of an ensemble of electrons can be written as $\vec{J} = \vec{L} + \vec{S}$, where $\vec{L} = \sum \vec{L}_i$, and $\vec{S} = \sum \vec{S}_i$, summing over all of the electrons in the ensemble. Orbital and spin angular momentum have different contributions to the total magnetic moment: $\mu_{total} = \mu_L + \mu_S$, shown by the scaling relationships: $\vec{\mu}_L = -g_L \mu_B \ \vec{L}/\hbar$ and $\vec{\mu}_S = -g_S \mu_B \ \vec{S}/\hbar$, where g_L and g_S are the Landé 'g' factors for orbital and spin angular momentum respectively, and μ_B is the Bohr magneton. These g factors are fundamental constants of nature, where $g_S \approx 2$ and $g_L = 1$. The difference between g_S and g_L results in the total magnetic moment and total angular momentum being generally non-collinear with one another. There exist various atoms, materials, and specially engineered nanostructures in which the magnetization is dominantly determined by $\vec{L}$, $\vec{S}$, or a combination of both.

As atoms become larger, the relativistic motion of the negatively charged electron with respect to the positively charge nucleus starts to have a significant impact on the relationship between $\vec{L}$ and $\vec{S}$ via the 'spin-orbit interaction' (SOI). The strength of SOI generally scales as Z^4, where Z is the atomic number. This can colloquially be explained from the perspective of the electron orbiting the nucleus. This electron 'sees' the positively charged nucleus orbiting itself. This loop of current is responsible for a magnetic field that can directly couple to the spin of the electron. The SOI acts as a channel by which orbital and spin angular momentum can influence each other, and is responsible for numerous magneto-electronic and optical effects that allow electric fields to directly influence spin dynamics.

Now that we have introduced the concept of magnetic moments, we can explain how net magnetic moments develop in the electrons orbiting an atom. An 'electronic state' can be uniquely defined by its quantum numbers: n (energy level), l (orbital angular momentum), m_l (projection of l along any arbitrarily chosen 'quantization axis'), and m_s (projection of the spin along the quantization axis). Electrons that share the same n, are said to share the same 'shell'. Electrons that share the same n and l are said to share the same 'sub-shell'. Electrons that share the same n l and m_l share the same 'orbital'. Because of the Pauli exclusion principle, no two electrons can share the exact same electronic state. Consequently electrons in the same orbital must have oppositely directed spins.

The empirical 'Hund's rules' explain how electrons are usually organized into different orbitals as the number of electrons orbiting an atom increases. A more rigorous and detailed description can be found in various magnetism and chemistry textbooks [1, 18], with numerous caveats, but the essence of the rules is

m_l	:	2	1	0	-1	-2	2	1	0	-1	-2
m_s	:	↑	↑	↑	↑	↑	↓				
		spin-up states					spin-down states				
		$J = \|L - S\|$					$J = L + S$				

Figure 1.1: Occupation of electronic orbitals for an isolated Fe^{2+} ion, following Hund's rules. Table recreated from [1].

that each orbital in a subshell is singly occupied before accepting a second electron, and the electrons in the different orbitals tend to maximize the sub-shell's total spin and total orbital angular momentum. This is a consequence of the powerful Coulomb repulsion that makes it energetically favorable to spread electrons far apart. This combination of Coulomb repulsion and Fermi statistics is described energetically as the 'exchange interaction'. The total angular momentum of the shell is given by $J = |L - S|$ for shells less than half filled and $J = |L + S|$ for shells more than half filled. An example is shown in figure 1.1 for the 3d shell of the magnetic ion Fe^{2+}, making the wordy explanation above simpler to understand. In this example, the electrons in the 3d shell of Fe^{2+} have a total spin of $S = 5 \cdot \frac{1}{2} - \frac{1}{2} = 2$ and a total orbital angular momentum of $L = 2+1+0-1-2+2 = 2$, resulting in a net magnetic moment. Hund's rules predict L=0 for half-filled sub-shells, and consequently spin-orbit effects stemming from $L \cdot S$ vanish. For instance, the spin Hall effect, in which spin-orbit effects promote spin dependent electron motion, is significant in Pt which has a finite L in the 5d shell, whereas the spin Hall effect is negligible in Au, due to the exactly half-filled 5d sub-shell. When an electronic sub-shell is totally full, it has no net magnetic moment.

1.2 Magnetism in solids

When individual atoms are brought together, for instance, due to bonding between electrons in outer shells, the Pauli exclusion principle prevents multiple electrons from existing in identical electronic states. If we consider two atoms combining together to form a molecule, the result is each electronic orbital splitting into two orbitals of slightly different energies. If a large number, N, of atoms are bonded together to create a crystalline solid, then the electronic orbitals are split into N sublevels. In the case of macroscopic solids N$\approx 10^{19}$, and these 10^{19} different sublevels can be approximated as a continuous band of allowable electronic energies, as shown schematically in figure 1.2. There are separate electronic bands for majority and minority electrons.

Figure 1.2: When N atoms are brought together, the distinct electronic orbitals split into N sublevels. When N is large, the sublevels can be approximated as a continuous 'band' of allowable energy levels

In many crystalline solids, electronic bands remain partially filled, and consequently the electrons in these bands exhibit magnetic moments, as predicted by Hund's rules for isolated atoms. However, Hund's rule are more of a rule of thumb than an exact predictor of how magnetism arises in solids. There are a number of more realistic and complex models for how magnetic order arises in solids [1, 18, 21]: the Weiss mean-field model, the Heisenberg/Ising model, and the Stoner model. The Stoner model is a useful model for new students to learn, and can be thought of as an extension of Hund's rules for electronic bands.

In the discussion about Hund's rules, I noted that Coulomb repulsion and Fermi statistics combined to create the 'exchange interaction' which results in electron spins aligning, and electrons spreading out into different orbitals. In crystalline solids, there are no longer degenerate orbitals for the exchange interaction to 'push' electrons into. Instead there exist electronic states, with uniquely defined kinetic energies and wavevectors, and a 'density of states' (DOS). The DOS is essentially the number of different electronic states available to an electron at a particular energy level. These electronic states are generally filled up to the 'Fermi energy'.

In the limit of infinite DOS, the exchange interaction can be easily satisfied and minority (spin-down) electrons at the Fermi energy can be 'pushed' into majority (spin-up) states without paying any energy penalty, spin polarizing the electrons in the band [18]. In the opposite limit of very low DOS, the only available states that the exchange interaction can 'push' spin-down electrons into have higher kinetic energies, increasing the total energy of the system. Consequently, the electron band is not spin polarized. This is schematically depicted in figures 1.3. The Stoner model accounts for the competition between the exchange energy and the kinetic energy of the band electrons, quantitatively characterized as the Stoner Criterion for

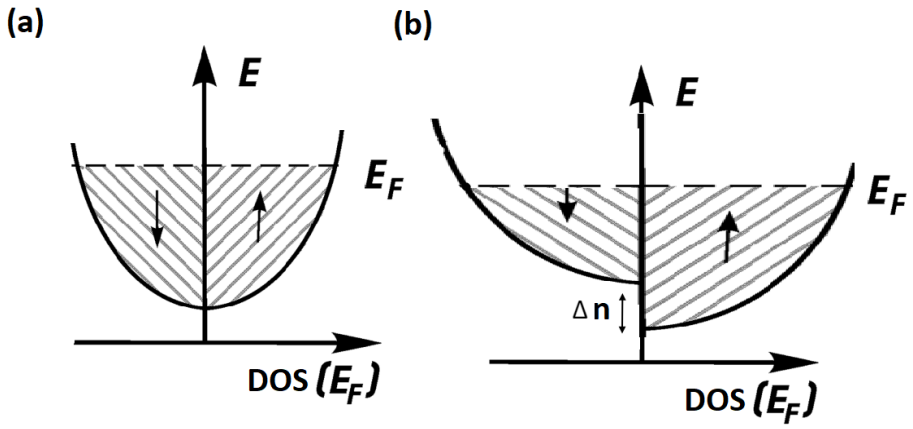

Figure 1.3: (a) In a nonmagnetic material, the spin up and spin down bands are equally filled, due to the kinetic energy penalty induced when a minority spin electron is placed in the majority spin band. (b) When the density of states becomes large, the exchange interaction promotes magnetic ordering. The area under the curves from $E = 0$ to $E = E_F$ determines the total number of electrons in each spin sub-band. The difference between the total number of spin up and spin down electrons determines the spin polarization of the band.

ferromagnetic ordering: $J_{ex}(E_F) \cdot \mathrm{DOS}(E_F) > 1$. When the exchange energy dominates over the increased energy due to increasing the number of electrons in the spin-up band, then magnetic ordering is energetically favorable. Different electron bands have different DOS, and crystalline solids with different inter-atomic separations have different exchange constants J_{ex}. When inter-atomic spacing is small, the Coulomb energy saved by aligning spins is negligible and the exchange energy promotes anti-ferromagnetic ordering $J_{ex} < 0$. As inter-atomic spacing increases, there is a Coulomb energy reward for ferromagnetic ordering $J_{ex} > 0$. At large inter-atomic separations, the Coulomb interactions between electrons are totally negligible and $J_{ex} \to 0$. This is captured by the Bethe-Slater curve, shown in figure 1.4, which successfully predicts the magnetic ordering of 3d transition metals. Often the Stoner Criterion determines the type of magnetic ordering, while the magnitude of the magnetization is well predicted by Hund's rules. For instance, Ni has a much lower magnetization than Fe. Unfortunately (or fortunately, depending on who you ask), magnetism is a complicated phenomena, and these basic models and rules of thumb sometimes fail to simply explain magnetic ordering in practical materials.

1.3 Magnetic ordering: anisotropy and domains

Now that I have introduced magnetism in atoms and bulk crystalline materials, I will briefly discuss how magnetic electrons' spins are spatially oriented. In magnetic materials, there are many different types of energetic interactions that depend on the orientations of the electrons' spins with respect to other vector directions: such as other electron's spins, external magnetic fields, or interfaces between different materials.

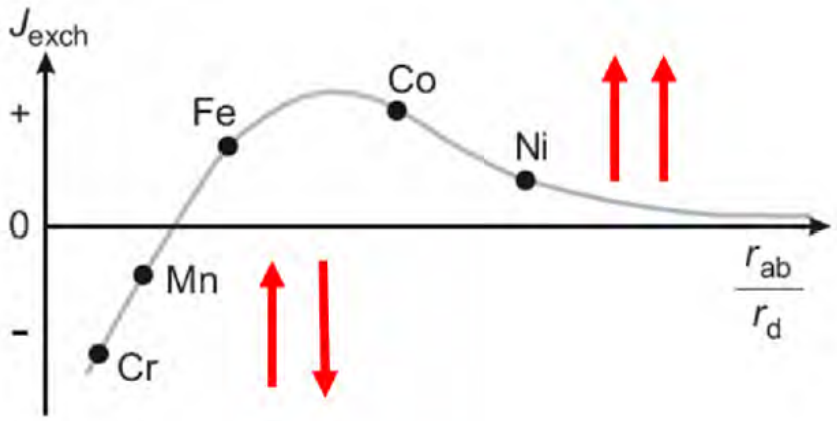

Figure 1.4: Bethe-Slater curve depicting the value of the exchange constant as a function of the inter-atomic spacing in crystalline transition metals, where r_ab is the interatomic distance and r_d is the radius of the 3d electron shell responsible for magnetism, reproduced from [2]

The vector nature of these interactions suggest a certain orientation of spin alignment that minimizes the magnetic energy. This relationship between the direction of magnetic orientation and energy is described as magnetic anisotropy. I will list a few of the prominent magnetic interactions that lead to anisotropy here [18]. The exchange interaction, which was described above, promotes ordering (parallel or anti-parallel) alignment between neighboring spins. Magnetocrystalline anisotropy is a consequence of the spin-orbit interaction, and promotes the alignment of magnetic spins along certain crystal axes. The magnetostatic energy can be thought of as a self-energy, due to the interaction between spins in some region of the magnetic material with the magnetic field surrounding spins in other regions of the material, making this effect strongly dependent on the geometry of the magnetic material. The Zeeman energy promotes anti-parallel alignment between the magnetic spins and an external magnetic field. The spin-orbit interaction also leads to two other interactions that are generally less common than the above mentioned energies, but are relevant in certain systems with large spin-orbit interaction. Magnetoelastic energy is the relationship between strain in a material and the direction of magnetization. And finally, the Dzyaloshinskii-Moriya Interaction (DMI) is a generally weak interaction that promotes chirality between neighboring electron spins, allowing for the tilting of spin orientation and in some cases spin vortices [22, 23].

The spins in a magnetic material will rotate to accommodate these different energetic interactions and minimize the total energy, resulting in an equilibrium magnetic configuration. The most common equilibrium magnetic configuration for ferromagnetic materials is generally the formation of 'magnetic domains', microscopic regions in which all magnetic spins are aligned. Some common magnetic domain configurations are shown in figure 1.5. However, there are numerous types of equilibrium configurations that are relevant in

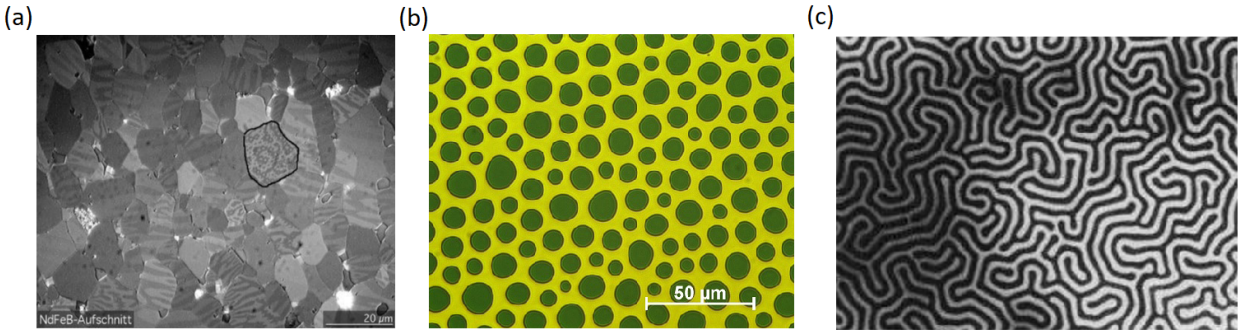

Figure 1.5: Images taken from various magneto-optical techniques [3, 4] depicted different common magnetic domain configurations, where different colors correspond to different directions of magnetization. The structure of the equilibrium magnetic configuration is a result of competition between different types of magnetic energetic interactions.

different cases when one or more of the magnetic interactions described above are dominant over others. For instance, in magnetic thin films present in the majority of the projects described in this thesis, the magnetostatic energy usually minimized when the net magnetization is aligned in the plane of the film. However, some specially engineered systems can exhibit out of plane magnetic anistropy [24], magnetic vortices [25], long, narrow, and winding 'labyrinth' domains [26, 27], and there are even some cases in which these magnetic interactions are in conflict with one another, and the magnetic system is said to be 'frustrated', with no well defined equilibrium state [28, 29].

1.4 Spin Waves

I have now introduced the building blocks that describe how magnetic ordering occurs in magnetic materials. However, the spins in the magnetic materials are not frozen in time into the magnetic domains described in the previous section. Even a single spin in the presence of a magnetic field will evolve as a function of time, precessing around the local magnetic field as a consequence of conservation of angular momentum according to the Landau-Lifshitz torque equation [1, 5, 30]: $\frac{-1}{\gamma}\frac{d\vec{M}}{dt} = \vec{M} \times \vec{H}_{eff}$, where γ is the gyromagnetic ratio, $\vec{M}$ is the magnetization, and $\vec{H}_{eff}$ is the local effective magnetic field. This precession is known as Larmor precession. However, the spatial and temporal evolution of spins in magnetic materials is more complex than simple Larmor precession, due to the energetic interactions between the spins described in the last section. This coupling between spins creates certain 'dynamical eigenmodes' that describe the allowed frequencies at which spins can precess around the local magnetic field, and the amount by which the precession phase of a spin lags behind each neighboring spin. These eigenmodes are called spin waves, where the wavelength is defined as the periodic distance at which the phase of precession repeats, as shown schematically in

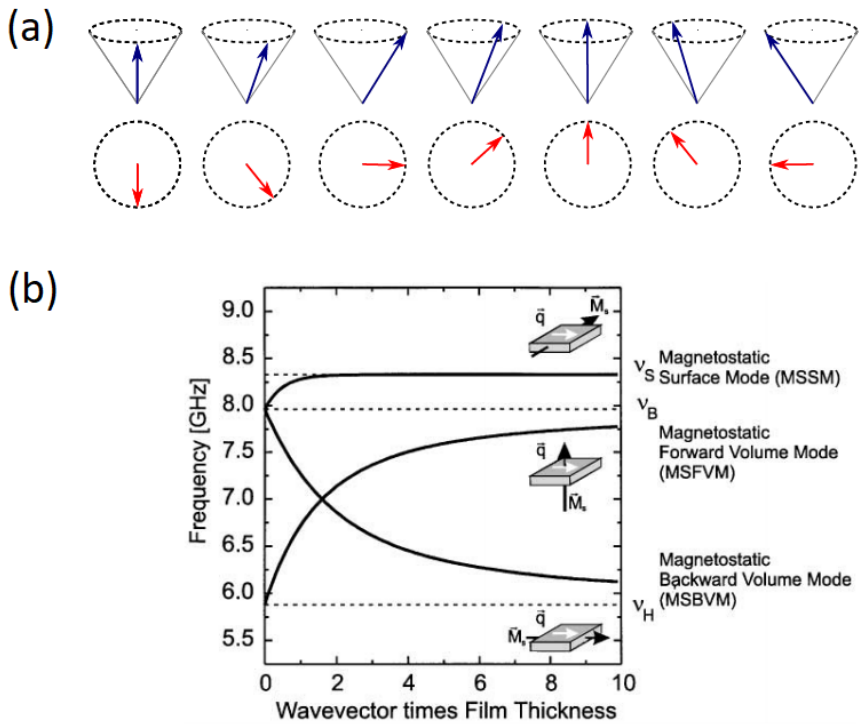

Figure 1.6: (a) Schematic depicting spin waves, the periodic oscillation of the phase of precession of spins around a magnetic field. (b) The dispersions (frequency vs wavevector) of three common spin wave modes, as labeled. Figure recreated from [5]

Fig. 1.6(a). The spatial and temporal evolution of spins in magnetic materials can generally be described as linear superpositions of different spin wave modes.

I will now discuss briefly the spectral properties of the spin wave modes excited in thin magnetic films. There exist three common types of spin wave modes corresponding to different orientations of the magnetic field with respect to the film. These modes have well defined dispersions [1, 5] (the relationship between the spin wave frequency and wavevector), as shown in Fig. 1.6(b). The Magnetostatic Forward Volume Mode can be excited if the magnetization is tilted out-of-plane. The other two modes are excited when the magnetization lies in the plane of the sample. The Damon-Eschbach mode, or Magnetostatic Surface Wave mode, can be excited when the spin wave wavevector, and the magnetization of the film are perpendicular to each other. The third mode, the Magnetostatic Backwards Volume Mode, is characterized by a negative group velocity with respect to the wavevector, and excited when the magnetization and wavevector are collinear. The presence of these two modes for in-plane magnetized films results in a spin wave dispersion manifold, with the frequency being related to angle between the magnetization and the wavevector by the

following expression:

$$f_{sw}(k,\phi) = \sqrt{(\gamma(B + 4\pi MAk^2) + \gamma 4\pi M(1 - (1 - e^{-kd}/kd)))} \cdot \sqrt{\gamma(B + 4\pi MAk^2) + \gamma 4\pi M(1 - e^{-kd}/kd)sin^2\phi)}, \quad (1.1)$$

where d is the magnetic film thickness, $\gamma = 2.8 \times 10^6$ Hz/Oe is the gyromagnetic ratio, A is the exchange constant, k is the wavenumber, ϕ is the angle between the wavevector $\vec{k}$ and the external field, M is the magnetization, and B is the magnetic flux density. The special case of k=0 defines the uniform precession mode, or ferromagnetic resonance mode (FMR), where all of the spins in the magnetic films precess coherently (in-phase).

At low wavevectors, the spin wave dispersion is predominantly determined by the long range magnetostatic, or dipolar interaction, and at high wavevectors, the dispersion is primarily determined by the short range exchange interaction. Consequently, low wavevector spin waves are often called dipolar spin waves, and high wavevector spin waves are often called exchange spin waves. As magnetic materials are confined to nanoscale, the reflection of spin waves from the interfaces results in standing waves in the direction of confinement [30], with discrete allowed wavevectors $k = n \cdot \pi/d$, where d is the thickness in the confined direction. For thin films, this means that the out of plane wavenumber is quantized, while the allowed in-plane wavevectors are continuous. For magnetic nanowires, the wavenumber in both confined directions is quantized, and similarly for nanodots, the wavenumbers of spin waves excited are quantized in all three directions.

In the GHz to THz frequency range the electromagnetic spectrum (photons), strongly couple with the spins in a magnetic medium, with the result being a 'magnon', the term for the quanta of spin waves. In this language, the number of magnons is equivalent to the square of the amplitude of the spin wave. The strong coupling between the electromagnetic spectrum and the spin wave spectrum allows for spin waves in nanomagnetic devices to be resonantly excited by either macroscopically large microwave fields, or local microwave fields generated by nanoantenna excited at microwave frequencies. The reciprocal is also true, and allows magnons to be used as sources of microwave radiation in nanomagnetic devices.

However, even in the absence of external exciting microwave fields, spin waves at frequencies allowed by the spin wave spectrum are generally present in magnetic materials. In a magnetic film at equilibrium, without any external driving, the spins in the film fluctuate around the direction of the equilibrium magnetization, due to the presence of thermal energy and the magnetic interactions between spins described above. One can think of the spin wave excitations as a channel into which thermal energy is dissipated. These seemingly random thermal fluctuations of spins can actually be decomposed into a distribution of incoherent

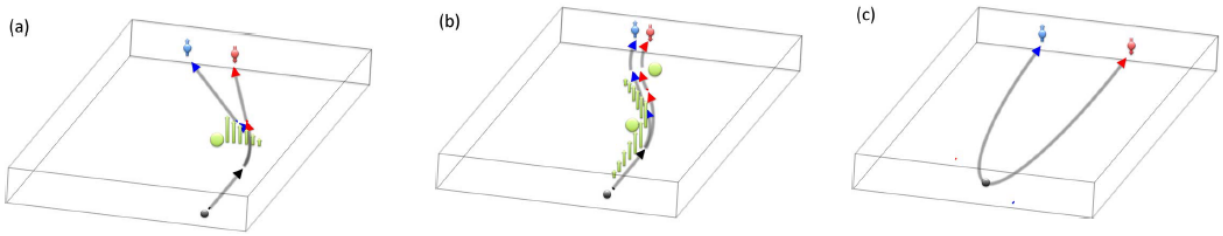

Figure 1.7: Schematics depicting different mechanisms of the spin Hall effect, recreated from [6]. (a) and (b) represent the 'skew scattering' and 'side-jump' mechanisms respectively. These two mechanisms are considering 'extrinsic', due to their occurrence during electron scattering events. (c) represents the 'intrinsic' spin Hall effect, occurring in the absence of scattering, as a result of electron band structure.

magnons of different frequencies (i.e. different spin waves with no phase relationship between each other). The frequency distribution of these incoherent magnons is generally well described by the Bose-Einstein distribution, $n(f) = 1/(e^{\hbar 2\pi f/k_b T} - 1)$, where the allowed frequencies f are defined by the spin wave spectrum. The bosonic nature of magnons is a reminder that magnons are hybridizations between photons and electron spins. One interesting consequence of this bosonic nature is that under the right experimental conditions, magnons can be pumped into a 'Bose-Einstein condensate', i.e. a large population of coherent (in-phase) magnons at the lowest frequency allowed by the spin wave spectrum [31].

There are long-term technological goals underpinning the investments into research in nanomagnetic phenomena and spin waves. The field of 'spintronics' is based around technological applications mirroring the paradigms of electronics, but focused on manipulating the spin of the electron instead of its charge [32] . Some 'spintronics' applications have already been realized. The most well known application is magnetic memory, a ubiquitous and society transforming application that has almost been made obsolete to regular technology consumers by the more modern flash memory. However, major technology companies are still investing in magnetic memory, using effects studied in academic research labs and combining them with existing technologies to make magnetic memory more robust, quicker, and more information dense. Generally, there is hope that the study of nanomagnetic phenomena, and specifically the manipulation of spin waves can have an influential effect on information processing technologies of the future.

The success of any future technologies based upon spin waves would be critically linked to the ability to efficiently generate large amplitude, long-living, far-traveling spin waves. Experimentally, one of the most common modern approaches to creating large amplitudes of spin waves is by increasing the amplitude of thermal magnons by a particular spin-orbit effect, the spin Hall effect (SHE) [6, 32–35]. The SHE is manifest as currents of electron spins (spin currents) propagating in directions perpendicular to electrical currents. The SHE occurs when electrical current is driven through materials with large spin-orbit coupling, predominantly materials with large atomic numbers, for example, from the platinum group in the periodic table. There are

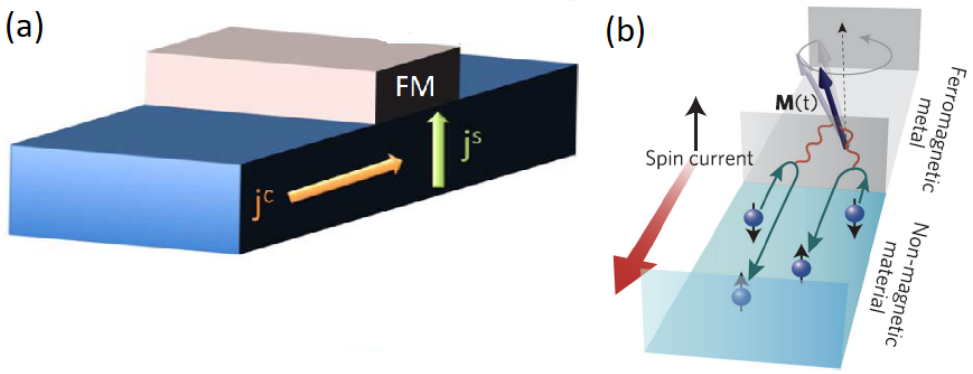

Figure 1.8: Schematics depicting two common implementations of the spin Hall effect in nanomagnetic devices, recreated from [6, 7]. (a) depicts normal metal/ ferromagnet bilayers, where the SHE drives spin current into the magnetic element, exciting spin waves. (b) depicts the reciprocal effect, 'spin pumping', where spin angular momentum from spin waves in a magnetic element is pumped into the normal metal.

numerous mechanisms by which the SHE occurs, some occurring during the process of electron scattering (extrinsic mechanisms), while others occur as electrons propagate, in between scattering events (intrinsic mechanisms). The SHE is commonly implemented experimentally by driving electrical current through bilayers of a material exhibiting large SOC, and a magnetic material in which the spin waves are to be excited. The result is angular momentum driven into the magnetic film, enhancing the amplitude of the spin waves present in the film. There is a large field of research based around understanding the mechanisms by which the SHE occurs, the length scales over which it develops, and methods to enhance its strength. The transfer of angular momentum from the SO material into the magnetic material, a process known as spin-transfer, is also an active area of research. Some open questions are technical and detail oriented, while others are suprisingly basic and fundamental, such as the role of energy conservation in the generation of spin waves (an ongoing area of research in the Urazhdin lab). There is also research on the reciprocal process of spin transfer, known as spin pumping, in which spin waves in a magnetic material interfaced with a SO material decay into spin and electrical currents in the SO material.

I've now explained the foundations of how magnetic ordering occurs in magnetic materials, the dynamical eigenmodes of spin motion in magnetic materials, known as spin waves, and the common electronic and microwave methods used to excite them. This sets the backdrop for my thesis research. My thesis research was primary experimental, with simulations, modeling, and calculations used supplementally to quantify specific effects, validate experimental results, or specific approximations used in analysis. The experimental work involved a variety of electromagnetic techniques, operating at various frequencies. The low frequency range of kHz, sometimes considered the DC limit in electromagnetics research, was primarily used to drive electrical currents in nanoscale electrical circuits. The microwave frequency range was used to resonantly

excite spin waves and characterize magnetic materials. At these frequencies, the magnetic field of electromagnetic radiation (light) strongly interacts with the spins in the magnetic material. I was also involved in projects based on THz and optical (100s of THz) excitation of magnetic systems, where the electric field of light weakly couples to the spins in the magnetic system via the spin-orbit interaction.

The second chapter of my thesis discusses a project that was a part of a general research direction related to studying how spin currents can be generated and how they dissipate. I was the primary author of this work, published in Physical Review Letters [36]. The project was focused on the mechanisms by which spin polarization decays in the archetypal spin-orbit material Pt. I was able to show that the current understanding of spin relaxation in Pt (and spin-orbit materials in general) is incomplete, and proposed a specific mechanism by which spin polarization can relax. The results may also explain why Pt exhibits strong magnetic correlations, but never fully transitions into a ferromagnetic state.

The third chapter of my thesis discusses a project in which I was involved, also published in Physical Review Letters [37], that focused on the transfer of spin angular momentum into magnetic materials (spin-transfer) by low frequency (kHz) electrical current. To contextualize, in much of the modern magnetism research community, the process of spin-transfer is approximated semi-classically, as 'spin-torque'. In this work, we showed that a significant component of the spin-transfer process is related to zero-point, quantum fluctuations of spin, which cannot be approximated as a classical torque. In a direct analogy to process of lasing, we show that spin transfer can be thought of as the stimulated and spontaneous generation of magnons in magnetic materials.

The fourth chapter of this thesis discusses a project in which I was involved that is closer to engineering than the fundamental physics of the first two chapters. In this work, published in the journal Optics Express [38], we showed the application of an anti-reflective coating used to dramatically enhance the signal to noise ratio of magneto-optical pump-probe experiments in which microscale Au THz antennae are used to localize electromagnetic energy into nanomagnetic films, and drive ultra-fast demagnetization. The inherently low signal to noise in these experiments is due to the fact that the Au antennae are significantly larger and more reflective than the nanomagnetic element. This problem is overcome by covering the Au THz antennae with an α-Si coating that decreases the optical reflection from the antenna, without perturbing the effects of the THz pulse on the magnetic element.

The fifth chapter features another project that I was the primary author of. In this chapter, I show how nanoscale metallic antenna placed on top of magnetic films can be used to facilitate light scattering from magnons that are 'invisible' to free-space light. In standard light scattering experiments, conservation of momentum makes all but the lowest frequency magnons inaccessible due to the small momentum of free-space light. In this work, I show experimentally and with calculations how the nanoscale metallic

antennae act to create local electric fields with large momentum components, allowing scattering from large wavevector magnons 'invisible' to free-space light. We analyze the effects of the antenna geometry, but the basic effect is robust and not dependent on carefully chosen geometries. In fact, similar nano-antenna can be easily implemented in other light-matter applications limited by conservation of momentum, such as light scattering from phonons and excitons, or solar power generation. As of the time of this writing, a manuscript based on this project is being reviewed at Physical Review Letters.

The sixth chapter of the thesis features unpublished work investigating the mechanisms responsible for a newly discovered magneto-electronic effect known as Unidirectional Magnetoresistance (UMR). There have been various explanations for the effect published, some based on the excitation of spin waves, and others based on spin-dependent electron scattering. This thesis chapter shows experiments that I performed in which I suppressed the amplitude of spin waves in nanomagnetic devices to separately analyze the contributions of the 'spin wave' and 'electronic' mechanisms to the UMR effect.

The seventh and final chapter of my thesis features work that I was a contributing author to, in which we studied the generation of spin waves by current in the nonlinear regime [39, 40]. In this high current regime, spin transfer totally compensates for magnetic damping, allowing for the generation of large amplitude spin waves with unique properties. I discuss work focused on the spectral characteristics and time evolution of these 'nonlinear spin wave modes', as well as a device with the noteworthy ability to launch the nonlinear spin waves along a waveguide.

1.5 Suggested Textbooks

For the benefit of future students, I will briefly suggest a handful of textbooks that were very helpful during my PhD research. I think these texts are approachable and well-written. "Modern Magnetic Materials" by Robert O'Handley [18], "Quantum Theory of Magnetism" by Nolting and Ramakamth [21], "Spin Waves: Theory and Applications" by Stancil and Prabhakar [1], and "Spin Wave Confinement" by Sergej Demokritov [30] are great resources on magnetic phenomena and materials. "Principles of Nano-Optics" by Lukas Novotny and Bert Hecht [41], "Plasmonics: Fundamentals and Applications" by Stefan Maier [42], and "Introductory Quantum Optics" by Christopher Gerry and Peter Knight [43] are great textbooks on nanoscale optical phenomena. The massive literature review "Spintronics: Fundamentals and applications" by Igor Zutic, Jaroslav Fabian, and Das Sarma [44] is essentially a textbook and explains spin-orbit effects very well.

Chapter 2

Spin Relaxation in Pt - Evidence for Undiscovered Spin Relaxation Mechanism

2.1 Motivation and background on spin-orbit effects

The interplay between the electron's motion and its spin, due to the spin-orbit interaction (SOI), opens unprecedented opportunities for the control of both spin and orbital degrees of freedom [32, 45–48]. For instance, the spin Hall effect (SHE) results in generation of pure spin current [49], enabling electronic control of magnetization in metallic and insulating nanomagnets [34, 50, 51]. Recent studies of materials that exhibit large SOI, including Pt, Ta, W, topological insulators, and alloys such as CuBi, have focused on identifying the SOI mechanisms, and characterizing the relevant parameters, including the spin-orbit scattering rates, the spin Hall angle, and the effective spin-orbit field [52–59]. Another relevant parameter is the spin diffusion length, λ, defined as the length scale for the relaxation of spin polarization away from its source. The value of λ is determined mostly by SOI. It is also the length scale for spin current generation via the SHE, and is thus directly related to SHE efficiency.

Pt is one of the most extensively studied spin-orbit materials, thanks to the large SOI effects [52, 60, 61], and relatively low resistivity minimizing Joule heating and current shunting in heterostructures. Parameters relevant to SOI in Pt such as the spin Hall angle and λ have been studied by a variety of techniques [52, 56, 60, 62–64]. Nevertheless, the values and the mechanisms controlling them are still debated. In particular,

the reported values of the spin Hall angle, defined as $J_e = \Theta_{SH} J_S$, or the ratio of spin current generated by a given electrical current, has been reported for a large range in Pt, from 0.004 to over 0.1 [52, 56, 65], and those of λ range from less than 1 nm to over 10 nm [52, 56, 60, 62–64, 66–68]. Such a large spread of the reported characteristics makes it challenging to establish the mechanisms controlling the spin-orbit effects.

In this work, we report a study of the temperature-dependent magnetoresistance in nanopillar spin valves with Pt spacers, and demonstrate that this approach can be utilized to elucidate the mechanisms of spin scattering in Pt and at its interfaces, and to characterize the relevant spin-orbit parameters. The dependence of magnetoresistance on the Pt spacer thickness allowed us to determine the value of λ and extract the spin lifetime. The observed temperature dependence indicates that at room temperature, spin relaxation in the studied Pt films is dominated by the Elliott-Yafet (EY) scattering, while at cryogenic temperatures it is dominated by intrinsic spin dephasing that can be attributed to the presence of an effective spin-orbit field. We also demonstrate that spin relaxation is suppressed in a thin Pt layer interfaced with a ferromagnet, consistent with the competition between the effective spin-orbit field and the proximity-induced exchange field in Pt.

2.2 Interfacial spin-orbit effects

One of the main difficulties in analyzing SOI is posed by the interplay between interfacial and bulk effects. As Wolfgang Pauli famously stated, "God made the bulk, surfaces were invented by the devil." Numerous studies investigating spin-orbit effects are complicated by the requirement of accurately modeling spin dynamics near interfaces between different materials. For instance, measurements of λ based on the spin absorption efficiency are affected by the spin relaxation at the interfaces [63].

The most ubiquitous interfacial spin-orbit effect is the Rashba effect. The Rashba can be thought of as a direct consequence of broken inversion asymmetry and spin-orbit coupling. Qualitatively, the Rashba effect can be explained as a consequence of the different atomic numbers for two adjacent materials, which leads to an electric potential across the interface. As conduction electrons travel near the interface, the electric potential is transformed relativistically into an effective magnetic field [69]. This Rashba field directly influences spin dynamics of conduction electrons. The strength of the Rashba field decays away from the interface, but many standard nanoscale spintronic devices are small enough for the Rashba field to be comparable or even stronger than the effects of bulk spin-orbit interaction. The Rashba field strongly affects the magnitude of the SHE in spintronic nanostructures, and makes a determination of the bulk spin diffusion length, λ, difficult.

Another relevant type of interfacial spin physics is proximity magnetization. A material interfaced with

a magnetic material experiences the effects of the exchange interaction of the magnetic material over the length scale defined by the magnetic correlation length [13]. If the neighboring material is paramagnetic, it can become magnetized over this length scale. Furthermore, spin-orbit effects at interfaces with ferromagnets may be affected by the temperature-dependent contribution from the proximity-induced magnetism [70].

There are several other effects that result in spin dynamics near interfaces. One of which is interface transparency, a result of Zeeman energy: $\vec{s} \cdot \vec{B}$, where $\vec{s}$ is the spin of the conduction electron and $\vec{B}$ is the magnetic field. When a nonmagnetic material is in contact with a magnetic material, there is a Zeeman energy barrier that conduction electrons from the nonmagnetic material must overcome to pass into the magnetic material. This leads to a different transmission probability for majority and minority conduction electrons. For instance, the apparent spin Hall angle in a SHE/ferromagnet bilayer depends on the transparency of their interface [65, 71, 72].

There is also the effect known as spin memory loss, where the spin of the conduction electron is transferred directly to the lattice via SOC when perturbed by the energy barrier at the interface. Technically, this is Elliott-Yafet (EY) spin relaxation that occurs from scattering at an interface. EY scattering will be described in more detail in a later section. Spin memory loss is relevant for magnetic and non-magnetic interfaces alike. Sometimes, the terms spin memory loss and spin transparency are used interchangeably in literature, but they are two separate effects.

Finally, there is the precession around the magnetic fields present at interfaces. The magnetic field can be a consequence of the Rashba effect, as described above, or from the presence of an adjacent magnetic material. All of these interfacial effects have been modeled together in what is known as the spin mixing conductance, or magnetoelectronic circuit theory [73–75]. This theory has made it easier to account for each of these interfacial effects, but due to the many parameters required to accurately model them, it is difficult to integrate into experimental analysis of spin transport.

2.3 Measurement technique: Giant Magnetoresistance

The original aim of this project was to clarify the value of the bulk spin diffusion length, λ, in Pt using a method that could clearly isolate the bulk spin transport effects from the interfacial effects described above. The approach that we used can unambiguously separate the interfacial from the bulk contributions to spin relaxation: current-perpendicular-to-plane giant magnetoresistance (CPP-GMR) in ferromagnet/normal metal/ferromagnet (F/N/F) spin valves, with the studied material inserted in the nonmagnetic spacer N [76].

GMR is defined as the difference in resistance of a magnetic multilayer when the magnetic layers are magnetized parallel to each other as compared to when they are anti-parallel. In standard magnetic materials,

the resistance is largest when the magnetic layers are aligned anti-parallel to each other. This effect ultimately originates in the quantum mechanical exchange interaction. It is strictly a magnetic effect, not a spin-orbit effect like some other magnetoresistance effects. In ferromagnetic materials, the exchange interaction splits the conduction bands for majority and minority electrons. The majority and minority bands have different electronic densities of states, which result in different scattering rates, as described by Fermi's Golden Rule [77]. This difference in scattering rates for electrons of different spins in the bulk of a material is quantified by the spin asymmetry: β, and a similar effect at the interfaces between two materials is quantified by the interfacial spin asymmetry γ [32]. The consequence of this spin-dependent electron scattering rate is GMR.

To understand the GMR effect at a slightly deeper level, let's consider a simple model, known as the two-current series resistor (2CSR) model, which is valid in the limit of weak interfacial scattering and long spin diffusion lengths [8]. Current is carried by conduction electrons in both the majority and minority bands. Each magnetic layer is modeled as a separate resistor and the two conduction channels are modeled as parallel lines in the circuit [Fig. 2.1]. The majority channel has a resistance $R_\uparrow$, assumed to be smaller than the resistance of the minority channel $R_\downarrow$. When the two magnetic layers are parallel, the total resistance of the circuit is $R = 1/(1/(2R_\uparrow) + 1/(2R_\downarrow))$. This is relatively low, because most of the current can pass through the low resistance majority channel. However, when the two magnetic layers are anti-parallel, then majority conduction electrons in one layer pass into the second layer, becoming the minority electrons of the magnetically reversed second layer. In this case, both conduction channels are high resistance, leading to a larger total resistance $R = R_\uparrow + R_\downarrow$.

Spin flipping events in the non-magnetic spacer can be modeled as a resistor that shorts the two parallel lines, generally decreasing the magnetoresistance[Fig. 2.1e.]. It is this effect that we use to measure the spin diffusion length in Pt. The value of λ is directly determined from the dependence of GMR on the thickness of the nonmagnetic spacer layer, while the contribution of the interfaces is determined from the dependence on the number of inserted spacers. In CPP-GMR, electrical current flows normal to the studied layer, and therefore electron transport is described by the bulk material parameters even for ultrathin films. In contrast, techniques based on the in-plane current flow require an elaborate analysis of thickness-dependent resistivities and current shunting [67, 68]. Although the GMR-based approach to the quantitative characterization of spin scattering in materials is well established, only one such measurement has been reported for Pt at temperature $T = 4.2$ K [67], yielding the value of λ significantly larger than other approaches [60].

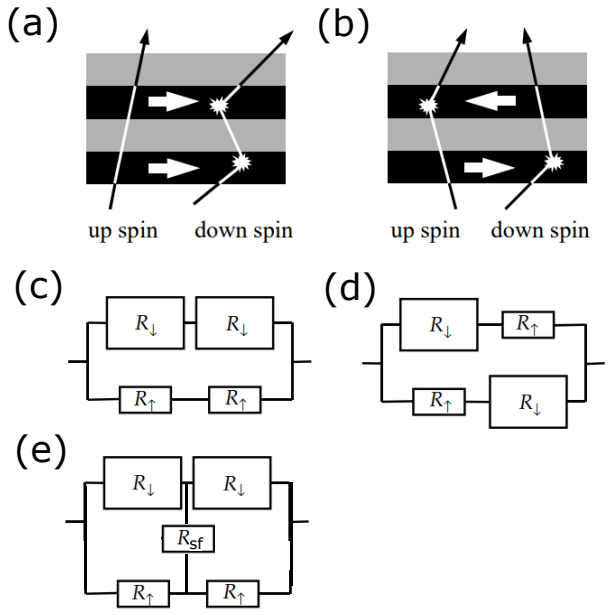

Figure 2.1: Schematics of electron transport in GMR and the two current series resistor model (2CSR), recreated from [8]. (a) Schematic depicting scattering in a magnetic bilayer in parallel alignment. (b) Schematic depicting scattering in a magnetic bilayer in anti-parallel alignment. (c) Equivalent 2CSR circuit corresponding to parallel alignment. The resistors on the left represent the first magnetic layer, while the resistors on the right represent the second magnetic layer. $R_{\uparrow}$ represents scattering of majority electrons (small resistance), and $R_{\downarrow}$ represents scattering from minority electrons (large resistance). (d) Equivalent 2CSR circuit corresponding to anti-parallel alignment. (e) Equivalent 2CSR circuit for parallel alignement, where resistor R_{sf} accounts for spin relaxation, partially shorting the two channels.

2.4 Nanofabrication details

The samples that were studied by GMR were based on multilayers with structure Cu(40)Py(10)Cu(6-d/2)Pt(d)Cu(6-d/2)Py(5)Au(5), where Py=Permalloy=$Ni_{80}Fe_{20}$, and thicknesses are given in nanometers. Py was used as the magnetic material due to its small coercivity (field required to saturate the magnetization), as well as its low magnetic anisotropy. They were deposited on oxidized Si substrates by high-vacuum sputtering in 1.2 mTorr of ultrahigh-purity Argon gas, in a vacuum chamber with a base pressure of 1×10^{-8} Torr. The Pt thicknesses d was varied from 0 to 8 nm in 1 nm increments, and the thickness of the Cu spacers that separate Pt from the ferromagnetic Py layer was adjusted for different values of d so that the total thickness of the spin valves was independent of d, and the Cu was at least 2 nm to avoid the possible effects of proximity-induced magnetism in Pt, resulting in a Cu layer thickness of $6 - d/2$. To analyze such effects, we separately fabricated nanopillars based on the structure Cu(40)Py(10)Pt(1)Cu(4)Py(5)Au(5), whose properties are discussed later in this text.

After the multilayer deposition, a circular Al(50) mask with diameter of 75 ± 5 nm was fabricated on top of the multilayer by a combination of e-beam lithography (EBL) and thermal evaporation. The size of the disk was verified by scanning electron microscopy (SEM). We originally thought that our e-beam lithography set up had a much smaller resolution. A large part of my work in the lab was characterizing and decreasing the resolution of our EBL. During this project the smallest feature size we could make was around 75nm. However, with a combination of using thin EBL resists with small molecular weight, increasing the voltage of our SEM, and developing the resist in an ice bath, I was later able to reduce the smallest feature size down to around 40nm. The voltage of our SEM is limited to 30kV. Many commercial machines allow for voltages up to 100kV, more suitable for small feature design. The ice bath development allows for more careful control over the thermally activated development. It takes more time to develop the resist in an ice bath, which allows the user to more precisely reach the point at which the resist just begins to develop, before the feature begins to over-develop, increasing in size.

The multilayer was removed by Ar ion milling down to the middle of Py(10), everywhere except for the area protected by the Al mask. The ion milling rate was separately calibrated to the precision of better than 10%. An insulating SiO_2(15) layer was deposited immediately after ion milling without breaking the vacuum, to eliminate the possibility of sample oxidation. The remnants of the the Al mask and the SiO_2 covering it were removed by a combination of Ar ion milling at a shallow angle ($\approx 2^\circ$) with respect to the film surface and chemical etching in KOH. NaOH, I learned the hard way, is not a good substitute for KOH, as it sometimes made the insulating layer partially conductive. This is an effect that we don't fully understand, but was detrimental to our sample fabrication process. In the final step of processing, a Cu(80) electrode

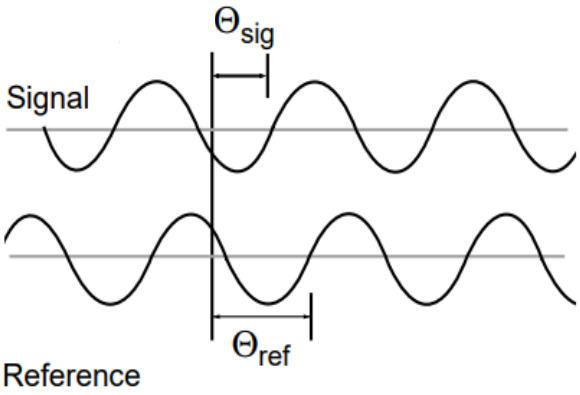

Figure 2.2: Schematic recreated from [9] showing the two primary signals involved in lock-in detection: the reference signal which operates at the frequency of the driving current, the voltage response at that same frequency. Lock-in detection also allows the measurement of the difference of the phase of the signal Θ_{signal} and the driving current Θ_{ref}

was deposited on top.

2.5 Electronic measurement details

Magnetoelectronic measurements were performed in a closed-cycle cryostat, using a pseudo-four probe geometry and the lock-in detection technique, with an ac current of 100 μA rms at a frequency of 1.3 kHz. Lock-in detection is an electronic technique which allows for the extraction of a small signal from a noisy environment. A source of current and the lock-in amplifier, which measures voltage, are phase locked together. A small ac current is applied to the sample and the lock-in amplifier measures the voltage drop across the sample. The lock-in amplifier multiplies the measured harmonic signal by a reference signal at the frequency of the applied current, and is then averaged over time. This allows the lock-in amplifier to extract the voltage at the frequency of the driving current, and minimize spurious contributions at other frequencies. This is due to the orthogonality identity of harmonic functions: $\int_{-\pi}^{\pi} \sin(mx)\sin(nx)dx = \pi\delta_{mn}$, where δ_{mn} is the Kronecker delta: equal to 1 when m=n and 0 otherwise. The measured DC voltage is proportional to the magnitude of the fourier harmonic of the voltage at the reference frequency, and the cosine of the difference between the reference phase and the phase of the voltage response: $V_{DC} \propto V_\omega cos(\Theta_{signal} - \Theta_{ref})$ [9][Fig. 2.2]. For this experiment, we recorded the magnitude of V_ω and divided it by the driving current to measure the resistance of the sample.

The magnitude of the experimentally applied ac current was far below the threshold for the onset of current-induced magnetic dynamics in the magnetic layers. This threshold was at least 1 mA in the

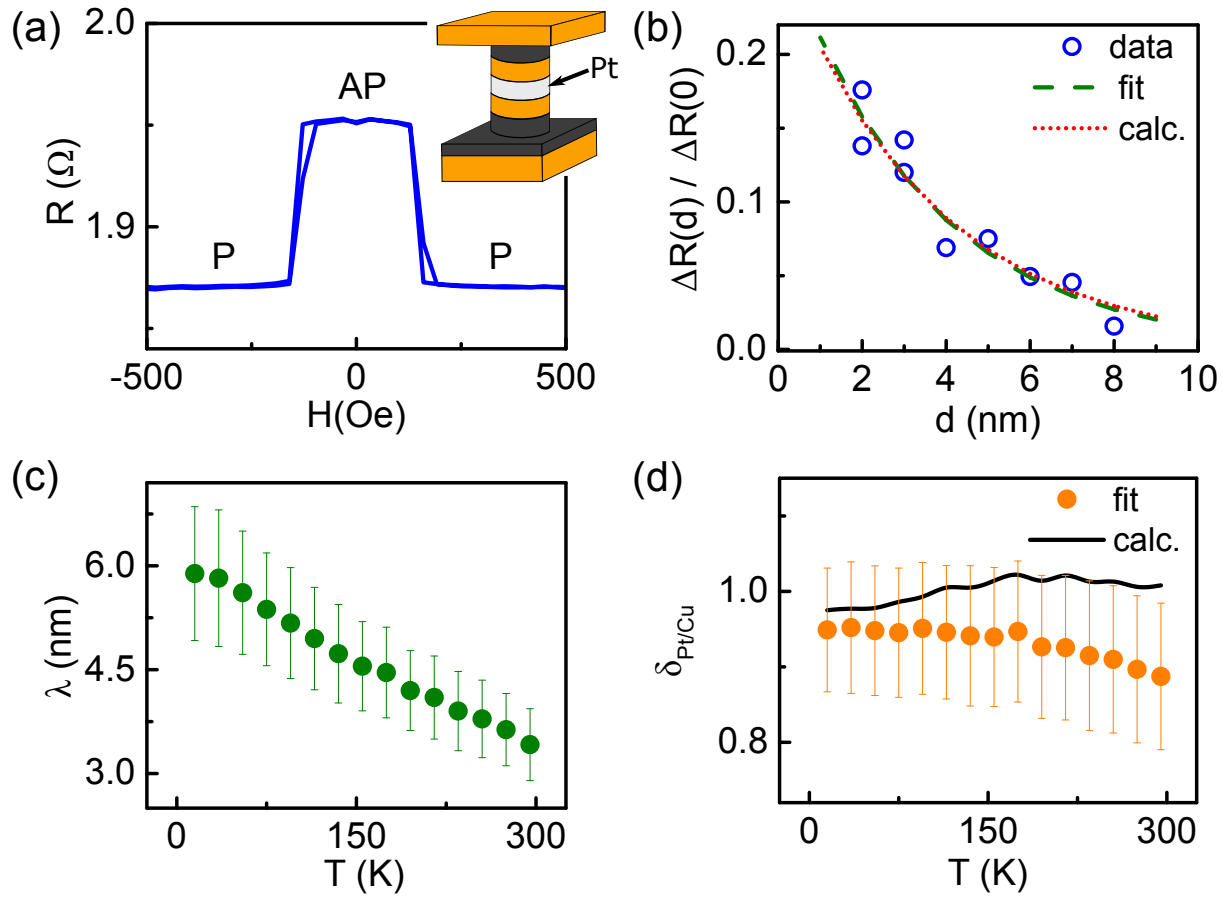

Figure 2.3: (a) Resistance vs applied field for a sample without Pt spacer, at room temperature (RT), $T = 295$ K. Inset: schematic of the studied nanopillars, with Py layers shown in black, Cu in orange, and Pt in white. (b) Symbols: ΔR, scaled by the MR of the reference sample without Pt spacer, vs Pt thickness d, at RT. Dashed curve: exponential fit to the data. Dotted curve: calculation based on the Valet-Fert theory. **(c)** Spin diffusion length vs temperature, determined by fitting $\Delta R(d)$ with Eq. (2.1). (d) Interfacial spin-loss factor vs temperature, obtained by fitting $\Delta R(d)$ with Eq. (2.1) (symbols), and by minimizing the difference between the MR data and the Valet-Fert calculations (curve).

Py/Cu/Py nanopillars without the Pt spacer, and larger in the samples with the Pt spacer. The magnetic field was applied in the sample plane. Its specific in-plane direction did not affect the results.

2.6 Experimental and calculated results and analysis of spin diffusion

The magnetizations of the Py layers formed antiparallel (AP) configuration with resistance R_{AP} at small field, H, due to their antiferromagnetic dipolar coupling [78]. At large fields, both magnetizations became aligned into a parallel (P) configuration with resistance R_P, resulting in switching between P and AP

states in field scans [Fig. 2.3(a)]. At a given temperature, T, the dependence of magnetoresistance (MR), $\Delta R = R_{AP} - R_P$, on d was well-approximated by the exponential

$$\Delta R(d) = \Delta R(0) e^{-d/\lambda - 2\delta_{Pt/Cu}}, \tag{2.1}$$

as shown by the dashed curve in Fig. 2.3(b) for room temperature (RT), $T = 295$ K. Here, $\delta_{Pt/Cu}$ is the parameter describing spin loss at the Pt/Cu interface [57, 65, 79]. The temperature dependencies of λ and $\delta_{Pt/Cu}$, determined by fitting the dependence of MR on d with Eq. (2.1) at each T, are shown by symbols in Figs. 2.3(c) and (d), respectively. The value of λ increased from 3.5 nm at RT to 6.0 nm at 7 K [Fig. 2.3(c)]. The slight increase of $\delta_{Pt/Cu}$from 0.89 at RT to 0.95 at 7 K was within the fitting uncertainty.

Although the value of $\delta_{Pt/Cu}$ is not central to our study, we briefly discuss it here. This parameter is generally well-defined only for diffuse interfaces, $\delta = w/\lambda_I$, where w is the width of the interfacial region, and λ_I is the effective spin diffusion length [57]. To establish whether this interpretation is consistent with the fitting using Eq. (2.1), we performed calculations based on the Valet-Fert (VF) theory of GMR [80–82], using the extracted λ and the known spin-dependent transport properties of Py, Cu and their interfaces [60, 83].

In the VF model, the different layers are described by the bulk resistivity ρ, the scattering asymmetry $\beta = (\rho^{\downarrow} - \rho^{\uparrow})/(\rho^{\downarrow} + \rho^{\uparrow})$, and the spin diffusion length λ. The interfaces between materials are described as thin layers of thickness $d_{int} = 0.5$nm, which is a typical atomic interdiffusion thickness for transition metals. We confirmed that variations of interfacial layer thickness, over a reasonable range, did not noticeably affect the results of the calculations. The interfacial spin transport parameters were converted into effective bulk properties as follows: $\rho_{int} = AR/d_{int}$, where AR is the interface specific resistance, $\beta_{int} = \gamma = (AR^{\downarrow} - AR^{\uparrow})/(AR^{\downarrow} + AR^{\uparrow})$, where γ is the interfacial spin asymmetry, and $\lambda_{int} = d_{int}/\delta$, where δ is the interfacial spin scattering parameter.

The two governing equations: $\partial^2(\mu_{\uparrow} - \mu_{\downarrow})/\partial x^2 = (\mu_{\uparrow} - \mu_{\downarrow})/\lambda^2$ and $\partial \mu_{\uparrow,\downarrow}/\partial x = e\rho_{\uparrow,\downarrow}$ were solved for each layer, with the boundary conditions of continuity for the spin-up and spin-down effective electrochemical potentials, the charge current, and the spin current at each interface. These equations are solved for the spin-dependent effective electrochemical potentials throughout the multilayer, yielding the position-dependent spin accumulation, defined as the difference between spin-up and spin-down effective electrochemical potentials in the form $\Delta\mu(x) = Ae^{x/\lambda} + Be^{-x/\lambda}$ for each layer. The resulting analytical form of MR as a function of Pt layer thickness d generally has a relatively complicated form. However, as shown in Fig. 2.3b., it is well approximated for the studied samples with Pt spacers by $\Delta\mu(x) \approx e^{-d/\lambda}$. This can be attributed to the short spin diffusion length λ in Pt and large spin loss at its interfaces that almost completely eliminate the interplay between spin-dependent scattering at the magnetic interfaces separated by the nonmagnetic

Material Parameters used in VF calculations	
T=5 K	T=295 K
Bulk resistivity ρ (nΩ m)	
$\rho_{Cu} = 10.6$ [84] $\rho_{Py} = 112$ [84] $\rho_{Pt} = 112$ [84]	$\rho_{Cu} = 34.8$ [84] $\rho_{Py} = 238$ [84] $\rho_{Pt} = 248$ [84]
Specific resistivity AR (f Ω m^2)	
$AR_{PyCu} = 0.255$ [85] $AR_{PtCu} = 0.75$ [86]	$AR_{PyCu} = 0.255$ [85] $AR_{PtCu} = 0.75$ [86]
Spin asymmetry β	
$\beta_{Cu} = 0$ $\beta_{Py} = 0.7$ [85, 87, 88] $\beta_{Pt} = 0$	$\beta_{Cu} = 0$ $\beta_{Py} = 0.29$ [85, 87, 88] $\beta_{Pt} = 0$
Interfacial spin asymmetry γ	
γ_{PyCu}=0.7 [85] γ_{PtCu}=0	γ_{PyCu}=0.7 [85] γ_{PtCu}=0
Spin diffusion length λ (nm)	
$\lambda_{Cu} = 500$ [60] $\lambda_{Py} = 5.4$ [85] $\lambda_{Pt} = 5.8$ [84]	$\lambda_{Cu} = 500$ [60] $\lambda_{Py} = 2.58$ [85] $\lambda_{Pt} = 3.42$ [84]
Interfacial spin flip parameter δ	
$\delta_{Py/Cu} = 0.3$ [60] $\delta_{Pt/Cu} = 0.98$ [84]	$\delta_{Py/Cu} = 0.3$ [60] $\delta_{Pt/Cu} = 1$ [84]

spacer.

The nanopillar diameter of 75 nm, determined by SEM imaging, was used in these calculations. Table 1 shows the spin transport parameters used in our calculations at 5 K and 295 K. Their temperature dependence was determined from the following analysis. The temperature-dependent value of spin diffusion length λ_{Py} in Py has been reported at 4.2K [85]. We assumed that EY scattering is dominant in Py ($\lambda \propto l$), and used the temperature-dependent mean free path in Py, extracted from our resistivity measurements for Py, to determine λ_{Py} as a function of temperature. We used the bulk spin asymmetry parameter β_{Py} for Py as a fitting parameter for the calculations of the Py(5)Cu(10)Py(5) nanopillars to minimize the difference between the calculation and our measured results. The resulting value of β_{Py} agrees with the well-established low temperature value [85, 87, 88] and the T^{-2} dependence expected for higher temperatures [88]. In Fig. 2.4(a), we show both the measured and the calculated MR for nanopillars without Pt.

In VF calculations for the Py/Cu/Pt/Cu/Py nanopillars, we used λ_{Pt} extracted from our experiments, and $\delta_{Pt/Cu}$ as a fitting parameter to minimize the difference between our data and the calculations. The best fit was achieved with $\delta_{Pt/Cu} \approx 0.98$ with a modest temperature dependence, as shown in Fig. 2.3(d). It is consistent with the previously reported value of $\delta_{Pt/Cu} = 0.9$ [67]. In Fig. 2.4(b-h), we show the measured and the calculated MR for the nanopillars with different thicknesses of Pt. The minor variations between the calculations and the experiments are likely the result of small variations of the material

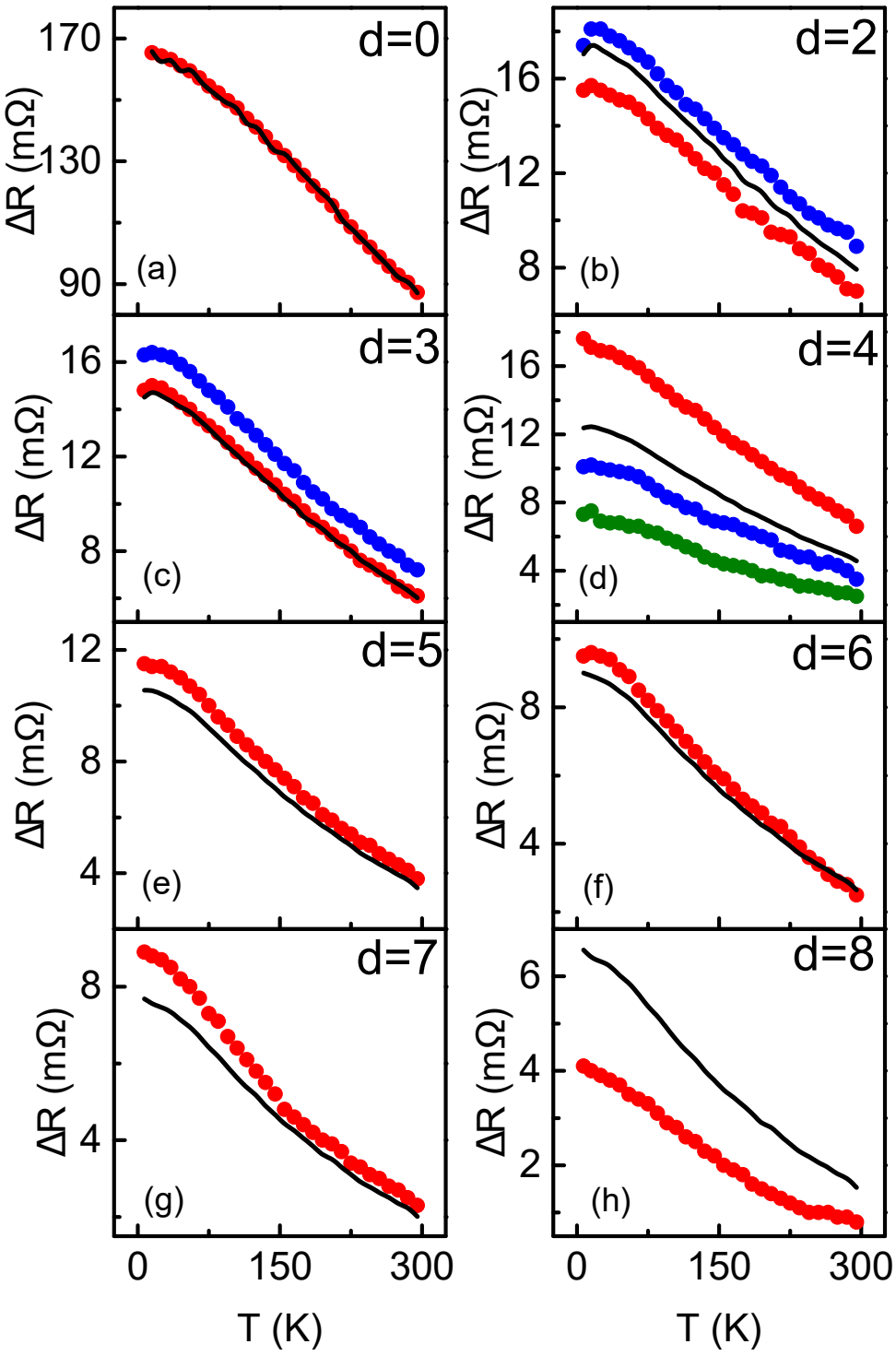

Figure 2.4: Symbols: measured MR vs temperature for each of the samples used in our analysis of spin scattering in Pt, with labeled Pt spacer thickness d in nm. Different colors correspond to different samples. Curves: calculated MR vs temperature obtained using the VF model. There are three samples shown in panel d, because of repeatability issues with sample fabrication; however, the average of the three samples agrees well with theory.

deposition/nanofabrication conditions, and are not essential to the analysis shown later in this text.

Based on these data and calculations, we conclude that the spin relaxation rate at the Cu/Pt interface is approximately temperature-independent. The overall agreement between the VF calculations and the fitting based on Eq. (2.1) validates our interpretation of λ and $\delta_{Pt/Cu}$ in terms of clear separation of the bulk and interfacial contributions to spin diffusion across Pt layers. We emphasize that neither VF calculations, nor magnetoelectronic circuit theory, are needed to extract these parameters, reflecting the robust model-independent nature of the CPP-GMR experimental technique.

2.7 Characterization of the electronic properties of the studied Pt films

To relate the measured spin diffusion parameters to the spin scattering rates, and analyze the mechanisms of spin relaxation, we first determined some basic electronic transport properties: extracted from the momentum scattering rates and the carrier concentration from resistivity and Hall effect measurements, respectively. Both measurements were performed in the van der Pauw geometry on 6.3×6.3 mm^2 oxidized Si chips, with Pt films sputtered directly on top. In the studied nanopillars, current flowed normal to the thin Pt layers, and our analysis explicitly incorporated scattering at their interfaces. Therefore, bulk electronic characteristics of Pt are relevant for the analysis of the charge and spin transport through the studied Pt layers. To determine the bulk Pt resistivity, we measured the resistivity of 3 nm, 10 nm, and 20 nm-thick Pt films at temperatures between 7 K and 295 K. At each temperature, we obtained a linear relation between the inverse of the Pt thickness d and resistivity [Fig. 2.5a.], as expected due to the effects of surface scattering [89]. Bulk resistivity was determined by extrapolating this dependence to $1/d = 0$. We note that the extracted values were very close to the resistivity obtained for $d = 20$ nm, consistent with negligible contribution of surface scattering for the material with mean free path $l \ll 20$ nm.

The carrier concentration n_e was determined from the Hall-effect measurement in a Pt(20) film, using $n_e = B/(R_H e d)$, where B is the magnetic field, R_H is the Hall resistance, e is the electron charge, and d is the film thickness [90]. The Hall measurement shown in Fig. 2.5b. yields $n_e = 2.81 \cdot 10^{29} m^{-3}$. Several years after the completion of this project, I was instructed by a fellow labmate, that this estimate for the carrier concentration is only a rough approximation, and that the fact that conduction in Pt is facilitated by both 5d and 4f electrons makes analysis of the carrier concentration more complex than the simple, textbook analysis that I show here.

The temperature-dependent mean free path, shown in [Fig. 2.5c.]was calculated from the obtained values

of the carrier concentration and the bulk resistivity, using the Drude formula: $l = m_e v_F/(n_e e^2 \rho)$, where m_e is the mass of the electron, e is the electron charge, $v_F = 4.2a_0(3/(4\pi n_e))^{-1/3} \cdot 10^{-8}$cm/s is the Fermi velocity, a_0 is the Bohr radius.

2.8 Analysis of mechanisms of spin relaxation in Pt

Two well-known, separate spin-orbit mechanisms can contribute to spin relaxation in materials and at their interfaces. Elliott-Yafet (EY) relaxation is caused by scattering on phonons and impurities in the presence of spin-orbit band mixing, resulting in a linear relationship between the average time between spin-flipping events, τ_{sf}, and the average time between momentum scattering events, τ_p [69]. This is simply a consequence of SOC, which causes spin-polarized electronic states to no longer be eigenstates. Instead, spin-mixed states are eigenstates: $\Psi = a \cdot \Psi_\uparrow + b \cdot \Psi_\downarrow$, where a and b are coefficients related to the strength of SOC. Perturbations like momentum scattering events have a finite chance to flip the spin of a conduction electron: $P_{sf} = b^2/(1 - b^2)$. A schematic of this mechanism is shown in Fig 2.7a. The EY mechanism is expected to be the dominant mechanism of spin relaxation in most SHE materials such as Pt.

Dyakonov-Perél (DP) relaxation is associated with spin precession around an effective spin-orbit field, $\vec{H}_{SO}$, found at interfaces (the Rashba field, described earlier in this chapter) and in bulk materials with broken inversion symmetry (the Dresselhaus effect) [10, 69, 71, 72, 91, 92]. Spin dephasing caused by the dependence of $\vec{H}_{SO}$ on the electron's momentum results in the inverse relation between τ_{sf} and τ_p [91] for DP relaxation. A schematic of this mechanism is shown in Fig 2.7b.

Using the mean free path, described in the previous section, we are able to extract the momentum relaxation time using $\tau_p = l/v_F$, shown as a function of temperature in Figure 2.8a. Figure 2.8b shows the temperature dependence of the spin-flip time τ_{sf}, determined from λ [Fig. 2.3c] using $\lambda = \sqrt{v_F l \tau_{sf}/3}$ [60]. Significantly larger values of τ_{sf} were obtained for Pt from Hanle-type measurements [93], likely because such measurements are dominated by the low-mobility (5d band) carriers whose spin relaxation can be significantly slower than that of high-mobility (4f band) carriers in transport phenomena [94].

At high temperatures, both τ_p and τ_{sf} in Figs. 2.8(a)(b) linearly increase with decreasing temperature, T, consistent with the dominance of the EY mechanism. While the dependence $\tau_p(T)$ remains monotonic at low T, τ_{sf} starts to decrease. This decrease of τ_{sf} with increasing τ_p [Fig. 2.8(c)] is reminiscent of the DP mechanism, which is not allowed in Pt by symmetry. We emphasize that the CPP-GMR approach allows us to unambiguously attribute this to the bulk spin relaxation; if it were caused by the interfacial effects, this would have been captured by an increase of $\delta_{Pt/Cu}(T)$ [Fig. 2.3(d)].

The DP relaxation at Pt interfaces is allowed by symmetry [72]. However, DP relaxation in bulk Pt is

prohibited by symmetry, so the spin relaxation in Pt has been attributed to the EY mechanism [52, 63, 68]. Increased spin relaxation observed at low temperatures in measurements of spin transport along Ag and Cu nanowires [95–97] has been explained by the increased contribution of surface scattering, when the mean free path becomes large. In CPP-GMR, current flows normal to the film, so this effect is not relevant. We can also eliminate the effects of magnetic fluctuations in Pt, which are too small to explain the observed enhancement of spin relaxation, as described in detail in a later section.

To interpret our results, we note the intrinsic SHE in Pt, a topological effect that is expected to be the dominant mechanism of the SHE in bulk Pt [12, 52]. The intrinsic SHE is due to the large spin Berry curvature of electron bands in materials with strong SOC, in the vicinity of nearly-degenerate points, known as spin hot spots [11, 12, 98]. When two electronic bands approach each other at some point in the Brillouin Zone, SOC mixes the bands, causing a phenomena known as anti-crossing or avoided crossing [Fig 2.7]. These points of anti-crossing are known in some contexts as spin hot-spots. A well known consequence of this avoided crossing is the Berry's Phase or Berry Curvature, a topological effect that is seen in various types of physical phenomena, including the common museum physics demonstration "Foucault's Pendulum" [11, 99]. It results from the movement of an electronic state (or more generally any vector) adiabatically [100] through a closed loop in some parameter space [11]. In condensed matter systems, the presence of Berry Curvature requires broken time inversion symmetry, broken spatial inversion symmetry, or spin-orbit coupling. In the case of the intrinsic SHE, the Berry curvature comes from the mixing of the bands at the spin hot-spots. Qualitatively, the "closed loop" can be thought of as the electron hopping between the two nearly degenerate electronic bands. The primary consequence of the Berry curvature is a transverse velocity that propagating electrons develop: a topological Hall effect, known in ferromagnetic materials as the intrinsic anomalous Hall effect, and in nonmagnetic materials is known as the instrinsic spin Hall effect or the orbital Hall effect [11, 98].

Colloquially, my original line of thought was that if the spin hot-spots result in the generation of spin polarization in some contexts (SHE), then they can likely also destroy spin polarization in other contexts. In fact, it is known that the polarization of electrons are exactly zero at the point of avoided crossing, the spin hot-spot [11]. Therefore, if initially spin-polarized electrons are injected from another material into a state near a spin-hot spot in a material with strong SOC, like Pt, then the electron will experience spin dynamics, even in the absence of scattering. Since these dynamics depend on the wavevector, they must result in spin dephasing similar to the DP relaxation. We describe this effect as "Dyakonov-Perél-like spin relaxation".

Another potential explanation for the experimentally observed effects comes from the Berry curvature in Pt, which creates a transverse trajectory of the itinerant conduction electrons , an effect which is known to become stronger at low temperatures [52]. As the conduction electrons pass "perpendicular-to-plane"

through the Pt layer, the Berry Curvature directs them towards the edges of the nanopillar. Scattering from the edges of the nanopillar would lead to EY spin relaxation. Also the broken inversion symmetry at the edges of the nanopillar result in a Rashba field near the edges, which could cause classic DP spin relaxation. Both of these types of edge relaxation would scale with the thickness of the Pt space layer, and therefore the effects would contribute to the measurement of the spin diffusion length λ, and consequently the spin lifetime τ_{SF} that we are analyzing here. The influence of edge scattering could be investigated by a simple, systematic study of temperature dependent MR from nanopillars with various diameters.

To quantify different contributions to spin relaxation in Pt, we use Matthiessen's rule $1/\tau_p = 1/\tau_{imp} + 1/\tau_{ph}(T)$ to separate the momentum relaxation rates $1/\tau_{imp}$, and $1/\tau_{ph}$ due to scattering on impurities and phonons, respectively. We fit the relationship between τ_{sf} and τ_p with $1/\tau_{sf} = 1/\tau_{DP} + 1/\tau_{EY}$, where $1/\tau_{DP} = (\Omega_{SO}^2\tau_p)$ and $1/\tau_{EY} = b_{imp}^2/\tau_{imp} + b_{ph}^2/\tau_{phonon}$ are the DP-like and the EY contributions to spin relaxation [69]. Here, b_{imp} and b_{ph} are the effective spin mixing parameters associated with impurity and phonon scattering, respectively. For simplicity, we characterize the DP-like relaxation by an average effective spin-orbit field H_{SO}, with $\Omega_{SO} = g\mu_B H_{SO}/\hbar$ representing the average precession frequency around H_{SO}. It is important to note that a true magnetic field is not allowed due to symmetry. H_{SO} is simply used to model the DP-like relaxation effect described above. The fitting [curve in Fig. 2.8(c)] allows us to estimate $H_{SO} \approx 1280 \pm 80$ T, $b_{imp} \approx 0.062 \pm 0.057$, and $b_{phonon} \approx 0.208 \pm 0.008$, where the uncertainties reflect the accuracy of the fitting.

The average precession phase, $\Omega \cdot \tau_p \approx 0.2$, between momentum scattering events satisfies the random spin-walk approximation used in our analysis. The probability of spin flipping per momentum scattering event, $P_{sf} = b^2/(1-b^2)$ [10], gives one spin flip per 25 (160) phonon (impurity) scattering events, consistent with the diffusive limit used in our analysis. At RT, the EY contribution to spin relaxation is about 2 times larger than the DP-like contribution [Fig. 2.8(d)]. The EY contribution decreases linearly with decreasing T, while the DP-like contribution increases, becoming larger than that of EY at temperatures below 195 K. With increasing purity of Pt, the DP-like contribution is expected to increase, while the EY contribution should decrease.

2.9 Interplay between Spin-Orbit Effects and Magnetism

Further evidence for DP-like relaxation in Pt was provided by measurements of the nanopillar with an active spin valve structure Py(10)Pt(1)Cu(4)Py(5), where Pt was interfaced with Py. In this case, the MR linearly increases with decreasing temperature [triangles in Fig. 2.9(a)]. In contrast, for the standard structure with $d = 1$, the MR starts to decrease at low T [circles in Fig. 2.9(a)]. The downcurving of MR is also apparent

in the VF calculations [solid curve in Fig. 2.9(a)], but is less significant, likely due to the limitations of the diffusive transport model and/or the discontinuity of the Pt(1) layer. Measurements and calculations for thicker Pt also showed downcurving of MR at low T, which can be attributed to the DP-like relaxation [15]. For Pt directly interfaced with Py, the linear dependence of MR on T without such downcurving indicates that DP-like relaxation is suppressed, which was confirmed by the VF calculation including only the EY mechanism [dotted curve in Fig. 2.9(a)].

The difference between the two structures can be correlated with the temperature-dependent magnetic properties of Pt, as illustrated in Fig. 2.9(b), reproduced from Ref. [13]. Symbols show the measured magnetic correlation length, and the curve shows the temperature dependence expected from the Curie-Weiss law, extrapolating to the Curie temperature of 90 K. The correlation length significantly deviates from the Curie-Weiss law at $T < 110$ K, and starts to decrease at $T < 25$ K, suggesting that magnetism in Pt becomes suppressed. Indeed, ferromagnetism was reported only in ultrathin Pt films and nanoparticles [101–103].

Both the effects of the magnetic interfaces on MR and the suppression of magnetism in Pt are observed at cryogenic temperatures, where the DP-like relaxation becomes increasingly significant [see Fig. 2.8(d)]. We model these effects by the interplay between H_{SO} and the proximity-induced effective exchange field H_{ex}. As stated in the previous section, H_{SO} is not a true magnetic field, but rather a way to quantitatively analyze the effect of the spin hot-spot (see Fig. 2.7). In this toy-model, the electron's spin experiences a large-angle precession around the total effective field, $\vec{H}_{eff} = \vec{H}_{SO} + \vec{H}_{ex}$. If $H_{ex} \ll \vec{H}_{SO}$ away from magnetic interfaces, the spins of the diffusing electrons, characterized by a broad distribution of wavevectors, $\vec{k}$, are efficiently dephased by the effects of the spin hot spot, H_{SO} [Fig. 2.11a]. SOI-induced spin dephasing, specifically the effects of the spin hot-spot, are possibly responsible for the suppression of magnetism in Pt, since it competes with the exchange interaction that stabilizes an ordered-spin state of the Fermi sea comprising electrons with a broad distribution of $\vec{k}$.

If $H_{ex} \gg H_{SO}$, near a magnetic interface, the spin precesses around the effective field, $\vec{H}_{eff}$, dominated by $\vec{H}_{ex}$ [Fig. 2.11b]. Since the spins of the electrons injected from the ferromagnet are aligned with $\vec{H}_{ex}$, their precession angle is small, resulting in suppression of the precessional spin relaxation, and thus an enhanced MR in the samples with proximity-magnetized Pt [Fig 2.9a]. This toy model is consistent with the reported suppression of DP relaxation by the external field [94], and with the reduction of intrinsic SHE in proximity-magnetized Pt [70].

2.10 Possible effects of magnetic fluctuations on spin relaxation

The central experimental result of our study, the observation of a decreasing spin lifetime in Pt with increasing momentum relaxation time at low temperatures, is explained by the effects of the spin hot-spots in the electronic band structure, deemed "Dyakonov-Perel (DP)-like spin relaxation". Since Pt is almost ferromagnetic [13], magnetic fluctuations can, at least in principle, also play a role in spin relaxation. The spin of the conduction electron can experience a random local exchange field produced by the magnetic fluctuation, resulting in precession and dephasing similar to those discussed in the context of the classic DP relaxation mechanism. Since magnetism has been demonstrated in nanoconfined Pt structures such as thin films, nanowires, and nanoparticles [101–103], the resulting relaxation may become most significant in thin Pt layers. Moreover, such effects may be enhanced by magnetic impurities.

Here, we describe the analysis and present measurements eliminating these possibilities. In the previous section, I discussed the estimation of the effective field $B_{DP} = 1300$ T that models the effect of the spin hot-spots that we deemed "DP-like spin relaxation". Assuming instead that this effect is caused by the effective exchange field due to magnetization fluctuations, we use Weiss's molecular field approximation to estimate that the corresponding average magnitude of the magnetization should be $M_{Pt} \approx 100$ emu/cm^3. Indeed, the magnetization of typical transition-metal ferromagnets like Co, Ni, and Fe is $M \approx 10^3$ emu/cm^3, resulting in the effective exchange field (the exchange splitting) of about $B_{ex} \approx 10^4$ T. Since 3d ferromagnets are more itinerant than the 5d Pt, the value of M_{Pt} given above is likely an underestimate.

To test for the signatures of magnetism in the studied Pt films, we utilized superconducting quantum interference (SQUID) magnetometry. The dependence of magnetization on field and temperature was measured in two structures incorporating Pt layers, a bilayer Pt(200)Cu(100) to characterize the magnetic properties of bulk Pt, and a multilayer of 100 repetitions of [Pt(2)Cu(1)] to characterize the magnetic properties of thin Pt films and the Pt/Cu interfaces similar to those in our GMR study of nanopillars. Both structures were sputtered under the same conditions, and from the same material sources as the nanopillars, and thus the characteristics of the Pt films, including the concentration of magnetic and nonmagnetic impurities, are the same in both studies. As can be seen from Fig. 2.11, the magnetic moment of both studied samples did not exceed 10^{-5} emu at ± 1 kOe, which can be attributed to a combination of the effects of paramagnetic impurities in Si, Cu and Pt, and a possible additional contribution of magnetism in Pt. Based on these data, we estimate the upper limit for the magnetization of Pt at 1 emu/cm^3, two orders of magnitude smaller than would be necessary to produce the observed DP-like contribution to spin relaxation.

We should also mention that the Kondo effect, which has been invoked in the studies of spin relaxation near the interfaces of thin films [104], is not expected to occur in Pt, because magnetic impurities are known

to produce giant magnetic moments due to the proximity of Pt to the ferromagnetic transition [105].

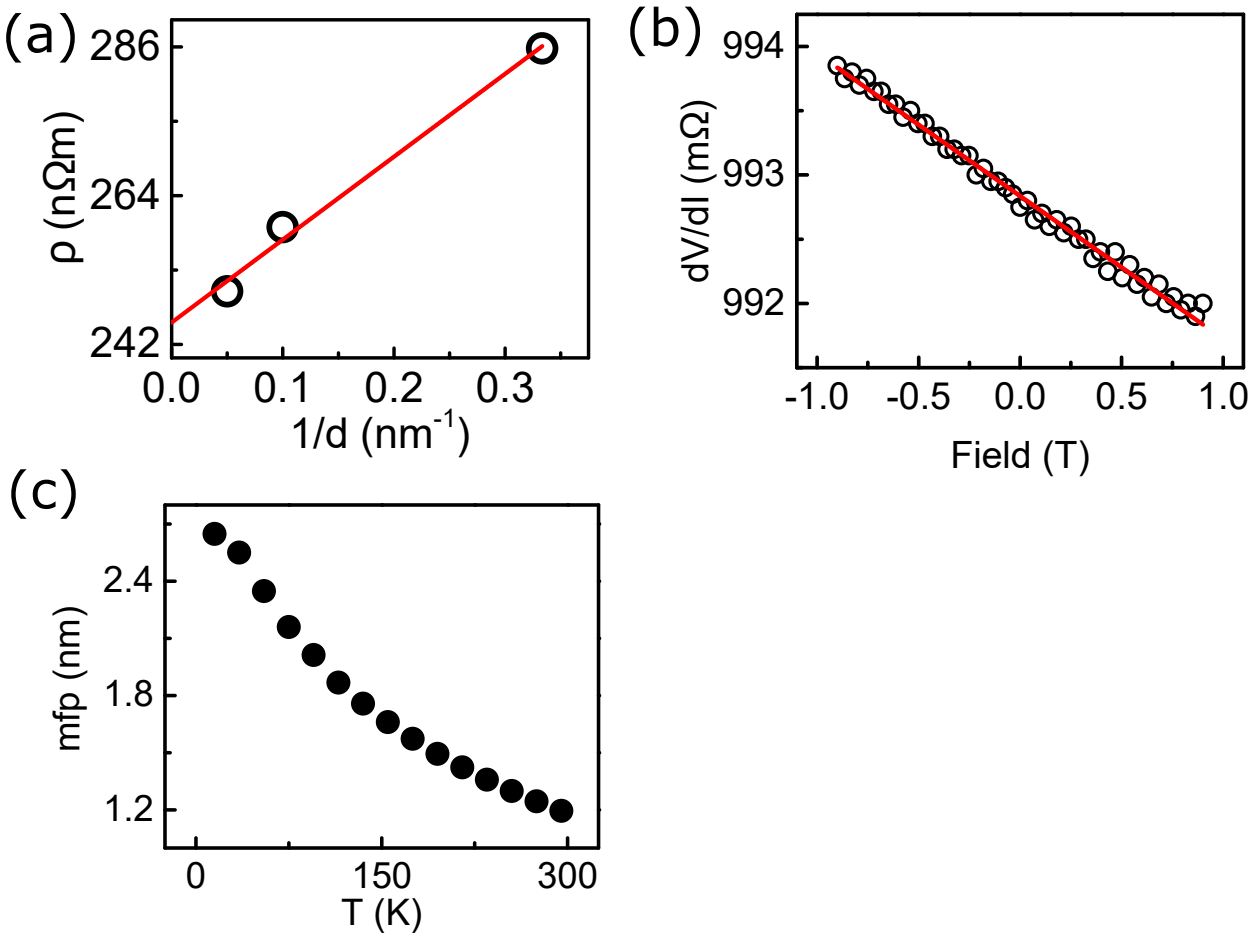

Figure 2.5: a) Symbols: Resistivity of three Pt films with thicknesses $d = 3$, 10, and 20 nm vs $1/d$, at room temperature $T = 295$ K. Line is a linear fit of the data. b) Symbols: Hall resistance vs applied field for a 20 nm-thick Pt film, at room temperature $T = 295$ K. Line is a linear fit of the data. c) Mean free path in the studied Pt vs temperature.

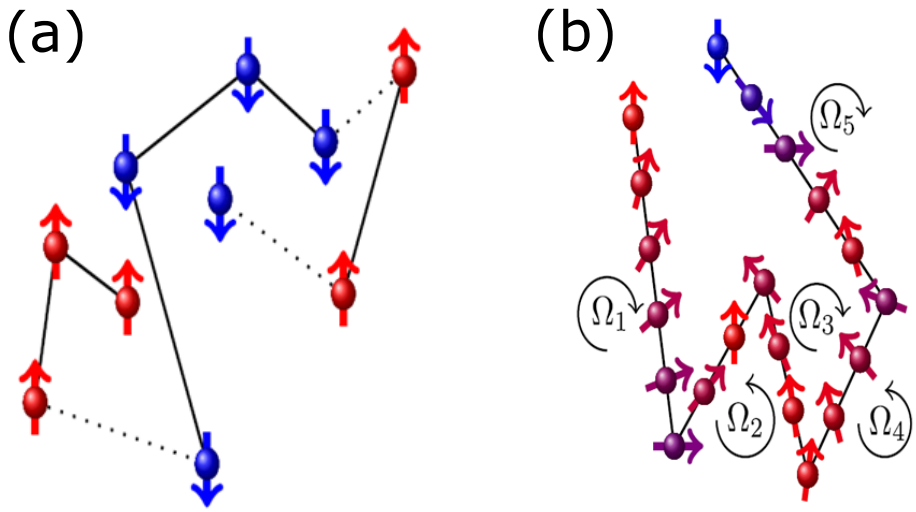

Figure 2.6: Schematic of two common spin relaxation mechanisms, recreated from [10]. (a) Elliott-Yafet (EY) relaxation, where momentum scattering events allow for a finite chance of spin-flipping. (b) Dyakonov-Perél (DP) relaxation, where spins precess around a momentum dependent spin-orbit field and dephase.

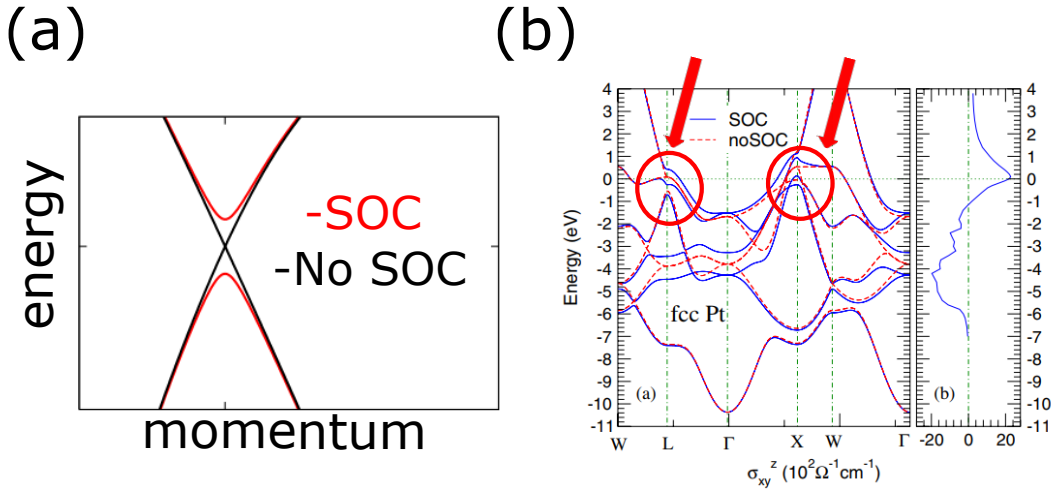

Figure 2.7: (a) Schematic of anti-crossing that occurs when two branches of an excitation become degenerate and are also coupled to each other energetically, recreated from [11]. This specific example shows electronic bands that hybridize and form an energy gap due to the spin-orbit interaction. In this context, the point of anti-crossing is known as a spin hot-spot. (b) Figure recreated from [12]. The left plot shows the band structure of Pt, with zero energy corresponding to the Fermi energy. The red circles indicate locations of anti-crossing, due to SOC. The right plot shows the strength of the Berry Curvature, responsible for the intrinsic SHE in Pt.

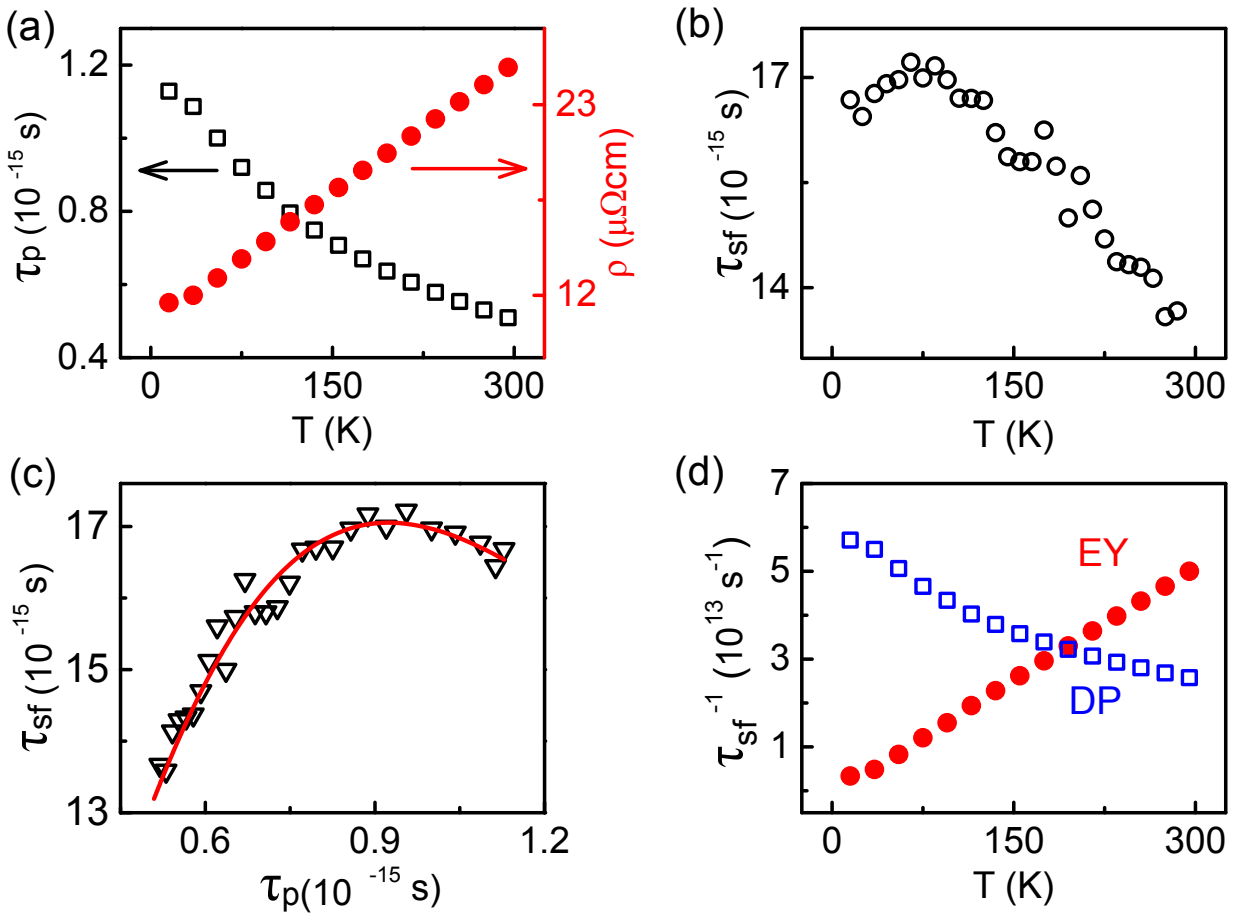

Figure 2.8: (a) Bulk resistivity (right scale) and the momentum relaxation time (left scale) vs temperature for the studied Pt films. (b) Spin relaxation time vs temperature determined from the data of Fig. 2.3(c). (c) Spin relaxation time vs momentum relaxation time. Symbols: data, curve: fitting with a superposition of EY and DP-like contributions, as described in the text. (d) Temperature dependence of the contributions to spin relaxation from DP-like and EY mechanisms, as labeled, determined from the fitting in panel (c).

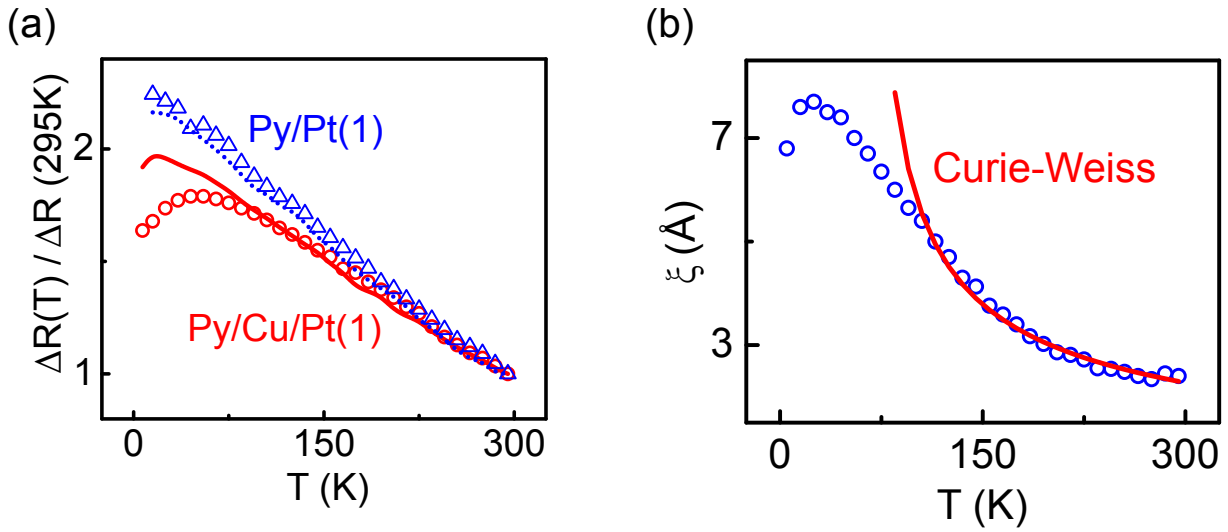

Figure 2.9: (a) Measured (symbols) and calculated (curves) MR vs temperature for the standard spin valve nanopillar with $d = 1$ nm (circles and solid curve), and for the nanopillar with the structure Py(10)Pt(1)Cu(4)Py(5) (triangles and dotted curve). For the latter, the calculation includes only the EY contribution to spin relaxation. The MR is normalized by its value at RT. (b) Symbols: magnetic correlation length in Pt vs temperature, from Ref. [13]. Curve: dependence expected based on the Curie-Weiss law.

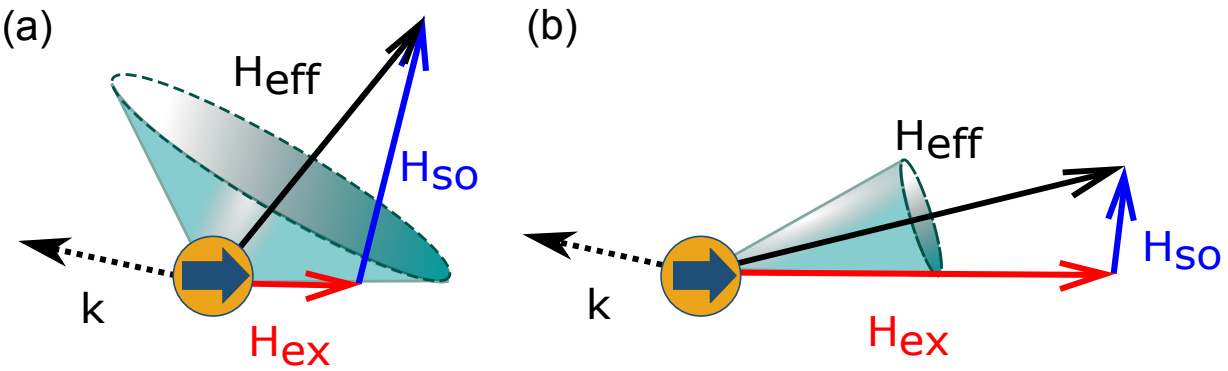

Figure 2.10: Interplay between magnetism and intrinsic spin-orbit interaction. The spin of electron in Pt precesses around the effective field $\vec{H}_{eff} = \vec{H}_{SO} + \vec{H}_{ex}$, where $\vec{H}_{SO}$ is the effective spin-orbit field determined by the electron's momentum $\vec{k}$, and $\vec{H}_{ex}$ is the effective exchange field due to either proximity-induced magnetism or magnetic fluctuation in Pt. The electron's spin is shown by a bold circled arrow. (a) If H_{SO} dominates, precessional dephasing suppresses the spin polarization and/or magnetization fluctuation. (b) If H_{ex} dominates, the precession angle for electron spins aligned with $\vec{H}_{ex}$ is small, suppressing the DP-like spin relaxation.

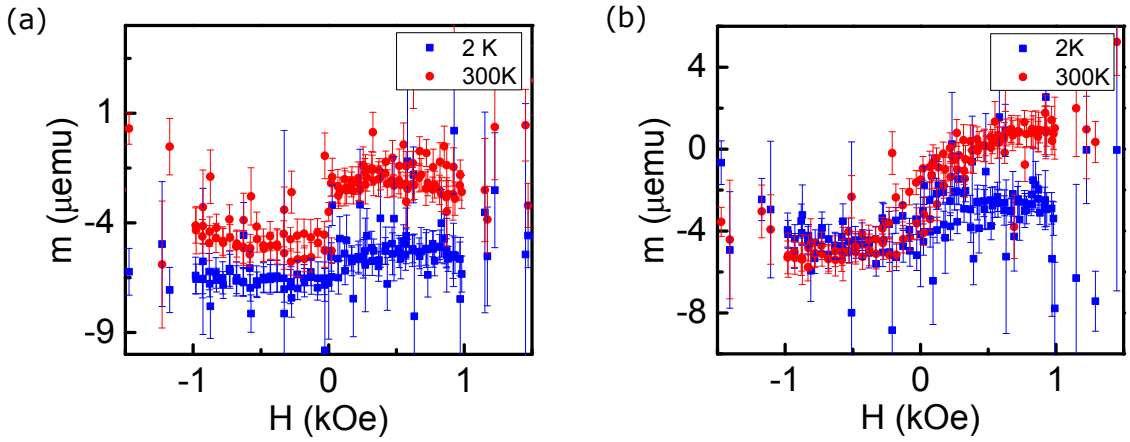

Figure 2.11: Magnetic moment vs applied field for bilayer Pt(200)Cu(100) (a) and for the multilayer $[Pt(2)Cu(1)]_{100}$ (b) deposited on 6.3×6.3 mm^2 oxidized Si substrates. The red circles (blue squares) are for $T = 300$ K ($T = 2$ K).

Chapter 3

Stimulated and Spontaneous Emission of Magnons Driven By Electrical Current

3.1 Background on spin transfer: semi-classical and quantum models

As described in the section 'Interfacial Spin-Orbit Effects' in the thesis chapter 2 on 'Spin Relaxation in Pt', the transfer of angular momentum from electrons in one material into another magnetic material, deemed 'spin transfer' is a very complicated process, with many different physical effects occurring at both interfaces and in the bulk of the materials. Consequently, there have been many models created to describe this process under different approximations and under different theoretical frameworks. For instance, the well-known spin Hall effect, described throughout this thesis, is often invoked as a simple explanation for the effects of the transfer of both spin and orbital angular momentum, coming from bulk and interfacial effects [48, 98]. Furthermore, 'magneto-electronic circuit theory' combines many spin-orbit and magnetic effects at interfaces and in bulk into effective parameters in a large, complicated matrix that determine spin and charge transport through magnetic materials [52, 56, 65, 73–75].

A more focused, but approximate theory on spin transfer from itinerant electrons into a magnetic system was developed by Slonczewski in 1996 [106], by essentially looking at only a single effect, the conservation of angular momentum during scattering between a single electron and a single spin wave mode. In this model,

the spins that are responsible for the magnetization of the magnetic material are approximately described as a spin wave with wavevector k=0, i.e. the uniform precession or ferromagnetic resonance (FMR) mode. In this model, the total angular momentum in the magnetic material is added up into what is called a 'macrospin'. In this theory, the spin of the incoming electron is rotated to be aligned or anti-aligned to the macrospin, due to the influence of the magnetic exchange interaction. The component of the incoming electron's spin transverse to the macrospin is absorbed, exerting a torque on the macrospin, either increasing or decreasing the amplitude of the FMR spin wave mode depending on the orientation of the incoming spin with respect to the macrospin. In the language of magnons, the number of magnons is modified by the electrical current as described in the following equation:

$$< N(I) >= \frac{N_0}{1 - I/I_c} \tag{3.1}$$

where N_0 is the number of magnons in thermal equilibrium, I is the electrical current, and I_c is the critical current at which magnetic damping is fully compensated [106].

This process is depicted schematically in figure 3.1, and is deemed 'spin transfer torque' (STT) a term ubiquitous in modern nanomagnetism research and technology. STT is used to enhance thermal fluctuations of magnetization allowing for the magnetic reversal of magnetic films, the generation of spin waves, and when large enough can completely compensate the dynamical magnetic damping leading to nonlinear effects. This last effect is described in detail in my thesis chapter 7, 'Coherent spin waves generated by spin current in the nonlinear regime'.

STT theory has been effective, and was fundamental to much of the nanomagnetic research that has taken place over the last twenty years. However, it ignores all of the other dynamical excited states in the magnetic system (i.e. spin waves with k$\neq$0), energy conservation, and the bosonic nature of spin waves. Another theory by Berger [107], also published in 1996, is based on a full field field theoretical treatment of spin waves as bosonic systems, in which there is a direct analogy made between the spontaneous and stimulated generation of photons ubiquitous in optics (specifically exploited in the operation of lasers).

To briefly explain, in quantum optics, electrons decaying into a lower energy state from a higher energy state release a photon. The high energy and low energy states of the electron are collectively considered a 'two-level system'. The electronic transition is made more likely when the electrons are perturbed by other photons with the same energy as the energy difference between the two electronic levels, and with polarization that has some projection along the direction of the dipole moment of the electronic transition, the 'transition dipole moment'. This process is deemed 'stimulated emission'. However, even in the absence of additional photons, the excited electron can 'spontaneously' decay to the lower energy state, due to the

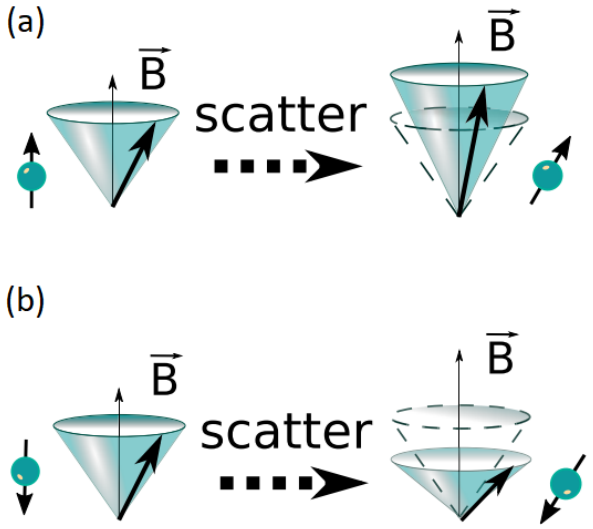

Figure 3.1: Schematic depicting the semi-classical model of spin transfer of spin polarized electrical current driven into magnetic systems deemed 'spin transfer torque' (STT). The magnetic system is modeled as a single spin wave mode (k=0, the FMR mode), in which all spins coherently precess around the magnetization axis, depicted in the schematic as the arrow and cone. The spin from the incoming electron interacts with the FMR mode via the exchange interaction, rotating the incoming spin to be aligned with the spins in the FMR mode. The component of the spin transverse to the spins of the FMR mode is absorbed, leading to a torque that either (a) decreases or (b) increases the amplitude of the FMR mode.

interaction between the electrons and the quantum electrodynamic vacuum (QED vacuum) i.e. quantum fluctuations of the electromagnetic field. Equivalently, these quantum fluctuations can be thought of as fluctuations in the shape of the electronic orbitals, which result in a finite transition rate from the higher to lower electronic energy level. This is a well-established topic, generally taught to varying degrees in a physics student's career, and explained carefully and approachably in 'Introductory Quantum Optics' by Gerry and Knight [43].

One should remember that magnons are also bosons that interact with the electromagnetic field, and can colloquially be thought of as a hybridization between a photon and the spin of an electron. Consequently, there exists a similar process of stimulated and spontaneous emission of magnons. In this case, the 'two level system' is the spin of the electron: either up (majority band) or down (minority band). Berger derived expressions for the stimulated emission of magnons due to current driven into a magnetic material [107]. In this case, the generation of magnons by electrical current excitation is made more likely as the number of magnons present in the system increases. However, in the paper, he makes the approximation that the 'spontaneous' emission is negligible compared to the stimulated process, under most experimentally relevant conditions.

In the following section, I will discuss work in which I was involved where we show that the spontaneous

emission of magnons significantly contributes to magnon generation by spin transfer from itinerant conduction electrons, inconsistent with the semi-classical STT theory. This spontaneous emission of magnons driven by spin polarized electrical current, deemed 'quantum spin transfer', is dominant at temperatures below approximately 150 K in our experiments and calculations, but contributes to the spin transfer process at all temperatures, and generates spin waves of all frequencies and wavevectors (all spin wave modes in the spectrum).

3.2 Magnons generated by current excitation

To arrive at an expression of the number of magnons generated by electrical current excitation including both stimulated and spontaneous emission, we first analyze the process of electron scattering by the active magnetic layer, and how this scattering modifies the dynamical state of the latter. Initially, we focus on scattering of a single spin-polarized electron. The electron is described by the spinor $|s\rangle = (a, b) = a|\uparrow\rangle + b|\downarrow\rangle$, where $|\uparrow\rangle$ and $|\downarrow\rangle$ correspond to the majority and minority spin polarization respectively, and a and b are the complex amplitudes that satisfy $|a|^2 + |b|^2 = 1$. The magnetization is described by a quantum macrospin $|S, S_z\rangle$, where S_z is the projection of the macrospin onto the quantization axis aligned with the equilibrium direction of magnetization, opposite to the direction of the magnetic field B [108, 109]. The interaction between the two spins is described by the standard exchange Hamiltonian $\hat{H}_{ex} = J_{ex}\vec{s}\cdot\vec{S}/S$, where J_{ex} is the Heisenberg exchange constant. As the electron enters the magnetic layer, it starts to experience the exchange interaction, which is described by turning on $\hat{H}_{ex}$. The result of this interaction is precession of both $\vec{s}$ and $\vec{S}$ around the total angular momentum $\vec{J} = \vec{s} + \vec{S}$ conserved by the exchange Hamiltonian.

To describe the time evolution of the incoming spin and the macrospin due to the exchange interaction between the two, the state $|S, S_z\rangle \otimes |s\rangle$ is written in the expanded basis $|J, J_z\rangle$ of the eigenstates of the total angular momentum and its projection on the z-axis. The remaining details that comprise the derivation are about a dozen lines of simple quantum mechanical math. This derivation is carefully outlined in both the supplementary information of the publication of this work [37], and my labmate Andrei Zholud's thesis [14]. I will omit these details to prevent the glazing over of the eyes of the uninterested and the intimidation of young graduate students.

Proceeding to the result, the generation of magnons via scattering from a single electron, in the limit of small magnon populations $N = S - S_z \ll S$, is:

$$< \Delta N > \approx -|a|^2 N/S + |b|^2 N/S + |b|^2/S. \tag{3.2}$$

Eq. (3.2) can be used to describe the effects of electron currents partially-polarized along the z-axis, or impure spin states, by describing the polarization with $p = |a|^2 - |b|^2$. It is easy to see that since only $|a|^2$ and $|b|^2$ enter Eq. 3.2, but not the amplitudes themselves, the result of scattering with initial impure states is the same as with pure states characterized by the same spin projection on the magnetization axis. In this context, the first term on the right can be interpreted as stimulated absorption of magnons by the majority spin electrons ($a = 1$, $b = 0$). The second term represents stimulated emission of magnons by minority spin electrons ($a = 0$, $b = 1$), and the last term is the spontaneous emission by minority spin electrons, present even in the absence of magnons [107]. The generation of a magnon flips the spin of the incoming spin, due to conservation of angular momentum.

In the steady state, the magnon population is determined by the balance between spin transfer driven by current I, and the dynamical relaxation. Describing the latter by Landau damping, or equivalently for small N by the relaxation time approximation $\frac{\partial N}{\partial t}|_{rel} = -\frac{N-N_0}{\tau}$ [107, 108] with $\tau = 1/(2\alpha\omega)$, where ω is the FMR mode frequency, one can calculate:

$$< N(I) >= \frac{N_0 + (|I|/p + I)/2I_c}{1 - I/I_c}, \tag{3.3}$$

where $p = |a|^2 - |b|^2$ describes the current polarization. The unusual non-analytical form of Eq. (3.3) originates from the asymmetry of Eq. (3.2) with respect to exchange of a and b describing current reversal. Note that Eq. (3.3) does not diverge at $p = 0$, since $I_c \propto 1/p$.

In the classical limit $N_0 \gg 1$, the spontaneous contribution in Eq. (3.2) is negligible, and Eq. (3.3) reduces to the STT result in equation. (3.1). In the quantum limit $N_0 \ll 1$ at $T \ll \hbar\omega/k_B$, we obtain a piecewise-linear dependence of N as a function of current. In the next section, I will show how this functional form of magnon generation can be experimentally measured.

3.3 Relation between magnon population and magnetoresistance of nanomagnetic spin-valve

In this section, I will show how the common magnetoelectronic measurement technique, giant magnetoresistance (GMR), can be used to observe the current dependent magnon generation given in equation 3.3, and ultimately show the significant effects from the spontaneous emission of magnons. For a more detailed description of the GMR effect, read the section 'Measurement technique: Giant Magnetoresistance' in the thesis chapter 2, 'Spin Relaxation in Pt'.

A spin-valve is a common nanomagnetic device, where two magnetic films are separated by a nonmagnetic

spacer. Spin-valves are a standard device used to measure GMR, which results in a sinusoidal dependence of resistance on the angle between the magnetizations of the two ferromagnetic layers forming the spin valve, with the period of 2π [60, 76, 110],

$$R(\theta) = R(0) + \Delta R \sin^2\left(\frac{\theta}{2}\right) \tag{3.4}$$

where $R(0)$ is the resistance minimum in the parallel configuration, ΔR is the magnetoresistance, and θ is the angle between orientations of the magnetizations of free layer F1 and of the polarizer F2. At finite magnon population in the free layer, the magnetization $\vec{M}$ precesses around its equilibrium orientation, aligned with the magnetic field, at an angle θ. Each generated magnon decreases the projection of the magnetic moment on the equilibrium axis by μ_B/V, shown schematically in figure 3.2, where μ_B is the Bohr magneton, and V is the volume of the free layer. Thus, the magnon population in the FMR mode is related to the precession angle by

$$M_z = MV\cos\Theta = MV - N\mu_B \tag{3.5}$$

By combining Eq. (3.4) and Eq. (3.5), we determine the relationship between the magnon population and the resistance of the nanopillar:

$$N = \frac{MV(R(\Theta) - R_0)}{2\mu_B \Delta R} \tag{3.6}$$

Here, we focus only on the "active" magnetic free layer F1, whose magnon population is affected by the spin-polarized current. Fluctuations in the other magnetic layer, the "polarizer" F2, are assumed to be determined entirely by temperature T, and are accounted for by the value of ΔR in Eq. (3.4). We note that the dipolar effects determined by the geometry of the ferromagnet result in variations of R on the timescale of magnetization dynamics, due to the ellipticity of the precession orbit. These effects result in a scaling correction to Eq.(3.6) by a factor of order 1, with the value of R representing an average over this timescale. The linear relation between N and R must hold not only for FMR, but also for other magnon modes, because their local description in terms of precession angle is the same, while the GMR results from the electron scattering by the local magnetization configuration. To reinforce this argument, consider an arbitrary spin wave mode with the largest possible mode population describing a reversed magnetization state. In this case, Eq.(3.4) is clearly applicable regardless of the spatial characteristics of the mode. For smaller magnon populations, electron spin diffusion across a magnetically inhomogeneous state should result in corrections to Eq.(3.4) of the order one. The argument presented above for a single mode also holds for the time-averaged value of R in excited states involving multiple dynamical modes, and therefore Eq.(3.4)

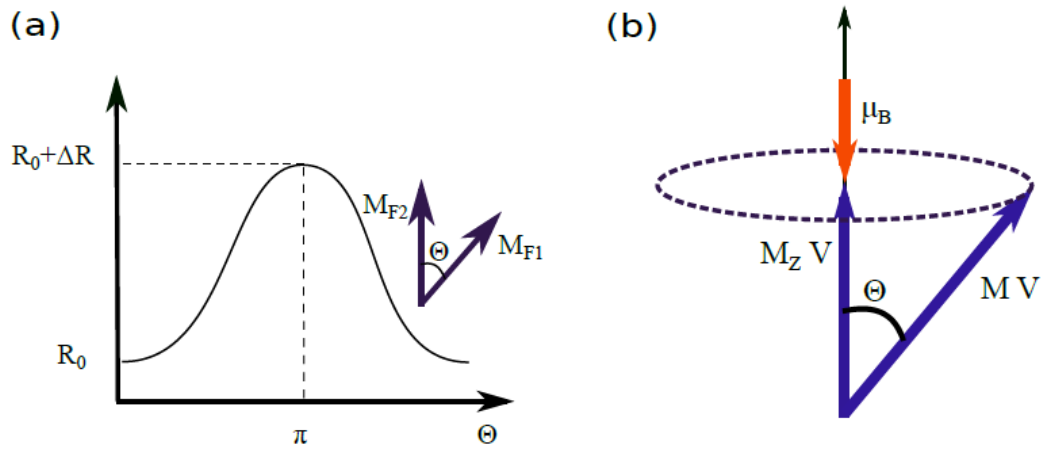

Figure 3.2: (a)Schematic depicting the change in the resistance of a magnetic bilayer as a function of the angle between the magnetizations of the two layers. (b) Schematic depicting the generation of a magnon, and the corresponding decrease in the projection of the magnetization on the equilibrium axis by μ_B/V. Reproduced with permission from [14].

applies to the total magnon population. Thus, GMR results in a linear relationship between resistance and the total magnon population in the nanomagnet, not limited to quasi-uniform modes. We therefore use the magnetoelectronic measurement GMR as a probe of the number of magnons present in a magnetic film as a function of the current driven through the sample, allowing us to show the significance of the spontaneous emission of magnons.

3.4 Magnetoelectronic measurements and calculations of spontaneous and stimulated emission of magnons

In this section I show how GMR measurements on Py based nanoscale spin-valves was used to determine the effect of current driven spin transfer on the number of magnons present one of the magnetic layers of the spin-valve.

We analyze the differential resistance at subcritical currents, for various strengths of external magnetic field, as exemplified in figure. 3.3. Figure 3.4 shows the current dependent differential resistance of the spin-valve for different values of large, saturating external magnetic field, The current dependence exhibits an unusual piecewise-linear shape, with the slope larger for $I > 0$ than for $I < 0$. The curves are shifted by the field, which can be explained by the magnon freeze-out, as illustrated in figure. 3.4(b) that shows the field dependence of resistance at $I = 0$ together with the calculated field-dependent thermal magnon population. Since field variation does not noticeably affect the slopes of the curves in Fig. 3.4(a), the observed piecewise-

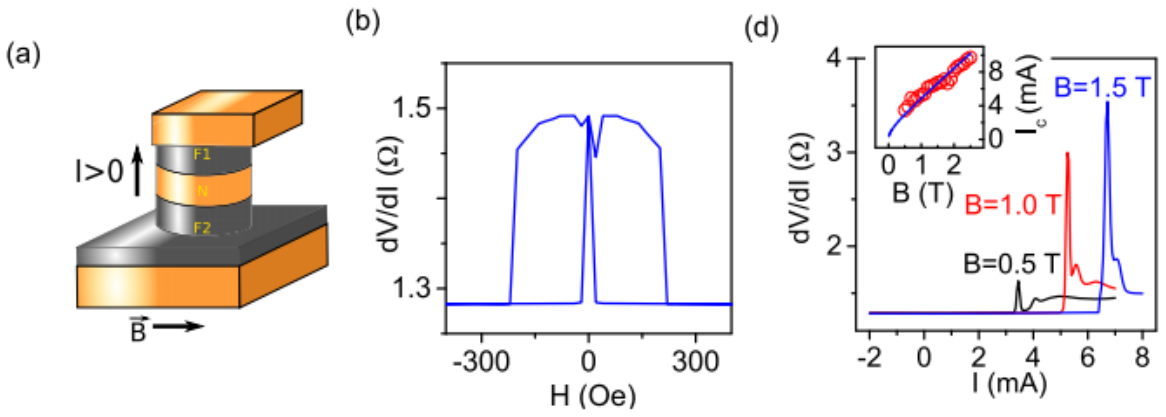

Figure 3.3: (a) Schematic of the tested spin-valve nanopillar. Grey: Permalloy (Py) "free" layer F1 and "polarizer" F2. Orange: Cu electrodes and spacer N. (b) The magnetoelectronic hysteresis loop: differential resistance vs applied magnetic field, representing a standard GMR measurement. (c) Differential resistance vs current, at the labeled fields. Inset: Critical current I_c for the onset of auto-oscillation vs field determined from the experimental data (symbols), and the calculation (curve). All measurements were performed at 3.4 K

linear dependence cannot be associated with thermal fluctuations whose intensity is controlled by the field. It cannot be explained by Joule heating, because the dissipated power, and thus the resulting resistance increase, is quadratic in current. It is also inconsistent with the analytical expression Eq. (3.1) of spin torque theory. Electronic shot noise exhibits a similar linear increase of power with bias [111]. However, shot noise (fluctuating current) can contribute to the differential resistance only by inducing magnetization fluctuations, which in the absence of thermal fluctuations is forbidden by the angular momentum conservation argument of spin torque theory.

We conclude that a previously unrecognized contribution to spin transfer, not described as enhancement of thermal magnetization fluctuations, results in a linear increase of magnon population with current. To interpret our observations, we note that even if thermal fluctuations are negligible at low temperature, the polarization of the scattered electrons cannot be perfectly aligned with the magnetization because of the quantum fluctuations of the latter, leading to electron spin dynamics driving spin transfer. The proposed quantum effect must be distinct from STT described by Eq. (3.1). In particular, in contrast to thermal fluctuations, quantum fluctuations cannot be suppressed by scattering of the majority electrons, due to the uncertainty principle [Fig. 3.4(c), top]. However, they can be enhanced by scattering of the minority electrons [Fig. 3.4(c), bottom]. To satisfy angular momentum conservation, the transverse to the field component of the magnetization must remain zero. The resulting substantially non-classical magnetization state cannot be described by rotation from the initial state, and therefore the proposed effect is not a torque.

In the following, we analyze this piecewise-linear dependence of the resistance in terms of equations 3.3 and 3.6 described above, in which the increase in resistance is due to the spontaneous and stimulated emission

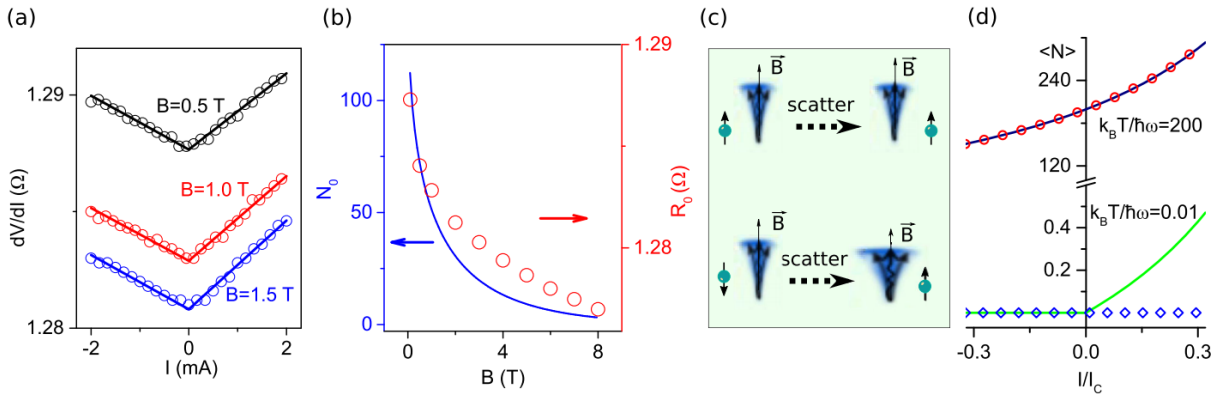

Figure 3.4: (a) Differential resistance vs current, at the labeled values of field and $T = 3.4$ K. Symbols: data, lines: best linear fits performed separately for $I < 0$ and $I > 0$. (b) Differential resistance (symbols, right scale) and the calculated total magnon population (curve, left scale) vs B at $I = 0$. (c) Scattering of the majority (top) and the minority (bottom) electron by magnetization experiencing only quantum fluctuations. Vectors show the direction of the fluctuating magnetization and the magnetic moment of the scattered electron. (d) Curves: population of a magnon mode with frequency ω vs current, as described by Eq. (3.3), in the classical limit $k_BT/\hbar\omega = 200$ and in the quantum limit $k_BT/\hbar\omega = 0.01$, for $p = 1$. Symbols: calculation using Eq. (3.1) for $k_BT/\hbar\omega = 200$.

of magnons.

We now discuss the significance of the proposed quantum contribution to spin transfer. Since exchange interaction between the electron spin and the magnetization underlying spin transfer is local, Eq. (3.3) with mode-dependent values N_0, I_c, must be applicable not only to FMR, but also to the nonuniform modes [112]. The quasi-uniform modes with frequency f of a few GHz are degenerately populated at 3.4 K, so the contribution of their quantum fluctuations to spin transfer, i.e. spontaneous emission from these low frequency modes, is negligible. However, the modes with $f > 70$ GHz are frozen out, and therefore the high frequency magnons excited by spin transfer at low temperatures are expected to be primarily from spotaneous emission. Summation of Eq. (3.3) over the magnon spectrum confirmed that the contribution of spontaneous emission to the total current-dependent magnon population is dominant at 3.4 K, consistent with our interpretation of Fig. 3.4(a). We note that for short-wavelength modes, additional resonant contributions may arise due to the interplay between the magnetization dynamics and orbital electron motion; we leave their analysis to future studies.

At higher temperatures, the zero-current singularity becomes rapidly broadened [Fig. 3.5(a)]. This cannot be attributed to the increasing role of thermal magnetization fluctuations, since the piecewise-linear dependence is still apparent at larger currents even at 20 K. To analyze this effect, we fit the data with a piecewise-linear dependence convolved with a Gaussian. The extracted broadening closely follows a linear dependence $\Delta I = (1.9 \pm 0.1) k_BT/eR_0$, where R_0 is the resistance at $I = 0$ [inset in Fig. 3.5(a)]. This result is

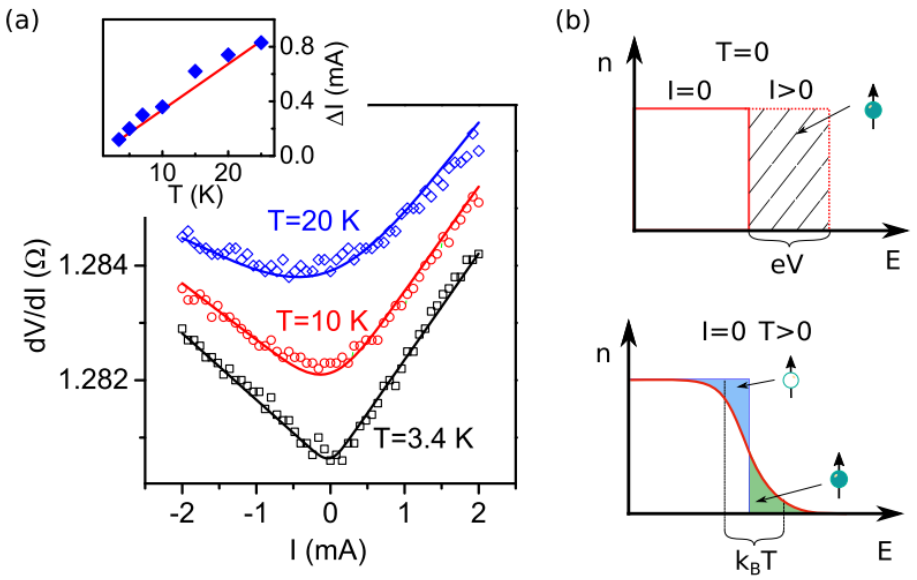

Figure 3.5: (a) Symbols: differential resistance vs current, at the labeled values of temperature and $B = 1$ T. Curves: results of fitting with a piecewise-linear dependence convolved with a Gaussian whose width is used as an adjustable parameter. Inset: temperature dependence of the Gaussian width extracted from the fitting (symbols), and $\Delta I = 1.9 k_B T/eR_0$ (line). The data are offset for clarity. (b) Top: at $T = 0$, the Fermi distribution of scattered electrons is step-like. Bias current shifts the distribution, driving the spin transfer. Bottom: at finite T, scattering of thermal electrons and holes occurs even at zero bias, equivalent to bias distribution of width $k_B T/e$.

consistent with the proposed quantum mechanism. Bias current shifts the electron distribution in the nanomagnetic spin-valve, driving spin transfer [Fig. 3.5(b), top]. At finite temperature, the electron distribution becomes thermally broadened, resulting in scattering of thermally excited electrons and holes [Fig. 3.5(b), bottom] equivalent to a distribution of width $\Delta V = k_B T/e$ of the bias voltage applied to F1, facilitating spin transfer even in the absence of directional current flow. The relation $\Delta I = (1.9 \pm 0.1) k_B T/eR_0$ is consistent with the approximately equal contributions of layers F1 and F2 to R_0, such that $\Delta V \approx IR_0/2$. Thermal broadening is absent for STT, because the effects of electron and hole scattering cancel each other.

We now analyze the temperature dependence of spin transfer. We convolve Eq. (3.3) with a Gaussian, to account for thermal effects discussed above, and take a derivative with respect to current. At $I = 0$, we obtain

$$\frac{dN^{(\mathbf{i})}}{dI}|_{I=0} = \frac{1}{2I_c^{(\mathbf{i})}} + \frac{N_0}{I_c^{(\mathbf{i})}}, \tag{3.7}$$

where i indicates the excited magnon mode number. The first term on the right, describing the quantum contribution to current-dependent magnon population, i.e. spontaneous emission, is independent of temperature. The last term describing STT decreases with decreasing T, and vanishes at $T = 0$. We define

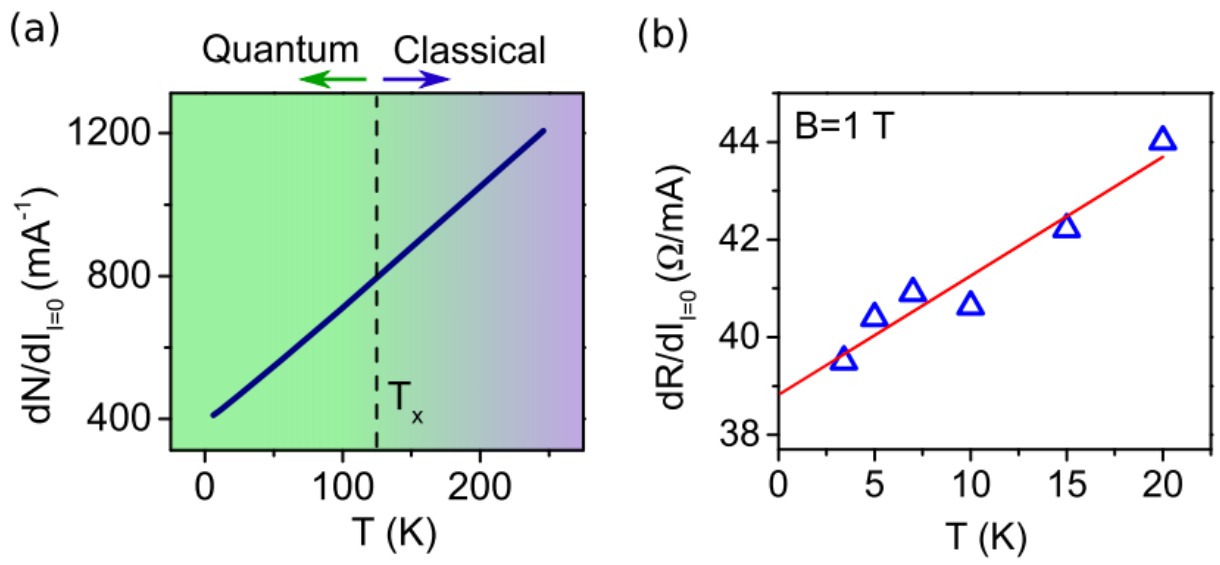

Figure 3.6: (a) The calculated slope dN/dI vs T, $B = 1$ T. Vertical dashed line marks the crossover temperature T_x between the quantum and the classical spin transfer regimes. (b) Symbols: The slope dR/dI of resistance vs current at $I = 0$ and $B = 1$ T. Line: best linear fit of the data.

T_x as the crossover temperature at which the two contributions become equal. Figure 3.6(a) shows the calculated temperature dependence of $dN/dI_{I=0}$ for the total magnon population at field $B = 1$ T, obtained by summing Eq. (3.7) over all the magnon modes. The increase with temperature associated with STT is approximately linear, indicating that the classical contribution is dominated by the degenerately populated modes described by the Rayleigh-Jeans law, i.e. the Bose-Einstein distribution in the limit of high temperature. Based on these calculations, $T_x = 126$ K for the total magnon population. The measured dR/dI, which is proportional to dN/dI, increases linearly with temperature, with a non-zero $T = 0$ intercept [Fig. 3.6(b)]. We use linear extrapolation to estimate $T_x = 160$ K, in a good agreement with calculations. If a single mode were involved in STT, the value of T_x would characterize the frequency of this mode $f_0 = 2k_BT_x/h \approx 7$ THz [see Eq. 3.7]. This result confirms that spin transfer involves high-frequency dynamical modes extending into the THz frequency range.

The presented results have significant implications for magnetoelectronic effects in a variety of magnetic systems. Quantum fluctuations can contribute to current-induced phenomena whenever highly nonuniform dynamical states are involved, for example in reversal via domain wall motion [113]. Generally, the quantum magnon generation decreases the effective magnetization, lowering the reversal barriers. The contribution of quantum fluctuations to spin transfer in antiferromagnets [114] must be larger than in ferromagnets. This is due to higher magnon frequencies (energies), leading to more significant magnon freeze-out effects. Quantum fluctuations may contribute to other phenomena involving interaction between magnetization

and conduction electrons, including spin pumping [115], spin-orbit [33], optically-driven [116], and spin-caloritronic effects [117].

We also infer a significant inelastic contribution to spin-dependent electron transport in ferromagnets due to quantum electron-magnon scattering. It is presently believed that currents flowing through ferromagnets become spin-polarized mainly due to spin-anisotropy of electron scattering. Meanwhile, according to Eq. (3.2), an unpolarized conduction electron scattered by the ferromagnet generates a magnon in a given dynamical mode with probability $1/2S$, where S is the total spin of the ferromagnet; it becomes majority spin-polarized in this process. The number of modes is of order S [118], and therefore the total probability for an initially unpolarized electron to become majority-polarized due to quantum magnon generation is of order 1. This result shows that inelastic scattering of electrons by quantum magnetization fluctuations provides a non-negligible contribution to spin-polarizing properties of ferromagnets.

Chapter 4

Anti-Reflective Coating for THz Nano-antennae

4.1 Introduction and Background on THz light-matter interaction

Sources and detectors of terahertz (THz) frequency electromagnetic radiation are relatively new compared to microwave and optical sources. Within the last two decades, the development of intense, coherent laser-based THz sources has allowed scientists and engineers to use this type of radiation to coherently control and study the properties of materials on the sub-picosecond time scale [119]. For example, in the context of nanomagnetism, THz lasers have been used to drive specific mechanisms of ultrafast demagnetization, the understanding of which is critical for the development of fast nanomagnetic devices [120]. Furthermore, THz photons, with energies in the meV range, can drive nonlinear dynamics without significantly increasing the entropy of the system [120–132], have been used to for spectroscopy and characterization of various physical properties of semi-conductors [119], and time resolved measurements of vibrational modes (phonons) in crystals [133]. In the field of condensed matter physics, the investigations of ultrafast dynamics driven by strong terahertz fields are frequently performed using terahertz-pump (usually in the 1 - 10 THz range, 300 to 30 μm in wavelength) and visible or near-infrared probing light (typically a sub-100 fs pulse).

To study the effects in the strong-field limit, the strength of the terahertz field can be locally enhanced exploiting near-field effects in meta-materials [121, 134–139], which typically consist of micrometer-sized metallic structures deposited on the sample surface. However, since the area of the sample is often significantly smaller than the area of metallic structures in meta-materials, the reflectivity in the visible or near-infrared frequency range of the probe is dominated by the latter. As a consequence, it is extremely

challenging to isolate the sample response, despite the enhancement provided by the meta-material. This problem can be mitigated by using dielectric and absorbing coatings, for instance to enhance the magneto-optical activity in magnetic thin films, and to reduce the background reflections [140–145]. This solution greatly boosts the signal up to a point where single nano-structures can be measured. The drawback of this approach is that it imposes constraints on the choice of layers underneath the target structure. This limitation can become crucial if these underlayers are utilized to tune the important properties of the studied thin films. In this case, a more suitable solution is to deposit an anti-reflection (AR) coating only on the metal structures forming the meta-material, to minimize the reflection from those areas, which is the main factor affecting the strength of the measured signal. At the same time, the AR layer should not perturb the terahertz radiation that still needs to be enhanced by the metal layers.

The work described in this chapter outlines experimental and simulation results on a single-layer anti-reflection coating design that can be implemented on arbitrary meta-material structures comprising highly conducting and reflective metallic layers. The working principle is simple, and has been implemented in a wide variety of other applications at various operating frequencies, but this work marked the first time it was used in the context of nanoscale THz metamaterials. In general, the infancy of THz technologies means that there are still many 'low hanging fruit' to be picked in the research areas of THz physics. The anti-reflective coating discussed here suppresses the near-infrared reflection typically utilized to probe the response of the sample, without noticeably affecting the terahertz radiation used for excitation of the magnetic nanostructure. Transfer matrix method calculations were performed, as well as measurements of the reflectivity both in the near-infrared and terahertz range, to demonstrate the functionality of the design. We have also investigated, using time-domain finite element simulations, the near-field enhancement properties of a dipole antenna - a template for the terahertz meta-materials - covered with the anti-reflection coating. As the experimental proof of principle, we experimentally measured the magneto-optical Kerr effect (MOKE) [1, 16, 18] from a magnetic wire placed in the gap of the antenna.

4.2 THz Meta-Material (Nano-antenna)

Terahertz meta-materials can be formed by depositing metallic (typically gold) layers that can locally enhance the electromagnetic field of incident radiation. One of the simplest realization of such structure consists of two metallic strips separated by a small gap, i.e. a dipole antenna [146]. For a suitable geometry of the antenna and polarization of the incident radiation, opposite charges can be induced by the electromagnetic field at the opposite edges of the gap, producing a strong local enhancement of electric field within the gap. Intuitively, but incorrectly, this charge motion is often attributed to the current driven by the electric field.

However, the correct explanation is that the local electric field enhancement in the gap is caused by the screening of the magnetic field, which induces a current flow in the metal, in the direction orthogonal to it (parallel to the electric field). This counter-intuitive electromagnetic response is an interesting example of how intuition derived from the macroscopic world at technologically common frequencies often doesn't apply at nanoscale or uncommon frequency ranges. The current flow induced by the magnetic field, known as the eddy current, can penetrate within the skin depth of the material (75 nm at 1 THz for gold). In contrast, the electric field component of the radiation is screened virtually instantaneously at the surface of the conductor by the charge redistribution, and at terahertz frequencies provides a negligible contribution to the net current flow in the bulk of the material, even in non-ideal metals.

4.3 Anti-Reflective Coating

In the standard AR coatings, designed to minimize the reflection from dielectric materials, one exploits the phenomenon of destructive interference of the waves reflected at the two interfaces, to cancel the total electric field that propagates in the backward direction. Since the energy of the electromagnetic wave is conserved, the transmission through the dielectric is maximized. However, this mechanism cannot be implemented for coatings on metals, since the wave cannot propagate through the metal, and hence the reflection cannot be eliminated. Colloquially, the energy has to go somewhere.

For an AR coating to work for a metal, it is necessary to create destructive interference (to suppress Fresnel reflections), and to simultaneously absorb the radiation, as shown schematically in Fig. 4.1. In other words, the dielectric layer needs to be sufficiently lossy in the visible/nearinfrared region, so that the wave decays after multiple reflections at the interfaces. This idea was proposed decades ago by Hass et al. [147], who demonstrated that lossy double dielectric layers can suppress the reflectivity of aluminum and copper in the visible range, while maintaining high-reflectivity in the mid-infrared range, up to the wavelength of 10 μm. Moreover, they also highlighted the fact that absorption in single-layer AR coatings is necessary to reduce the high reflectance of metals in the visible range.

In the following, we experimentally confirm that the reflection from gold, and hence from any good metal, can be suppressed by using a single layer of sputtered amorphous silicon (α-Si). In the visible/near-infrared range, a thin α-Si film acts as a dielectric with a relatively large imaginary part of the refractive index, since the electronic states are not characterized by well-defined momentum, enhancing the radiation absorption in α-Si as compared to its crystalline form [148]. On the other hand, low absorption in the terahertz range ($\lambda \approx 100$ μm), and the small thickness compared to the radiation wavelength, make these layers practically invisible, thus maintaining the high-reflectivity characteristics of gold in this range.

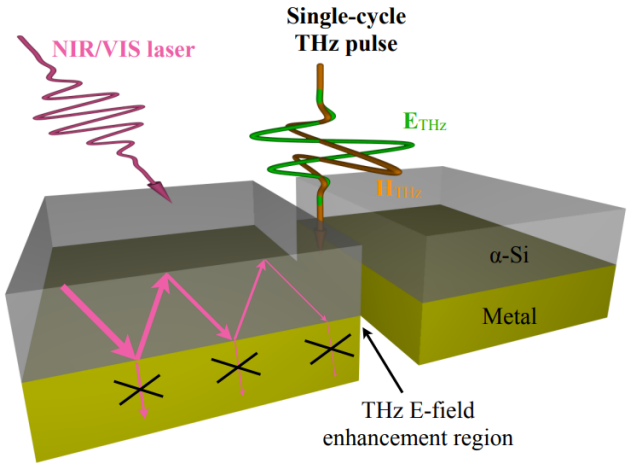

Figure 4.1: Design of the dipole antenna for terahertz near-field enhancement in the gap between two metallic electrodes, covered with an anti-reflection coating for near-infrared and visible radiation. A single-cycle of the terahertz field, with the suitable polarization for the optimal coupling to the antenna, is sketched. The pink arrows schematically show the working principle of the anti-reflection coating for a metal, where destructive interference (zig-zag arrows within the top layer) is combined with the dielectric losses to compensate for the forbidden transmission through the metallic electrodes (crossed-out arrows in the metal layer), as described in detail in the text.

The transfer matrix method (TMM) [149] was used to simulate the feasibility of this approach. We simulated the Air/α-Si/Au/Si(substrate)/Air multilayer, where the outermost Air layers were semi-infinite, and the substrate was 500 μm thick. The radiation was assumed to be monochromatic with a wavelength of 800 nm, the typical center-wavelength of a Ti:sapphire laser, at a normal incidence to the multilayer stack. We used the refractive indices $n_{Air} = 1$, $n_{\alpha-Si} \approx 3.90 + 0.11i$, $n_{Au} \approx 0.15 + 4.91i$, and $n_{Si} \approx 3.681 + 0.005i$.

In Fig. 4.2 we plot the reflectance of the stack as a function of the α-Si thickness, for two gold layers with different thickness. For thin gold (20 nm), part of the radiation can be transmitted into the substrate, and approximately 30 nm of amorphous silicon on top of it can efficiently suppress the reflectivity. For thick gold (100 nm), enough to prevent any transmission, a thicker amorphous silicon layer ($\approx$ 230 nm) is needed to achieve the same suppression. In the same figure, we also plot the reflectivity (dashed lines) of a fictitious dielectric layer with zero imaginary part of the refractive index, and its magnitude equal to that of the the amorphous silicon, representing a conventional dielectric with negligible losses. It is evident that such a layer on top of a 100-nm thick gold layer cannot efficiently suppress the reflectivity, demonstrating that the cumulative losses after multiple reflections are necessary to realize the anti-reflection configuration.

We note that a single α-Si anti-reflection coating remains efficient over a broad range of incidence angles. We used TMM to check that, when varying the incidence angle from 0 to 37.5 degrees, the optimal thickness for the α-Si layer varies by less than 2%. Furthermore, at the optimal thickness, the 800 nm reflectance remains below 0.05 (an acce ptable value for the coating to properly work), at angles of incidence as high as

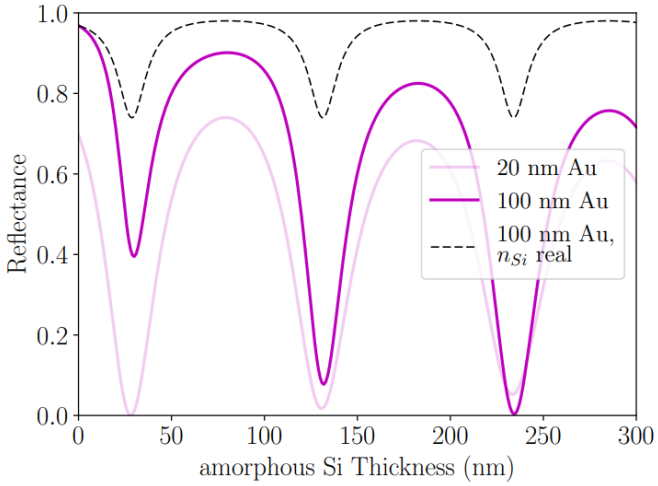

Figure 4.2: Solid curves: Calculated reflectance at the wavelength of 800 nm for the Air/αSi/Au/Si(substrate)/Air multilayer, as a function of the α-Si thickness, for two different Au thicknesses at normal incidence. Dashed curve: Calculated reflectance at a wavelength of 800 nm for an ideal dielectric on top of a 100 nm Au layer, characterized by n = 3.9 and zero imaginary part of the refractive index.

50 degrees. This can be understood as a consequence of the large refractive index of silicon, which causes the electromagnetic wave to strongly refract when entering the AR layer. As a result, the optical path in the silicon layer noticeably increases only at very large angles of incidence.

In Fig. 4.3, we plot the calculated and the measured reflectance for several Air/ α -Si(t)/Au(20nm)/Si(substrate)/Air multilayers, as a function of t, both for 800 nm and for the terahertz radiation impinging on the sample at 10 degrees incidence. The 800 nm radiation was produced by the Ti:sapphire-based regenerative amplifier (Coherent Legend) in 40 fs pulses, with the 30 nm FWHM bandwidth around the center 800 nm wavelength, as measured by a grating spectrometer. The reflectance at 800 nm was measured directly using a photodiode. The signal was scaled using the known reflectance value of a commercial gold mirror. The reflectance R of the terahertz radiation, generated by optical rectification in a OH1 organic crystal [150], was determine from the measured transmittance T, using $R = 1 - A - T$, where the absorption A was calculated based on the TMM. The transmittance was taken to be proportional to the square of the normalized amplitude of the maximum electro-optical sampling signal in a 100 μm thick, 110-cut GaP crystal.

The excellent agreement between the data and the calculations directly demonstrates the functionality of our design in suppressing the near-infrared reflectivity, with the appropriate thickness of α-Si, 27 nm and 127 nm in the studied case of 800 nm radiation. We emphasize that our experiment demonstrates efficient suppression of the broadband 40 fs pulses of 800 nm radiation. This result confirms the suitability of our design for the conventional ultrafast experiments. On the other hand, the terahertz reflectivity is unchanged

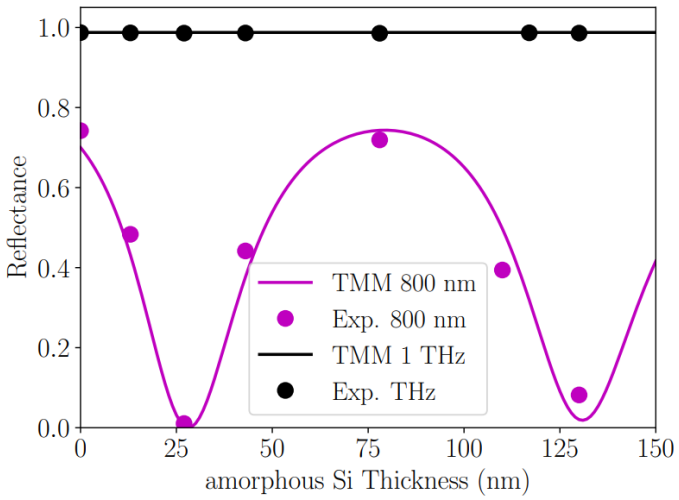

Figure 4.3: Experimental (symbols) and calculated (line) reflectance for a α-Si/Au/Si(substrate) sample based on a 20 nm-thick Au layer, at wavelengths of 800 nm (magenta) and 300 μm (black), the latter corresponding to the radiation frequency of 1 THz

by the α-Si layer, suggesting that the terahertz near-field enhancement is also likely unaffected the silicon layer. However, since the measured reflectivity is a far-field property, and near-field properties are in general very sensitive to interface effects, one needs to perform a more detailed investigation of the possible effects of the anti-reflection coating on the terahertz radiation in the near-field regime.

4.4 Simulated Near-Field

To analyze the near-field effects of the coating, finite-element numerical calculations were performed using COMSOL Multiphysics software. In Fig. 4.4(a), we plot the electric field enhancement at a frequency of 1 THz, for a set of two infinitely long, 5 μm wide, 20 nm thick gold plates separated by a gap of 2 μm. The terahertz electric field is applied along the x - axis in this figure. The field enhancement is computed by dividing the electric field value in the gap region by the electric field value at the air/silicon interface, in the absence of the gold plates. In Fig. 4.4(b), we plot time-dependence of the x - component of the terahertz electric field in the middle of the gap (x = 0), and at z = 10 nm above the silicon substrate. The simulation used the experimental time profile of the impinging terahertz field, measured by electro-optical sampling, with the peak value of $\approx$ 300 kV/cm.

For the bare silicon-air interface, the terahertz field is reduced to approximately half of its free-space magnitude, consistent with the relative amplitude of the transmitted wave at an air/silicon interface computed as $t = 2/(n+1)$, with n $\approx$ 3.4. The presence of the gold plates introduces a slight temporal shift, and enhances the amplitude of the terahertz field to more than 500 kV/cm, consistent with the $\approx$ 4 times enhancement

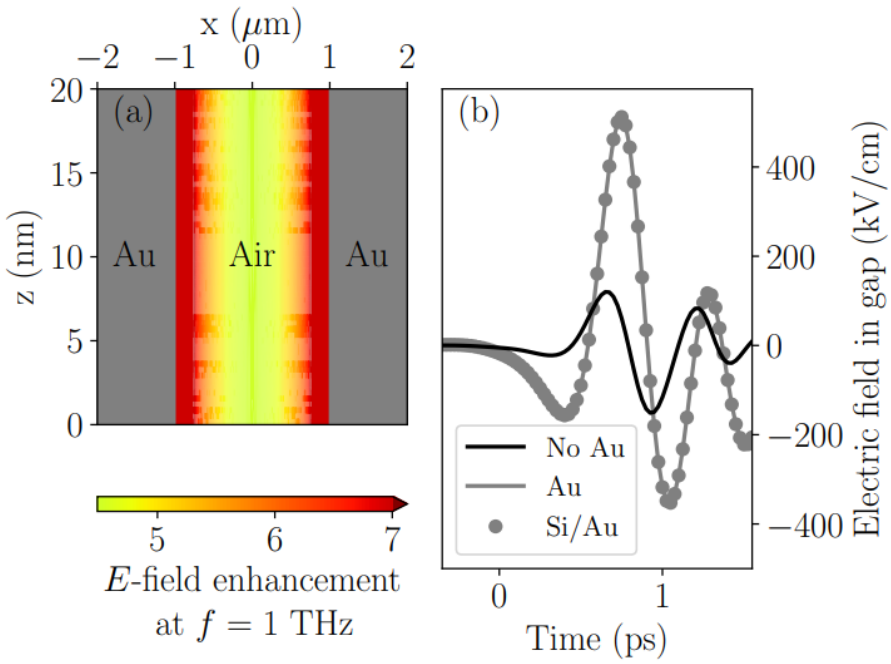

Figure 4.4: (a) Frequency-domain, finite element analysis of the enhancement map for a monochromatic electromagnetic field with frequency f = 1 THz incident on two gold plates separated by a gap. (b) Time-domain finite element simulations of the x - component of the electric field for a single-cycle (broadband) terahertz field at the center of the gap, without Au plates (solid black curve), with Au plates (solid gray curve) and with α - Si/Au plates (filled gray dots). In all the calculations, the electric field of the incident radiation is polarized along the x axis, and the propagation direction is along the z axis, normal to the sample plane.

observed in the frequency domain simulations of Fig. 4.4(a). Most importantly, the addition of the α-Si layer on top of the gold plates does not noticeably affect the field, confirming our intuitive conclusions based on the negligible effect of the α-Si layer on the terahertz reflectivity.

4.5 Magneto-optical Measurements on Magnetic Nanowire using Anti-Reflective Coating

To test the functionality of the AR coating in a practical configuration, we measured the polar magneto-optical Kerr effect (MOKE) from the 3 nm-thick CoNi film patterned into a 1 μm wide, 100 μm-long wire. The CoNi stack is formed by a Ta(2)/Cu(2)/[Co(0.2)/Ni(1)]x3/Ni(0.5)/Ta(3) multilayer (thicknesses in nm) with perpendicular magnetic anisotropy. The wire is located in the 2 μm wide gap between two 100μm long and 65 μm wide gold plates, coated with 27 nm of α-Si. By analyzing the magneto-optical response, we can unambiguously identify the signal coming from the embedded CoNi wire, with no contribution from the non-magnetic electrodes. As the MOKE signal typically results in a tiny intensity variation on top of a large background, this specific system implementation also demonstrates the general suitability of our design for the detection of small effects other than magneto-optical ones.

The polar MOKE loops from the embedded wire are plotted in the main panel of Fig. 5 for two different wavelengths of the probing radiation, 550 nm and 800 nm. At 800 nm, the AR coating optimized for this wavelength is expected to completely suppress the reflectivity of the gold electrodes, while at 550 nm, a substantial reflection from the metallic pads is expected. Using radiation of different wavelengths is geometrically equivalent to studying samples with different AR coating thickness, with the advantage that the very same sample can be used and the wavelength can be tuned very accurately.

The plotted MOKE signals reflect the change in the polarization ellipticity of the probing light,determined with a suitable polarization analyzing system. In these measurements, a polarization modulation technique [151] was used to provide the sensitivity necessary for testing the effectiveness of the proposed AR coating. In this setup, the polarization of the incident light was modulated at the frequency ω, while both the total measured intensity I_0 and its variation I_ω at the modulation frequency were simultaneously recorded. The polarization ellipticity was determined from I_ω normalized by the total intensity I_0 reflected from the sample. While the variations of I_ω were affected only by the magnetic structure, the magnitude of I_0 is determined by the whole probed area, including the gold plates. The working principle behind this measurement technique is similar to lock-in detection, described elsewhere in this thesis, where noise can be eliminated from a measurement of the response to a driving force, by measuring at the frequency of the driving force.

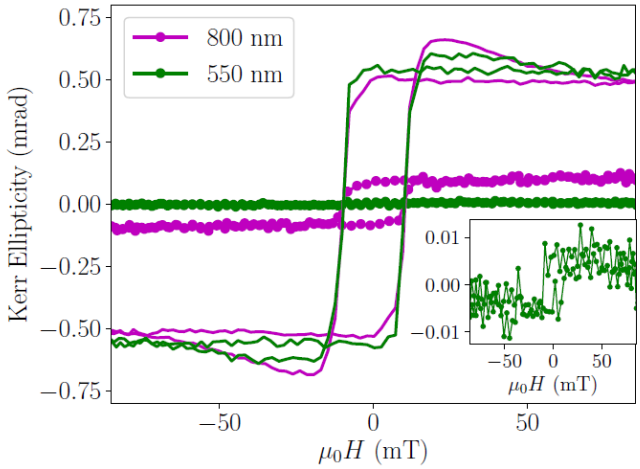

Figure 4.5: Polar Kerr ellipticity as a function of the magnetic field applied orthogonal to the sample plane, for the 800 nm and 550 nm wavelengths of the probing light. Symbols: average of 25 hysteresis loops for a 1μm-wide, 100μm - long CoNi wire. Solide curves: average of 4 hysteresis loops for a 100 μm x 100 μm CoNi square, at the same wavelengths. Inset: Zoom in on the 550 nm wavelength hysteresis loop for the CoNi wire.

The data plotted with symbols in Fig. 4.5 clearly show that the AR coating significantly enhances the signal-to-background ratio, resulting in a more than a ten-fold increase of the relative amplitude of the loop at the designated wavelength. We have checked that the increase in the relative signal is not caused by the difference between the magneto-optical constants of CoNi between 800 and 550 nm wavelengths, by measuring the MOKE signal from a 100μm x 100μm CoNi square of 3 nm thickness, with no gold electrodes surrounding the structure. The resulting hysteresis loops are shown with solid curves in the the same Fig. 4.5.

4.6 Summary

In summary, this chapter discussed the design and experimental implementation of an anti-reflective (AR) coating for highly reflective elements commonly used in THz pump-probe experiments. The specific system in which we implemented this coating was a pair of Au THz patch antennas, sandwiching a magnetic wire. The magnetic field from a THz laser excites eddy currents in the Au antennae, generating large THz electric fields in the magnetic wire. An optical laser then detects the magnetization of the magnetic wire. Without the AR coating, the magneto-optical signal is dominated by the Au patch antennae. The AR coating allows the magnetization of the magnetic wire to be measured magneto-optically with much larger signal to noise than what is possible without the coating. Specifically, this type of AR coating can be useful for magneto-optical measurements of THz-driven 'ultrafast' demagnetization. Generally, similar AR coatings can be easily integrated into a variety of 'pump-probe' measurements that use large reflective antenna, whenever

the pumping wavelength is significantly different than the probing wavelength.

Chapter 5

Brillouin Light Spectroscopy from Spin Waves Inaccessible with Free-Space Light

5.1 Background of Brillouin Light Spectroscopy

Brillouin Light Scattering is a process by which a photon inelastically scatters off of a dispersive electromagnetic excitation such as a spin wave (magnetic excitations, quantized as 'magnons') or a phonon (vibrational mode), as shown schematically in the inset of Fig. 5.1a. The selection rules underlying this scattering process are energy, linear momentum, and angular momentum conservation: $f_1 = f_2 + f_{exc}$, $k_1 = k_2 + k_{exc}$, and $l_1 = l_2 + l_{exc}$. Angular momentum conservation is often not discussed in texts about BLS, but spin waves are excitations with quantized angular momentum, and consequently scattering between a spin wave and a photon rotates the polarization state of the photon.

By measuring the intensity of the scattered light as a function of its shift in frequency, this scattering process is used spectroscopically to study basic material properties as well as the spectral properties of the excitations present in the material. The intensity of the measured BLS spectrum can be described with the following expression:

$$I_{BLS}(f_2) \propto N(k_{exc}, f_{exc}) \cdot \sigma(k_1, f_1) \tag{5.1}$$

where N is the number of quasiparticles, equivalent to the square of the amplitude of the excitation, and σ

refers to the scattering cross section, often referred to as the spectral sensitivity. A specific implementation of this process, micro-focus Brillouin Light Spectroscopy (μ-BLS), uses a focused laser beam that is scanned along the surface of a thin magnetic film to generate BLS spectra at different positions along the surface, mapping the amplitude of spin waves in real space [5, 19, 152]. In these experiments, the monochromatic light is passed through a linear polarizer and focused onto the sample. The backscattered light is passed through another linear polarizer, rotated 90° with respect to the incident polarization, and then transmitted into a multipass Fabry-Perot interferometer. The interferometer allows for the spectroscopic measurement of light intensity as a function of the shift in frequency that is due to the inelastic scattering. The interferometer used in the experiments described here is sensitive to frequency shifts as low as 230MHz. An example BLS spectrum from spin waves in a 30nm magnetic Yttrium-Iron-Garnet (YIG) film exposed to a 2000 Oe external magnetic field is shown in Fig. 5.1.(d).

Microfocus-BLS has been extremely valuable to the spin wave research community for decades, allowing for spatially resolved measurements of spin wave excitations in nanostructures, in contrast to electronic measurements which often provide information on the entirety of the structure that is electrically excited. However, there is a major limitation to the technique, due to the momentum mismatch between the incident free-space light ($k_1 \sim$ tens of μm^{-1}) and the spectrum of spin wave modes, which extends up to thousands of μm^{-1} [Fig 5.1.(a-b)]. Over the experimentally relevant frequency range from 7 to 9.5 GHz, the number of magnons in an archetypical YIG thin film decays by only around 20%, however, the spectral sensitivity, σ, decays by over 2 orders of magnitude [Fig. 5.1(c)]. Consequently, BLS spectra represent scattering only from spin waves at the bottom of the spectrum. High wavevector, and correspondingly high frequency, spin wave modes are completely inaccessible via traditional micro-focus BLS.

Even with the limitation of being sensitive to only the lowest frequency magnons, μ-BLS has been a valuable tool to studying magnonic systems that are in, or near, thermal equilibrium. However, magnons of all frequencies interact with each other, and consequently, the high frequency magnons that are inaccessible to μ-BLS play a critical role in the process of magnon thermalization [153, 154]. Having the ability to optically detect these high frequency magnons would be beneficial for the study of how magnonic systems evolve in time and ultimately thermalize. Furthermore, there are technological goals of using magnons as information carriers in next-generation computing technology. To create fast magnonic circuits, high frequency magnons must be well understood.

In this work, I demonstrate how sub-diffraction confinement of light by a metallic nano-antenna fabricated on top of a magnetic film can effectively overcome this limitation. I show with experiments, simulations, and calculations how the antenna generates large-momentum components of electric field not present in free-space light, providing information about the high-frequency magnon states that are not accessible to

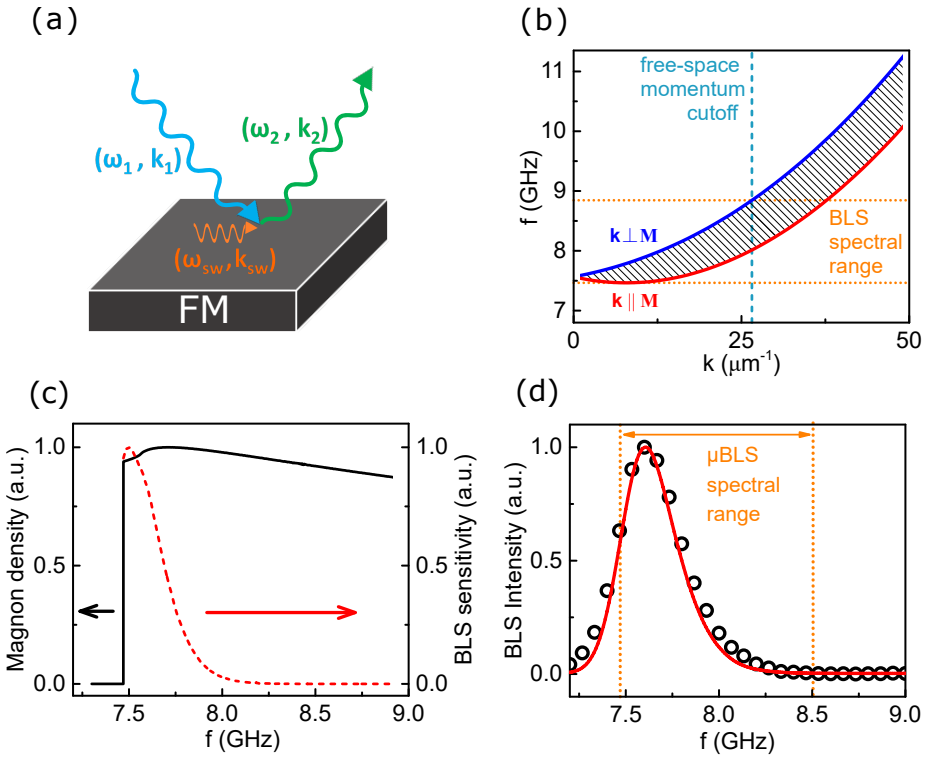

Figure 5.1: Spectroscopic limitations of BLS associated with momentum conservation. **a** In BLS, a photon is absorbed by the material, a quasiparticle is created or annihilated, and a shifted-frequency photon is emitted. This process is constrained by energy and momentum conservation of the involved quasiparticles. **b** Spin-wave manifold for small wavenumbers, calculated using the analytical spin wave theory [1]. The vertical dashed line indicates the largest wavevector accessible to BLS at the probing light wavelength $\lambda = 473$ nm, due to momentum conservation. The horizontal lines show the accessible spectral range. **c** Calculated spectral sensitivity of diffraction-limited μ-BLS (dashed curve) and the spectral density of magnons in YIG(30) (solid curve). **d** Experimental (symbols) and calculated (curve) μ-BLS intensity spectrum. Dashed vertical lines indicate the bottom of the spin-wave spectrum and the high-frequency BLS sensitivity cut-off, with the latter determined by the largest accessible wavevector $k_{max} = NA \cdot 4\pi/\lambda = 22.5$ μm^{-1}, where $NA = 0.85$ is the numerical aperture of the lens used in the experiment, and $\lambda = 473$ nm is the wavelength of light. All the calculations and measurements are for a YIG(30) film at an in-plane field $H = 2$ kOe, and $T = 295$ K

standard μ-BLS. The proposed approach can be easily integrated into other types of inelastic light scattering measurements, such as Raman spectroscopy, and other types of excitations, such as phonons or excitons.

5.2 Mathematical formulation of BLS spectrum

To more rigorous describe the BLS scattering process, and show how the use of a nano-antenna can yield optical access to high frequency spin waves, let us define the spectral intensity of μ-BLS produced by thermally excited spin-wave modes in a thin magnetic film in terms of the following integral:

$$I_{BLS}(f) \propto \int d^2k_{sw} \left| \int d^2k_1 \vec{E}_1(\vec{k}_1)\delta\hat{\epsilon}_{12}(\vec{k}_{sw})\vec{S}(\vec{k}_1 + \vec{k}_{sw})R(f)\right|^2, \tag{5.2}$$

The term $\vec{E}_1(\vec{k}_1)$ from equation 5.2 describes the wavevector dependent incident electric field. For a plane wave of free-space light, the wavevector is uniquely defined by the frequency of the light. This relationship is known as the free-space dispersion: $\omega = c \cdot k$, and gives $k = 13.3\mu m^{-1}$ for the wavelength of light used in our BLS experiments ($\lambda = 473$nm). A focused beam of light is comprised of a continuous range of in-plane photon wavevectors, and can be thought of as a superposition of various plane waves at different angles of incidence meeting together at the focal point of the beam. The more tightly focused the beam is, the larger its distribution of in-plane wavevectors. However, the maximal wavevector of this distribution is still limited by the free space dispersion. In order to create photonic states with wavevectors larger than the that allowed by the free-space dispersion, some form of light-matter interaction must take place. This is where the nano-antenna becomes relevant. By focusing our incident beam of light onto a metallic nano-antenna, the incident photons couple with the conduction electrons in the antenna, creating a local electric field distribution, written in equation 5.2 as $\vec{E_1}(k_1)$. Colloquially, one can think of the momentum from the massive electrons being shared with the incident photons. The electric field in the nanoscale vicinity of the antenna cannot radiate into the far-field, but has momentum components that can, in-principle, be larger than the free-space limit [41].

The term $\delta\hat{\epsilon}_{12}$ from equation 5.2 refers to the off-diagonal components of the dielectric tensor. This tensor describes the electric polarizability of a material: $\vec{P} = \hat{\epsilon} \cdot \vec{E}$, where the diagonal elements describe the effect on the material's polarization due to electric field and the off-diagonal elements describe the effect of magnetic fields, which can come from external magnetic fields, the internal magnetic fields in the case of magnetic materials, or the spin-orbit interaction in the case of non-magnetic materials. The dielectric tensor is often used to describe elastic light scattering from magnetically active materials (such as the Magneto-Optical Kerr effect and the Faraday effect [18]), and with the addition of energy and momentum conservation selection rules, the dielectric tensor can also be used to describe inelastic light scattering (BLS).

The presence of spin waves creates a magnetization oscillating in both time and space, with a dynamic magnetization: $M_x(k_{sw}, f_{sw}) = iM_y(k_{sw}, f_{sw}) = M_0 e^{-i(k_{sw}x - f_{sw}t)}$, where k_{sw} and f_{sw} are the wavevector and frequency of the spin wave respectively, and the square of the amplitude of the dynamic magnetization is equivalent to, in the language of quasiparticles, the number of magnons. Ignoring the effects of elliptical precession on the component of magnetization along the field, $M_z(k_{sw}, f_{sw})$, and terms nonlinear in the dynamic magnetization, we can write the oscillating part of the dielectric tensor as:

$$\delta\epsilon_{ik}(k_{sw}, f_{sw}) = \begin{bmatrix} 0 & 0 & -igM_y(k_{sw}, f_{sw}) \\ 0 & 0 & igM_x(k_{sw}, f_{sw}) \\ igM_y(k_{sw}, f_{sw}) & -igM_x(k_{sw}, f_{sw}) & 0 \end{bmatrix} \tag{5.3}$$

where g is a magneto-optical coefficient. The electric field $E_1(\vec{k}_1)$ is modified by the presence of the spin waves, creating an oscillating electric dipole with polarization given by [155]:

$$\Delta\vec{P}(\vec{k}_2, f_1 + f_{sw}) = \sum_{\vec{k}_1=\vec{k}_2-\vec{k}_{sw}} \Delta\hat{\epsilon}(\vec{k}_{sw}, f_{sw})\vec{E}_1(\vec{k}_1, f_1), \tag{5.4}$$

where summation is performed over the wavevector space in the plane of the magnetic film (xz plane). In the absence of a metallic nanoantenna, the amplitude of the scattered electromagnetic field with the three dimensional wavevector $\vec{k}_2$ characterized by the normal component $k_{2,y} = \sqrt{2\pi/\lambda_2 - k_{2,xz}^2}$ is determined by the dispersion of light, re-radiated into the far-field, is simply given by the expression: $\int_{k_2=0}^{2\pi/\lambda}(\Delta\overrightarrow{P}(k_2)^2 dk_2$.

The term $\vec{S}(\vec{k})$ in equation 5.2 accounts for the effect of the nano-antenna on the radiation pattern of the oscillating electric dipole in the magnetic film, as well as the effects of the detection objective. The relationship between the local field $\vec{E}_{local,xy}$ in the magnetic material and the far-field $\vec{E}_{far-field}$ is determined by the geometry and the dielectric properties of the antenna. It can be described by a tensor $\hat{T}(\vec{k}_{local}, \vec{k}_{far-field})$, such that $\vec{E}_{far-field}(\vec{k}_{far-field}) = \sum_{k_{local}} \hat{T}(\vec{k}_{local}, \vec{k}_{far-field})\vec{P}(\vec{k}_{local})$. Furthermore, our measurement system is only sensitive to one polarization of scattered light, and only detects a finite solid-angle of scattered light. These effects can be described by a vector function $\vec{A}(\vec{k})$, aligned with the detector polarization, such that the amplitude of the E-field at the position of the detector is $E_{detector}(\vec{k}) = \vec{A}(\vec{k}) \cdot \vec{E}_{far-field}(\vec{k})$. Here, we drop the vector notations for the electric field at the location of the detector, because only one direction of polarization contributes to the detected signal. We can now define the detection sensitivity function $\vec{S}(\vec{k})$ shown in equation 5.2

$$\vec{S}_j((\vec{k}_{local}) = \sum_{\vec{k}_{far-field},i} \vec{A}_i(\vec{k}_{far-field})\hat{T}_{ij}(\vec{k}_{local}, \vec{k}_{far-field}), \tag{5.5}$$

we obtain

$$E_{detector} \propto \sum_{\vec{k}_{local}} \vec{S}(k_{local}) \cdot P_{local}(\vec{k}_{local}). \tag{5.6}$$

Because of the reciprocity and the small imaginary component of the electric field in the studied nanostructure, the sensitivity function $\vec{S}(\vec{k})$ can be well-approximated by the electric field distribution in the magnetic film, $\vec{E}_{\vec{k}_{local}}$, created by a beam focused onto the nano-antenna with polarization orthogonal to the polarization of the incident beam. The argument is as follows. The local distribution of electric field produced in the magnetic film by incident light $\vec{E}(\vec{k}_{local})$ describes an electromagnetic mode of the optical system, including the light source, the objective lens, and the studied material, which can be alternatively defined by the distribution of the field of the light source - e.g. an approximately Gaussian diffraction-limited

focused source in the backplane of the objective. By the reciprocity argument, in a time reversed process, if a distribution of polarization $\vec{P}(\vec{k})$ is produced in the magnetic film by the incident field distribution $\vec{E}_1(\vec{k}_1)$ scattered by the spin waves, and this distribution matches $\vec{E}^*_{local}(\vec{k})$, this polarization will result in emission that will form the same focused distribution on the detector positioned in the backplane of the lens. On the other hand, if the distribution $\vec{P}(\vec{k})$ is significantly different from $\vec{E}^*_{local}(\vec{k})$, then the resulting distribution in the backplane of the lens will significantly deviate from a spot focused on the detector, resulting in a significantly decreased detected intensity. Thus, the overlap between the two distributions, characterized by the overlap integral $|\int_k d^2k\vec{P}(\vec{k})\cdot\vec{E}_{local}(\vec{k})|^2$ determines the intensity of the detected signal. Comparing to Eq. (5.2), we see that the detection sensitivity function $\vec{S}(\vec{k})$ can be to a good approximation replaced by $\vec{E}_{local}(\vec{k})$, the distribution of electric field produced in the magnetic film by the diffraction-limited spot with polarization orthogonal to that of incident light.

The final term in equation 5.2 is $R(f)$, which is the spectral breadth of the interferometer. An ideal Fabry-Perot interferometer would have an $R(f) = \delta(f - f_{sw})$, with δ representing the Dirac-Delta function, but in reality, there is a finite frequency window in which light can enter the interferometer to be detected: $R(f) = e^{-[f-f_{sw}]^2/4\Delta f^2}$.

To summarize colloquially, the nano-antenna modifies both the incident electric field, as well as the radiation pattern of the local field excited in the thin magnetic film. The effect of the antenna is to create a momentum components of electric field larger than what is possible in free-space light, and allow for scattering between light and spin waves whose large wavevector make them inaccessible to free-space light.

5.3 Spectral properties of spin waves

The analysis presented later in this text relied on the calculations of the linear spin wave dispersion and other related quantities, such as spectral density of dynamical states and the spectral density of magnons. We have calculated the dispersion using the formula [1, 16]:

$$f_{sw}(k) = \sqrt{(\gamma(B + 4\pi MAk^2) + \gamma 4\pi M(1 - (1 - e^{-kd}/kd)))}\cdot \\ \sqrt{\gamma(B + 4\pi MAk^2) + \gamma 4\pi M(1 - e^{-kd}/kd)sin^2\phi)}, \tag{5.7}$$

where $d = 30$ nm is the magnetic film thickness, $\gamma = 2.8\times10^6$ Hz/Oe is the gyromagnetic ratio, $A = 3\times10^{-12}$ cm^2 is the exchange constant for YIG, k is the wavenumber, ϕ is the angle between the wavevector $\vec{k}$ and the external field, $4\pi M = 1705G$ is the magnetization of the YIG film, and B is the external magnetic field. The magnon occupation function is given by the Bose-Einstein distribution $n(k) = 1/(e^{\hbar 2\pi f(k)/k_bT} + 1)$,

where $f(k)$ is the spin wave dispersion. The calculations of all quantities related to spectral distributions were performed by summing over a dense mesh of k-points, with the corresponding quantities calculated as a function of k, e.g. frequencies according to the dispersion Eq. (5.7). The obtained values were then binned in the frequency domain, with a small width Δf of each bin defining the frequency resolution of the calculation.

5.4 Context of this project: Nanostructure Assisted Optical Techniques

To the best of my knowledge, this project is the first to show how using nanostructures can extend the spectral range of inelastic light scattering. However, the work is qualitatively similar to a series of other projects based around the integration of nanostructures into optical measurement techniques. The most famous of these nanostructure assisted measurement techniques is Surface-Enhanced Raman Spectroscopy (SERS), where scattering from localized electronic excitations is made orders of magnitude stronger via plasmonic excitation. [156–160].

Localized surface plasmon excitation occurs when the resonant frequency of the conduction electrons in a metal coincide with the frequency of incident photons [161]. This resonance condition can be tuned via the dielectric and geometric properties of the metallic element. Dipolar plasmonic resonance occurs when incident light is polarized along the axis of a metallic element with width equal to half of the effective wavelength of the light in the metallic element, which is often less than 500 nm [162]. At resonance, the energy of the incident light is resonantly absorbed into the conduction electrons in the metal, and large, localized electric fields are created near the surface of the metallic element.

In Raman experiments, without plasmonic assistance, the light scattering cross section from a single molecule is far too small to observe experimentally, but when the molecule is placed within a near-field plasmonic hotspot, the concentrated field lead to Raman signals that are orders of magnitude larger, allowing for observable Raman signals from single molecules.

However, the application of Brillouin Light Scattering is fundamentally different than that of Raman scattering. BLS from dispersive excitations (spin waves, phonons, excitons etc.) requires momentum and energy conservation, while Raman scattering from localized electronic excitations only requires energy conservation. In the case of SERS, the strong localized electric fields only act to concentrate the energy from an incident beam into the small region where an electronic excitation occurs. The broad wavevector distribution of these local fields, while integral to my work increasing the spectral range of BLS, is irrelevant to

the application of Raman scattering.

Similar to my work discussed here on BLS, plasmonic Au nanoparticle arrays have been shown to increase the scattering cross section for BLS from resonant acoustic waves excited at the surface of a glass film [163, 164]. However, this work focused on the increased strength of the electric field in the vicinity of the acoustic waves, not the broad wavevector distribution of the localized fields near the plasmonic nanoparticles. The large local electric field does increase the BLS signal from the resonant acoustic waves by around a factor of 5, but because the acoustic waves that are excited are resonant at only a particular frequency and wavevector, the effect of the broad wavevector distribution of localized electric fields is masked. Interestingly, these papers seem to be an attempt to apply the principle of SERS to BLS measurements, calling the technique SE-BLS. Using plasmonic nanoparticles increases the Raman signal by orders of magnitude; however, in these papers, the BLS signal is only weakly enhanced. The difference can be attributed to the fact that Raman scattering occurs from localized electronic excitations, whereas BLS occurs from delocalized, dispersive excitations. The only selection rule for Raman scattering is energy conservation, where both energy and momentum conservation must be satisfied for BLS. A consequence of this is that in the case of SERS all wavevectors of the electric field contribute equally to the same observed signal, whereas in the case of BLS, the wavevector distribution of the electric field determines the scattered light intensity in a more complicated way via equation 5.2. The results from [163, 164] and my results together seem to suggest that the main effect of electric field localization on BLS is an enhanced spectral range of light scattering, not the substantial enhancement in total signal that is seen in the case of SERS.

In addition to Raman scattering and BLS, elastic light scattering has also been enhanced by the use of plasmonic nanostructures [165, 166]. Plasmonic nanostructures have been used to concentrate light into other optically active systems such as quantum dots [167], fluorescent molecules [168, 169], dielectric heating elements [170, 171], solar panels [172], and magneto-optical materials [173–180]

5.5 Characterization of YIG Film

The insulating magnetic film used in my μ-BLS experiments is a 30nm Yttrium Iron Garnet (YIG) film deposited on a Gadolium Gallium Garnet (GGG) substrate. The film was grown by a combination of magnetron sputtering and annealing by Mingzhong Wu's group at Colorado State University [181]. To characterize the magnetic properties of the resulting film, they performed ferromagnetic resonance (FMR) measurements, as shown in Fig. 5.2. FMR occurs when microwaves from a cavity or a microstrip antenna are resonantly absorbed into a magnetic film, generating uniform precession of the spins in the magnet i.e. a spin wave with wavevector $k_{sw} = 0$ [1, 16]. The field at which the resonance occurs is a measure of the

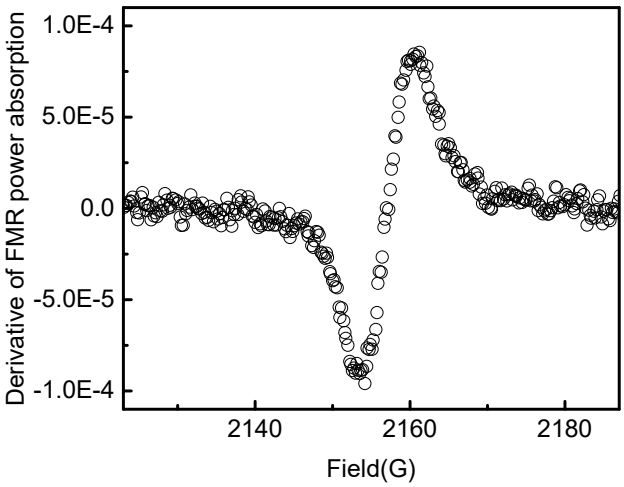

Figure 5.2: The derivative of transmitted power plotted as a function of in-plane magnetic field, measured at 8 GHz, captured from FMR measurement on the 30nm YIG film used in the μ-BLS experiments.

magnetization of the film: $f_{res} = \gamma/2\pi\sqrt{((B_{res}(B_{res} + \mu_0 M))}$, where f_{res} is the resonance frequency, B_{res} is the external field at which the resonance occurs, γ is the gyromagnetic ratio, μ_0 is the permittivity of free space, and M is the magnetization of the film. The FMR measurement indicated that our YIG film has a magnetization $4\pi M = 1705G$.

5.6 Ag and Al Deposition and Characterization

The nano-antennae used in the μ-BLS experiments were designed to be plasmonically resonant, with the goal of maximizing both the local electric field strength and the spatial confinement of the field. The more sharply the electric field is confined, the broader its distribution in wavevector space. Ag and Au are two standard plasmonic materials in the optical frequency range, due to their their large real dielectric permeability, ϵ_{Re}, which characterizes the macroscopic electric dipole strength, and their small imaginary dielectric permeability, ϵ_{Im}, which characterizes dissipation via electron scattering and interband (IB) electronic transitions [161, 182]. However, Au exhibits an IB transition at λ=450nm, quite close to our experimental wavelengths (λ=532,473nm). The IB transition leads to strong damping, and removes Au as a candidate for the material for our antennae. We therefore used Ag and Al as the plasmonic materials for our experimental antennae.

Ag had the continual and unresolved problem of tarnishing over the span of around a week, even with the use of protective capping layers. This limited the amount of data that we could capture on Ag devices. Al proved more practical, because of the 2 nm self-limiting oxide layer that develops at the surface, effectively protecting the sample. Al has been used for some plasmonic applications at UV frequencies, but is not as

commonly used in the plasmonic community. High quality Al is notoriously difficult to grow, due to the strong scattering that occurs at grain boundaries [183]. For other materials, including Ag, the best electronic characteristics are generally attained by creating smooth films with small grains. This can be achieved via physical deposition at cryogenic temperatures, where the low thermal diffusion of the material during deposition prevents the formation of the large grains that develop at thermodynamic equilibrium [184, 185]. We evaporate the Ag and Al films at T=-196°C by placing the substrate in thermal contact with a liquid nitrogen reservoir.

Because of the strong scattering at grain boundaries for Al, we needed to do extra testing to confirm which deposition conditions, and corresponding film characteristics, optimized the plasmonic properties. With the goal of testing the effects of smoothness and grain size, we tested the influence of annealing at 200°C after deposition and several deposition conditions. Room temperature evaporation at moderate deposition rates (∼1-5 Å/s) was our control deposition condition, cryogenic evaporation at fast deposition rates (>10A/s) allowed us to test small grains and smooth films, and room temperature sputtering at low rates (<0.5 Å/s) allowed us to test large grains and rough films. We experimentally tested the quality of our films, shown in Fig. 5.3, by using atomic force microscopy (AFM) to analyze grain size and roughness, as well as optical surface plasmon characterization via the Krestchmann-Raether (K-R) excitation method, where light focused at the Al surface through a high NA, oil-immersion aperture allows for matching between the dispersions of free space light and the SPP mode on the Al/air interface [186]. The reflected image contains a ring of decreased brightness that results from the absorption of the incident light into the SPP mode. The dip in reflection is fit with a Gaussian function, whose full width half maximum is is our quantitative measurement of the quality of the plasmonic resonance, recorded for different deposition conditions in Table 1. Using this methodology, we determined that cryogenic evaporation and later annealing the film at 200°C gave us the highest quality Al.

Deposition Conditions	SPP Resonance Width units: % of diameter of image
Evaporation at ∼1-5 Å/s, T=23°C, Annealed at T=200°C	0.73±0.14
Evaporation at ∼1-5 Å/s, T=23°C, Not Annealed	0.93±0.15
Evaporation at >10A/s, T=-196°C, Annealed at T=200°C	0.56±0.10
Evaporation at >10A/s, T=-196°C, Not Annealed	0.70±0.29
Sputtering at <0.5 Å/s, T=23°C, Annealed at T=200°C	0.70±0.15
Sputtering at <0.5 Å/s, T=23°C, Not Annealed	0.62±0.39

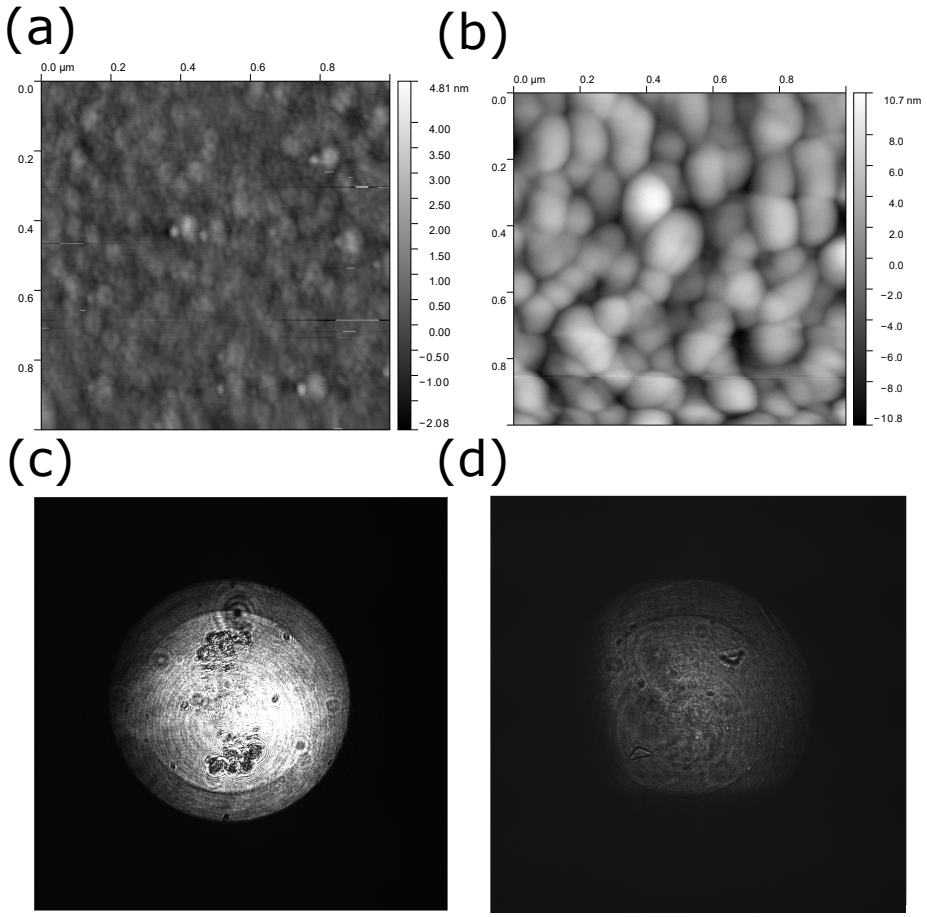

Figure 5.3: AFM topographical scans of 20nm Al films grown by cryogenic evaporation (a) and room temperature sputtering (b). Optical images showing surface plasmon excitation on Al films grown by cryogenic evaporation (c) and room temperature sputtering (d). The spot size is approximately a millimeter, and the dark line corresponds to plasmonic resonance.

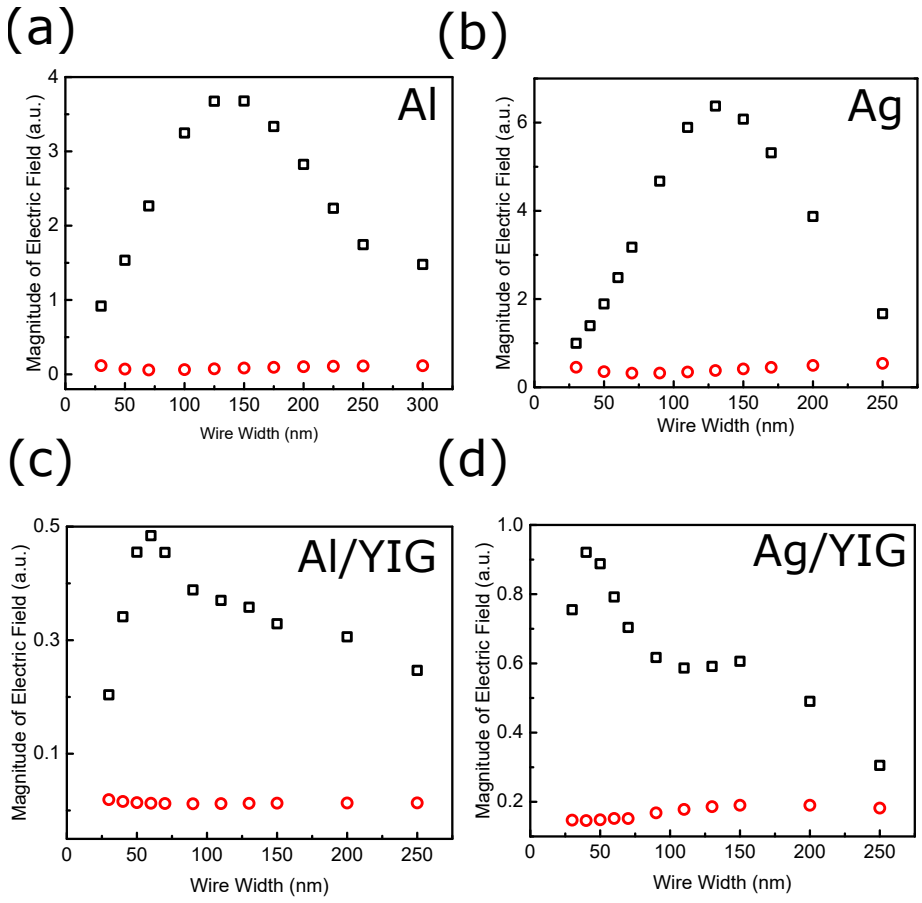

Figure 5.4: Simulated local electric field 6nm under the inner edge of a pair of 30nm thick wires separated by 100nm with varied widths, illuminated by a diffraction limited, focused Gaussian beam. The black squares correspond to incident beam polarized perpendicular to the long axis of the antenna, while the red circles correspond to polarization parallel to the long axis. (a) wires made of Al suspended in air, illuminated at λ=473nm. (b) wires made of Ag suspended in air, illuminated at λ=532nm.(c) wires made of Al in contact with a 30nm YIG film, illuminated at λ=473nm.(d) wires made of Ag in contact with a 30nm YIG film, illuminated at λ=532nm.

5.7 Choosing Antenna Widths: Simulations of Antennae in Contact With YIG

To ascertain the dimensions of antennae that correspond to plasmonic resonance, we performed 2D electromagnetic simulations of the illuminated antenna's near-field using Comsol multiphysics. In Fig. 5.4 (a) and (b), we show simulations of Ag and Al wires, suspended in air. The magnitude of the electric field 6 nm under the inner edge of the antenna is plotted as a function of the wire width, for incident polarization both perpendicular and parallel to the wires. These polarization dependent results suggest that antenna width of 130nm for Ag wires (for incident wavelength λ=532nm) and 140nm (for incident wavelength λ=473nm)

correspond to the dipolar plasmonic resonance.

However, when the antenna are placed in immediate contact with the YIG film, the damping present in YIG redshifts the resonance frequency. If the experimental wavelength is fixed, then the wire width corresponding to resonance at the experimental wavelength will be smaller compared to the wires suspended in air. The simulations of the wires in direct contact with the YIG film [Fig. 5.4 (c) and (d)] show this effect, with the resonant wire width decreasing down to 40nm for Ag (for incident wavelengthλ=532nm) and 60nm for Al (for incident wavelength λ=473nm). The antenna designed for the μ-BLS experiments were triangular pairs of wires separated by 100nm whose width spanned the smallest width we could produce with our e-beam lithography system, up to around 250nm. By using a pair of wires instead of just one, we were able to increase the interaction cross-section of the incident laser with the antenna while still maintaining wire geometries near the plasmonic resonance condition. Both of the Al and the Ag antennae used in the BLS experiments featured narrow tips whose width was expected to be approximately resonant at the experimental wavelength chosen. This design allowed us to scan the laser along the length of the wires, and change the spatial distribution of the incident field, allowing us to study the effect the spatial distribution of the electric field on the BLS spectrum.

5.8 Effect of antenna geometry on local electric field

To clarify the effects of the nano-antenna on the wavevector distribution of the local electric field, let's first consider the effects of a metallic nanoantenna formed by two Al nanowires of width w separated by the gap of width d fabricated on top of the magnetic film [inset in Fig. 5.5a]. In the simplest approximation, the biwire antenna partially blocks the diffraction-limited light spot with the half-width σ incident on the film from above. Consider $w \gg \sigma$, so that only a strip of width d is not optically blocked. The resulting distribution of the momentum of the E-field is described by the Fraunhofer pattern, which exhibits maxima at $k = (2n+1)\pi/d$, with peak amplitude decreasing exponentially but remaining finite at any integer n [187]. Thus, even simple partial light blocking generates momentum components not present in free-space light.

The effects of the antenna are further illustrated by the calculations performed for w = 100 nm and 200 nm, with d = 100 nm [Fig. 5.5a]. The calculated distribution $E(k)$ for w = 100 nm exhibits a sharp peak at k = 27 μm^{-1}, and a broader, less pronounced peak above 50μm^{-1}, both outside the the range accessible to free-space μ-BLS. Meanwhile, the distribution for w = 200 nm exhibits peaks at k = 19 μm^{-1} and k = 38 μm^{-1}. These dependences are qualitatively similar to the Fraunhofer pattern, but the peak positions clearly depend on the antenna width w.

While there is a continuous distribution of wavevector components of electric field created by the antenna,

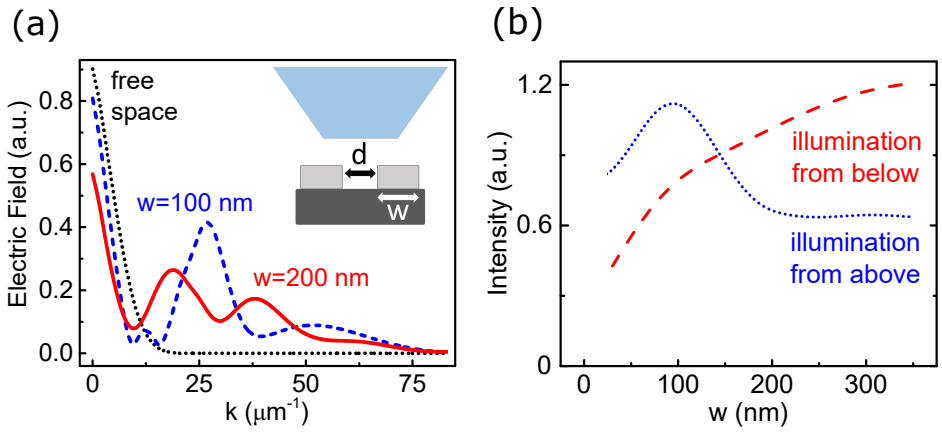

Figure 5.5: Calculated effects of a metallic nanoantenna on the E-field of a diffraction-limited spot. The antenna is formed by two Al(30) nanowires of width w, separated by a gap $d = 100$ nm, on YIG(30) film. The light wavelength is $\lambda = 473$ nm. **a** Fourier spectra of E-field produced by the diffraction-limited Gaussian spot [waist radius $0.61 \cdot \lambda/NA = 339$ nm] focused at the center of the antenna, for the labeled values of w. The distribution for the free-space spot is also shown for comparison. Inset: cross-section schematic of the considered layout, consisting of two wires of width w separated by a gap d, deposited on top of the magnetic film. Light is shown incident from above. **b** Calculated total intensity of E-field vs w, for illumination from above and from the substrate side. All the calculations were performed based on the COMSOL simulations of the spatial electric field distribution [15]

we can qualitatively describe the breadth of wavevectors excited by the antenna by fitting the electric field as a function of in-plane wavevector with the following expression: $E(k > 0) = E_1 e^{-k^2/\sigma_1^2} + E_2 e^{-k/\sigma_2}$, where the first term describes the focused Gaussian beam, with $\sigma_1 = 7\mu m^{-1}$, and the second term describes the wavevector distribution widened by the nanostructure. In Fig. 5.6, we show one of these fittings, as well as the polarization dependent wavevector range, σ_2, for several positions along the antenna. The polarization dependence of the wavevector ranges shown in 5.6(b) is due to plasmonic resonance in the antenna. As described in the section near equation 5.2, the electric field distributions for both incident polarizations contribute to the BLS spectrum.

The effects of the antenna are not limited to light blocking and wavevector enhancement, because the interaction between the electric field of light and electrons in the antenna results in a significant spatial redistribution of the electric field in the vicinity of the antenna. This is illustrated by the dependence of the total intensity of light incident from above on the antenna width [Fig. 5.5b, dotted curve]. The calculated intensity exhibits a peak at $w = d$, due to constructive interference, despite the increasing light blocking for larger w. For illumination from the substrate side, the intensity monotonically increases with increasing w, due to the increased reflection from the antenna [Fig. 5.5b, dashed curve]. These results indicate that a nanoantenna with a judiciously chosen geometry can generate large momentum components of E-field, and simultaneously enhance this field at the location of the magnetic film. According to Eq. 5.2, this should

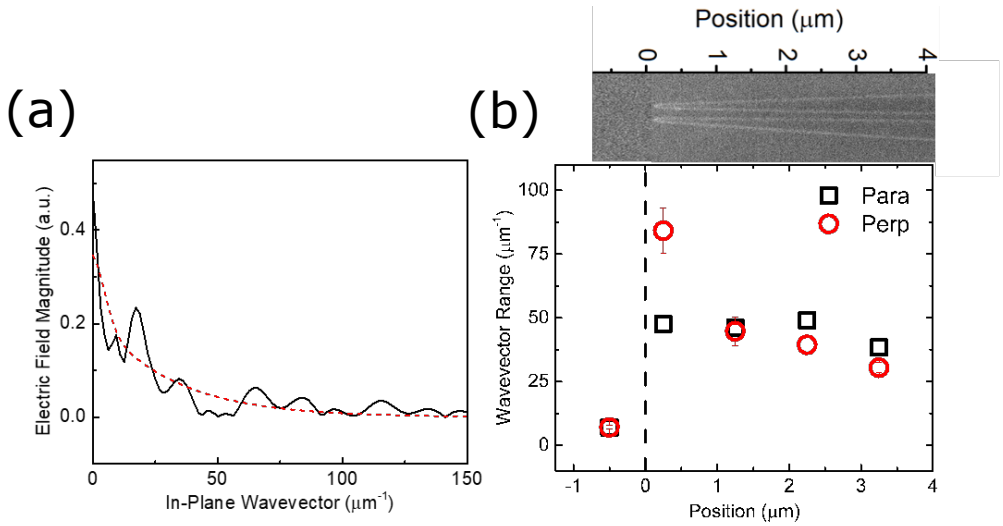

Figure 5.6: We use Comsol multiphysics to simulate the electric field near the illuminated antenna. (a) shows the wavevector distribution of the electric field under the antenna at position 4μm, illuminated by perpendicularly polarized light. (b) shows the characteristic wavevector range for several positions along the antenna, with red circles (black squares) corresponding to illumination by perpendicularly (parallel) polarized light.

increase the BLS intensity, and simultaneously provide optical access to spin waves inaccessible to free-space light.

5.9 Experimental BLS spectra from Al/YIG sample

We have experimentally verified the expected effects of nanoantenna on the μ-BLS spectra, by utilizing an Al(30) biwire with geometry similar to that discussed above. The antenna was fabricated on the YIG(30) film deposited on the GGG substrate [15]. The width w of the wires was gradually varied from 90 nm to 285 nm along the antenna [SEM micrograph in Fig. 5.7a, left], allowing us to probe the dependence of BLS signals on w by scanning the probing spot along the antenna.

Figure 5.7a shows a pseudo-color map of the μ-BLS spectra acquired with the probing spot incident from the free-space side of the structure. The main feature of these data is the abrupt broadening of the spectra, once the spot becomes positioned above the antenna, whose edge is indicated by the dashed line. The intensity decreases with increasing w, as expected due to the partial blocking of the beam by the nanowires. These trends are reflected by the analysis of the total BLS intensity, which exhibits an overall decrease with increasing nanowire width as the probing spot is scanned along the antenna [Figure 5.7b]. However, we note a small increase right near the edge of the antenna, at $w = 100$ nm, consistent with the constructive interference effects discussed above.

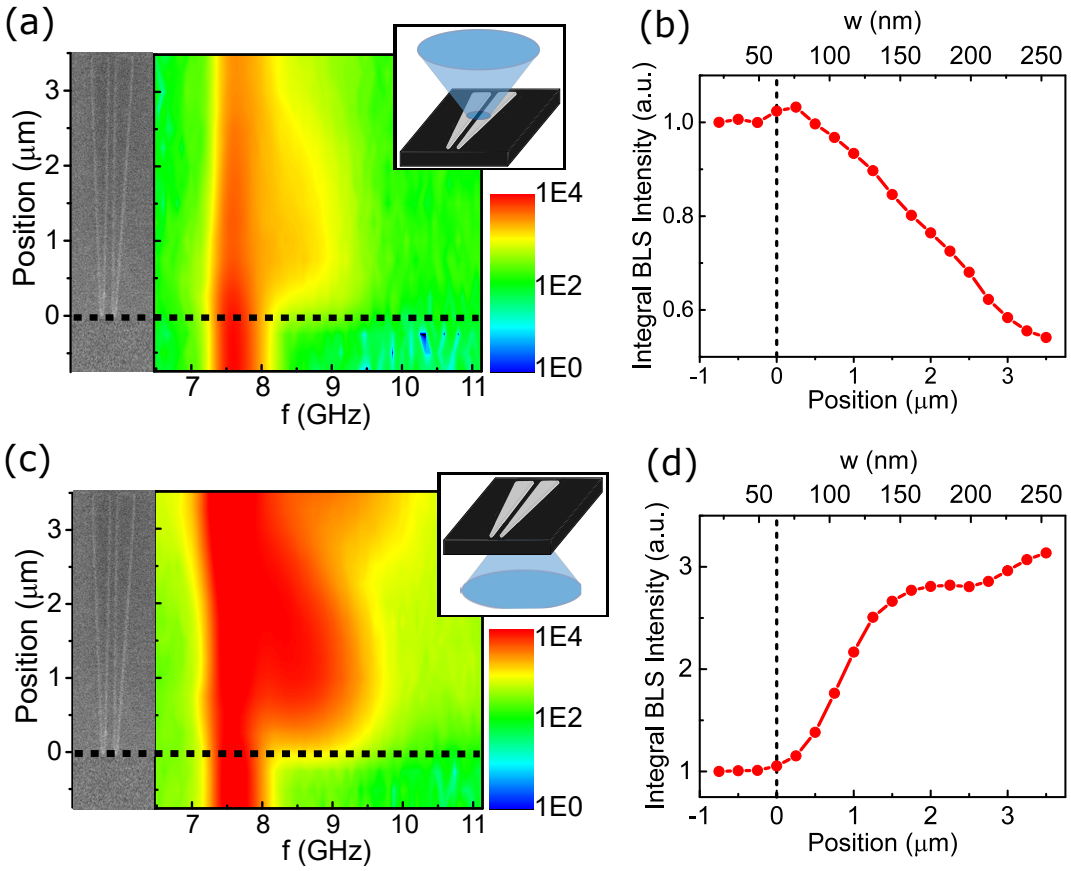

Figure 5.7: Measured effects of the nanowire antenna on the μ-BLS spectra of YIG(30) film. The nanoantenna is formed by two Al(30) wires with width w gradually varied from 90 nm to 285 nm, separated by the gap $d = 120$ nm, as shown in the SEM micrographs on the left. **a**,**c** Pseudo-color maps of the μ-BLS spectra as a function of the position of the probing laser spot along the wire, with the beam incident from above (a) and from the substrate side (c). **b**,**d** Corresponding integral BLS intensity as a function of position along the antenna [bottom scale] and w [top scale]. Insets in a,c, are schematics of the corresponding experimental layouts. In all measurements, the incident beam polarization and the in-plane field $H = 2$ kOe were parallel to the wires

The intensity enhancement and the spectral broadening become significantly more pronounced for illumination from the substrate side, Fig. 5.7c. In addition to the primary peak observed even without antenna, a large secondary peak appears at frequencies around 9 GHz as the probing spot crosses the edge of the antenna. In contrast to illumination from above, the intensity of the primary peak does not decrease with increasing w. Meanwhile, the intensity of the secondary peak first increases, and then starts to decrease, while a third peak emerges in the spectrum at higher frequencies. The additional peaks lie outside the spectral range accessible to free-space μ-BLS [see Fig. 5.1d], demonstrating that the nanowire antenna generates large-momentum components of optical field not present in free-space light.

Figure 5.7c clearly shows that the onset of large additional peaks in the BLS spectrum is not accompanied by the reduction of the BLS intensity for the illumination from the substrate side. On the contrary, the total BLS intensity increases by over a factor of 3 compared to the free-space illumination as the nanowire width w approaches 300 nm, Fig. 5.7d. A pronounced bump in the intensity around $w = 150$ nm is associated entirely with the onset of the secondary peak, demonstrating that the large-momentum components of optical field generated by the antenna are significant.

We now quantitatively analyze the BLS spectra obtained with illumination from the substrate side. These spectra are characterized by three spectral features, labeled "1", "2", and "3" in Fig. 5.8a showing the spectrum for $w = 160$ nm. We obtained a good quantitative fitting of these spectra by a sum of three Gaussian functions, as shown in Fig. 5.8a by a solid curve. The central frequency f_1 of the primary peak is independent of w, while the frequencies of the other peaks are approximately constant or exhibit a modest increase at small w, and then start decreasing at larger w [Fig. 5.8b].

The primary peak is observed even in the absence of antenna. Its frequency is determined by the long-wavelength part of the spectrum, which is not significantly affected by the antenna. The frequencies of the other two peaks are determined by the distribution of spin-wave wavevectors generated by the antenna, expected to be determined by the geometry of the antenna, as discussed below.

We establish the relationship between the observed spectral features and the momentum components of E-field generated by the antenna, by analyzing the spectral positions of the peaks relative to the spin-wave manifold, as shown in [Fig. 5.8c] for $w = 160$ nm. As expected, the frequency f_1 of the first peak corresponds to the bottom of the manifold. Meanwhile, the central frequency $f_2 = 8.3$ GHz of the second peak corresponds to wavevectors around $k_{sw} \approx 25\ \mu\text{m}^{-1}$, and the frequency f_3 of the third peak corresponds to the wavevectors around $k_{sw} \approx 50\ \mu\text{m}^{-1}$, both outside the range accessible to μBLS with free-space light. These results unambiguously demonstrate that the antenna enables one to overcome the fundamental spectroscopic limitations of free-space light scattering.

The efficiency of large momentum generation by the antenna is demonstrated by the analysis of the

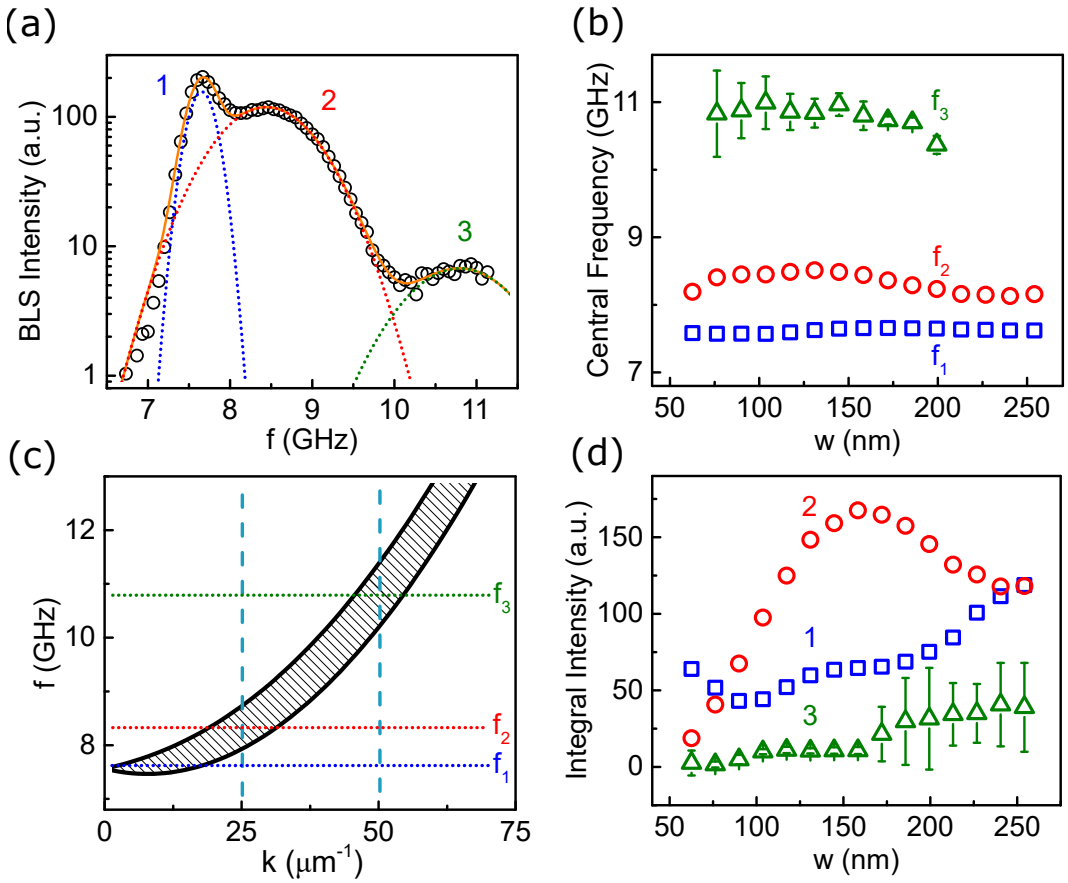

Figure 5.8: Quantitative analysis of the μ-BLS spectra measured with illumination from the substrate side. **a** μ-BLS spectrum for $w = 160$ nm (black circles), and its fitting with the sum of three Gaussian functions $g_i(f) = \frac{I_i}{\sqrt{2\pi}\Delta f_i} e^{-(f-f_i)^2/2\Delta f_i^2}$ (solid curve). The individual Gaussian peaks obtained from the fitting are shown with dotted curves. **b**,**d** Central frequencies f_i (b) and integral intensities I_i (d) of the peaks vs. w. Where omitted, the error bars are smaller than symbols sizes. The peaks are labeled 1,2, and 3, as indicated in panel a. The results for the frequency of peak 3 are omitted for $w > 200$ nm, because of the large fitting uncertainty. **c** Spin wave manifold superimposed with the central frequencies of the Gaussian peaks (horizontal lines), for $w = 160$ nm. Vertical lines are guides for the eye

integral intensity of the peaks, Fig. 5.8d. The intensity of the primary peak initially slightly decreases, but then starts to gradually increase with increasing nanowire width w, as expected from the overall increase of the incident light intensity due to the reflection from the antenna. In contrast, the intensity of the second peak rapidly increases, becoming three times larger than the primary peak near $w = 160$ nm, and then starts to decrease at larger w.

We note that the large intensity of the second peak is concealed in the spectra of Fig. 5.8c by its large width, which is over three times larger than the width of the primary peak. The strong nonmonotonic dependence of the second peak's intensity on w indicates that constructive interference from different regions defined by the antenna plays a significant role in the generation of large momentum of E-field.

5.10 Simulated BLS spectra and Spatial Harmonics Generated by Al Nanoantenna

The mechanisms of the observed efficient large momentum generation by the antenna are elucidated by the calculations of E-field distribution in the magnetic film. Figure 5.9a shows the calculated distribution of the local E-field of incident light in the cross-section of the antenna, for $w = 120$ nm. This distribution is qualitatively distinct from the simple partial blocking by the antenna. The most prominent features are the narrow high-intensity spot in the center of the gap, with two side-lobes localized under the wires characterized by the local polarization opposite to that of the central spot. The phase of E-field reverses again outside the antenna. Thus, the effects of the wires result in a rapid variation of E-field, which reverses its direction four times when crossing from one side of the antenna to the opposite side. The periodicity of the fundamental harmonic of this distribution is approximately $2\pi/(w+d)$, defining the dominant large-momentum component of E-field generated by the antenna.

Figure 5.9b shows the calculated dependence of the μ-BLS spectra on the wire width, obtained using Eq. (5.2) and the simulated E-field distributions such as that shown in Fig. 5.9a. These results capture the salient features of the data: A broad secondary peak that appears around 9 GHz, and a smaller third peak that emerges at larger w. We obtained good fittings of the calculated spectra by the sum of three Gaussian functions. The frequency of the primary peak is independent of w, in agreement with the experimental data [Fig. 5.8b]. The frequencies of the secondary peaks are in overall agreement with the data, but their calculated dependence on w is considerably stronger than observed. While the calculations underestimate the observed dramatic increase of the second peak's intensity, the calculated intensity of the primary peak increases by almost a factor of two when w is increased from 90 nm to 240 nm [Fig. 5.9d], in a remarkable

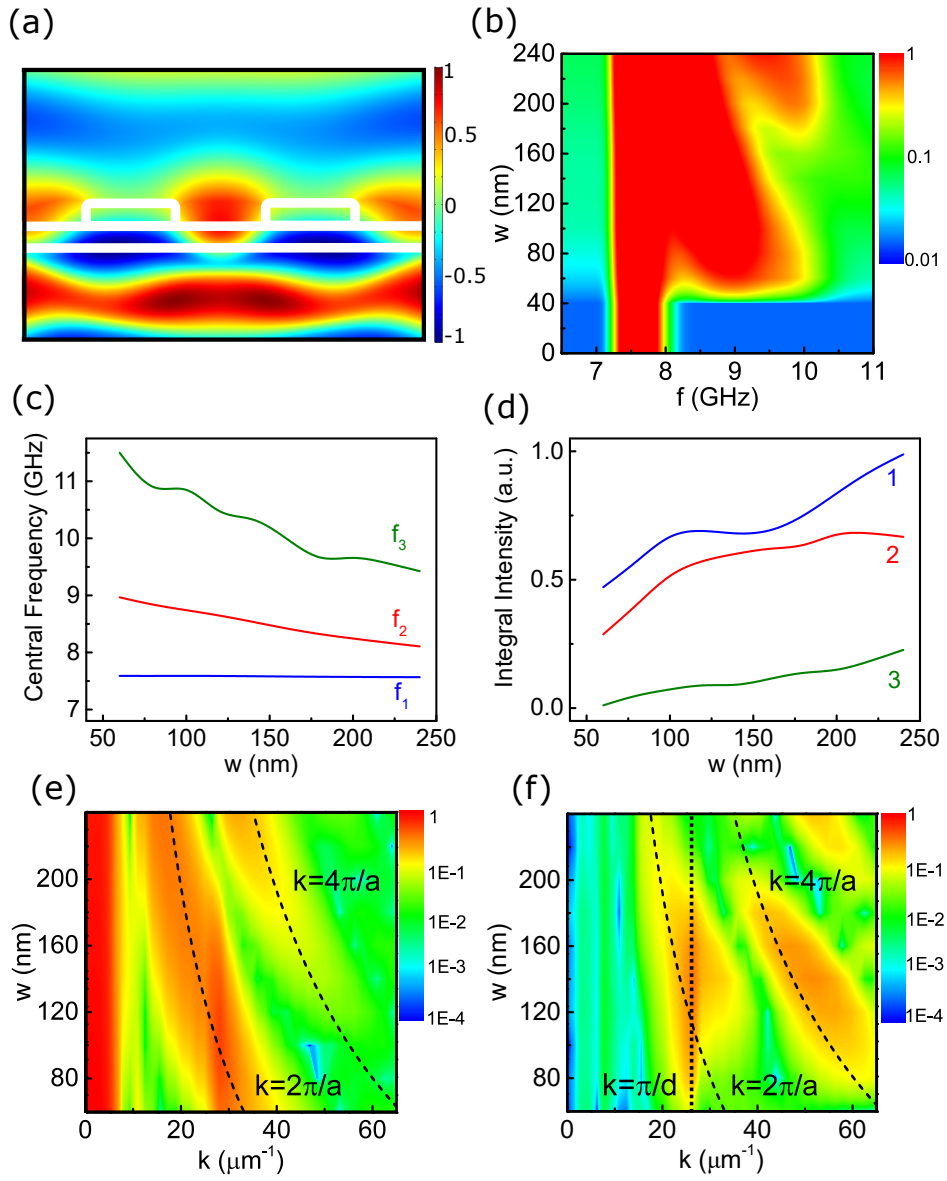

Figure 5.9: Calculated E-field distributions and μ-BLS spectra, for illumination from the substrate. **a** Spatial distribution of the magnitude of the incident optical E-field in the antenna cross-section, for $w = d = 120$ nm, for the polarization along the wires. The boundaries of the antenna and the interfaces of the magnetic film are indicated by white lines. **b** Pseudo-color plot of the calculated μ-BLS spectrum as a function of w, for $d = 120$ nm. **c**,**d** Dependencies on the wire width of the central frequencies (c) and integral intensities (d) of the peaks obtained by fitting the spectra in panel (b) with a sum of three Gaussians. **e** Spatial Fourier spectra of the component of the incident E-field along the wire, for polarization along the wire, vs w. **f** Spatial Fourier spectra of the out-of-plane component of the electric field, for polarization perpendicular to the wires. Dashed curves in (e), (f) show $k = 2\pi/a$ and $4\pi/a$, as labeled, where $a = w + d$. The dotted vertical line in **f** shows $k = \pi/d$

agreement with the data [Fig. 5.8d].

Analysis of the calculated momentum distribution of E-fields provides insight into the effects of the antenna geometry on the generation of large-momentum components. Figure 5.9e shows the momentum distribution of the in-plane component of E-field for polarization parallel to the wires, while Fig. 5.9f shows the momentum distribution of the normal-to-plane component, for polarization perpendicular to the wires. The former describes one of the contributions to the incident field term in Eq. (5.2), while the latter - to the detection sensitivity function. In addition to the primary peak around $k = 0$, the distribution Fig. 5.9e features a prominent secondary peak concentrated around $k = 2\pi/(w + d)$, and a less pronounced peak around $k = 4\pi/(w + d)$, as indicated by the dashed curves. These results are consistent with our qualitative analysis of the spatial distribution in Fig. 5.9a. The distribution in Fig. 5.9f exhibits similar features around $k = 2\pi/(w + d)$ and $4\pi/(w + d)$. In addition, both distributions clearly exhibit enhanced amplitude at $k = \pi/d$, as shown by the dotted vertical line in Fig. 5.9f. Such enhancement is expected from the partial light blocking by a single slit of width d. The resulting Fraunhofer pattern of momentum distribution exhibits maxima around $k = (2n + 1)\pi/d$, with integer n [187], consistent with the observed enhancement. Thus, the secondary spectral peaks observed both in our experiment [see Fig. 5.8] and in calculations can be identified with the interplay between the two contributions discussed above generating momentum components $k = 2\pi/(w + d)$ and $k = \pi/d$, which become mutually enhanced close to $w = d$. This effect can be alternatively described as a geometric enhancement due to the constructive interference of contributions from different regions defined by the antenna.

5.11 Results from Ag/YIG Device: Broad BLS Sensitivity

On the same YIG film, we fabricated another similarly shaped antenna, made of Ag instead of Al. The Ag sample tarnished over the span of a couple of days, limiting the amount of data that we could capture. However, we were able to capture BLS spectra along the antenna for polarization both parallel to and perpendicular to the length of the antenna, under the following experimental conditions: light of a different wavelength than the Al experiment (λ=532nm), with the incident beam focused from below the YIG film, and an external magnetic field of 1000 Oe. The BLS sensitivity (BLS intensity divided by the calculated density of magnons) as a function of frequency is shown in Fig. 5.10 for many positions along the length of the antenna.

The tip of the antenna was expected to be nearly resonant at this experimental wavelength. Furthermore, it featured many small defects that could act to localize the field laterally. The BLS sensitivity observed at the tip of this antenna was quite broad, decreasing by only a factor of approximately 4 from the BLS peak

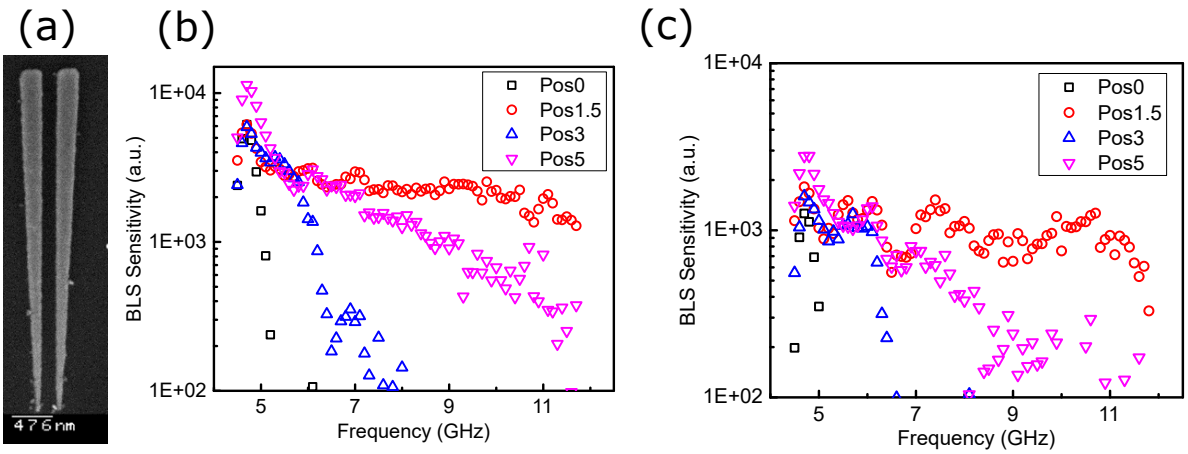

Figure 5.10: (a) SEM micrograph of Ag dimer antenna on YIG film. (b) BLS sensitivity (Intensity divided by density of magnons) plotted as a function of frequency for several positions along the antenna, with incident beam polarized perpendicular to the length of the antenna.(c) same as (b), but with incident beam polarized parallel along the antenna.

at 4.7 GHz up to the highest measured frequency of 11.6 GHz.

Much broader spectral ranges are achieved with this Ag sample compared to the Al/YIG sample, with many positions along the antenna exhibiting spectra that decay by less than an order of magnitude across the measured frequency range. Generally, as the incident beam is moved along the antenna from the tip towards the wide end, the spectral range decreases and then increases again. The broad spectra observed at the wide and narrow ends of the antenna are likely the result of two slightly different mechanisms: the narrow tip of the antenna may exhibit tightly confined electric fields due to plasmonic resonance, while the wide end of the antenna efficiently blocks the incoming beam due to its larger cross section. As with the Al/YIG sample, and as seen in equation 5.2, the BLS spectrum for both incident polarizations is nearly equivalent, highlighting the contributions of the antenna in both the localization of the incident beam and the re-radiation of the photons into the far-field after scattering with spin waves.

5.12 Results from Devices with Conductive Magnetic Film: Permalloy

In contrast to the samples based around the insulating ferromagnetic film, YIG, we also studied plasmonic antenna structures on films of the conductive magnetic alloy, Permalloy (Py). Permalloy is one of the most common conductive magnetic alloys used in modern spintronics and nanomagnetism research, due to its large magnetization and small anisotropy [18]. As compared to the YIG film, the ohmic damping present in Py could decrease localization of the electric field in the near-field vicinity of the antenna. Furthermore,

the conductivity of Py would at least partially short the antennae, so to prevent shorting, we separate the Py from the antenna by a thin insulating barrier of SiO_2.

We fabricated a variety of antenna structures on Py films for BLS experiments. Generally, we observed qualitatively similar results compared to the YIG samples: broad BLS spectra, and for some geometries, prominent Fourier peaks in the BLS sensitivity. We also see a general independence of the measured BLS spectra on the polarization of the incident beam, highlighting the contributions of the antenna in both the localization of the incident beam and the re-radiation of the photons into the far-field after scattering with spin waves.

5.13 Results from Ag/Py Device: Fourier Peaks and Broad BLS Sensitivity

This section describes an Ag dimer antenna structure used to facilitate BLS spectroscopy on spin waves in Py, similar to the YIG devices discussed previously. Instead of the triangular antennae from the YIG devices, we used straight wires, where the wire width was varied from sample to sample to exhibit the effects of the spatial harmonics of the near-field and the plasmonic resonance. The 30nm thick Ag wires, fabricated by a combination of e-beam lithography and cryogenic evaporation, were deposited on top of a thin film multilayer of Py(5)SiO2(4) deposited via magnetron sputtering. The SiO_2 acts as an insulating barrier to prevent shorting, and the finished structures were capped with a protective film of 7nm of Aluminum Oxide via evaporation in a partial oxygen pressure of 1.5mT.

To test which wire widths corresponded to plasmonic resonance, we performed optical transmission spectra on similar test samples. Broad-band white light from an optical fiber is focused onto the antenna and the transmitted light is passed through a linear polarizer and collected into a spectrometer. The dips in intensity of the transmitted light polarized perpendicularly to the length of the wires are expected to correspond with plasmonic absorption. We show in Fig. 5.11 the resulting optical transmission spectra. The results are not as clear as expected, as dips in transmission are seen for both polarizations of incident light. However, the dips are deeper and more obvious for the light polarized perpendicular to the wires, and suggest that wires 100-150nm wide resonantly absorb incident light at the experimental wavelength of λ=532nm.

We also performed Comsol simulations for wires of this configuration, shown in Fig. 5.12. The magnitude of the electric field 6 nm under the inner edge of the antenna is plotted as a function of the wire width, with incident polarization both perpendicular and parallel to the wires, at a fixed incident wavelength λ=532nm.

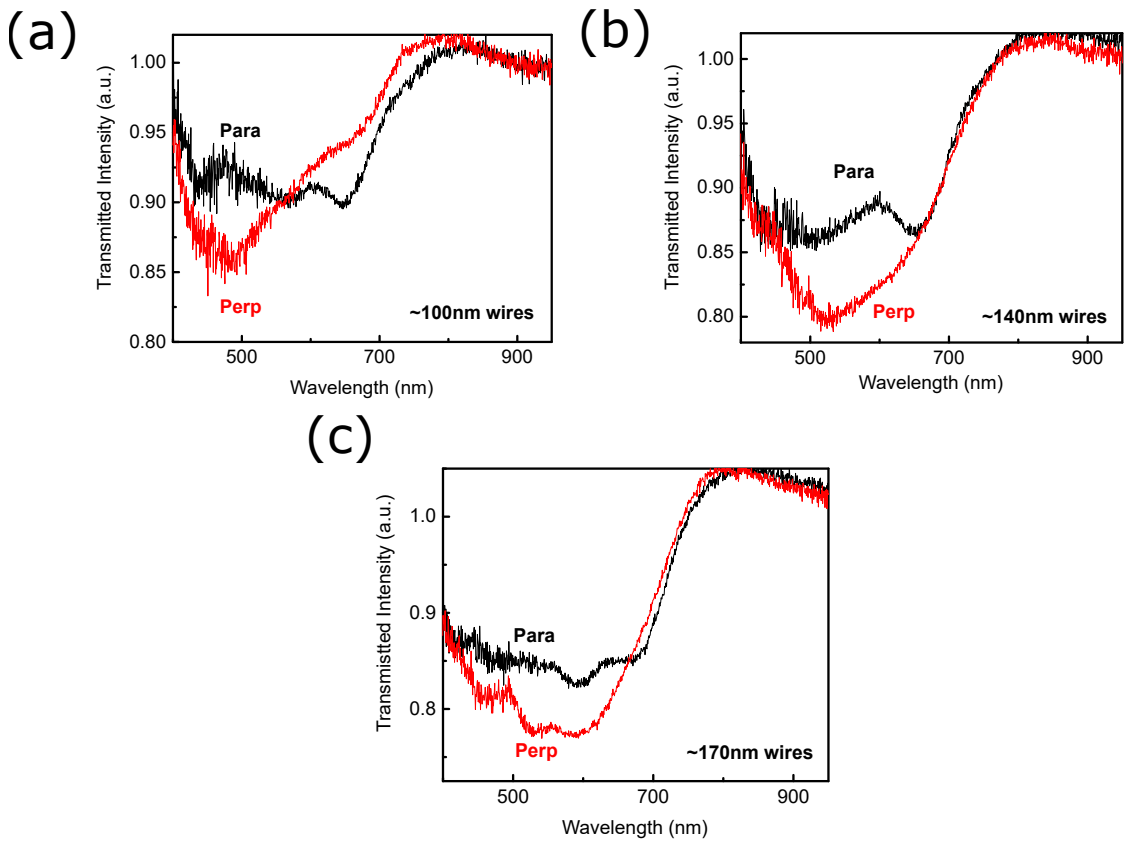

Figure 5.11: Transmitted intensity as a function of wavelength from Ag(30) wires on Py(5)SiO2(4) multilayer with thicknesses in parenthesis, given in nanometers. The widths of the wires are 100nm (a), 140nm (b), and 170nm (c). The red (black) lines correspond to data taken with incident light polarized perpendicular to (parallel along) the length of the wires.

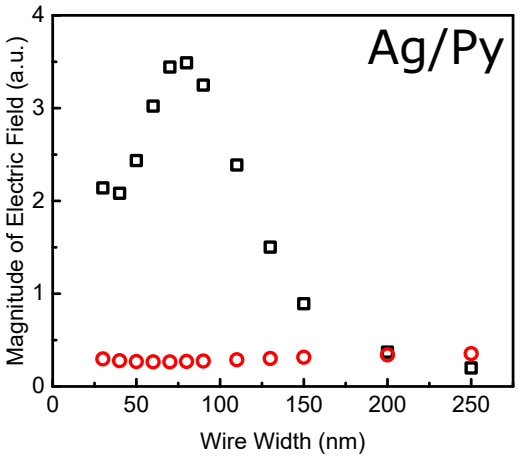

Figure 5.12: Simulated local electric field 6nm under the inner edge of a pair of 30nm thick Ag wires, separated by 100nm for varied widths, illuminated by a diffraction limited, focused gaussian beam at wavelength λ=532nm. The wires are separated from a 5nm thick Py film by 4nm of SiO2. The black squares correspond to incident polarization perpendicular to the length of the wires, while the red circles correspond to polarization parallel to the wires.

These simulations suggest that the resonant wire width at this experimental wavelength is 80nm, smaller than the experimental spectra indicate. The discrepancy between the simulated near field and the experimental far-field transmission is likely due to the enhanced damping that occurs due to the presence of the conductive and lossy Py film. Damping redshifts the spectral location of maximal near-field, but does not affect the spectral location of maximal dissipation [161].

For BLS measurements, we fabricated an array of dimer wire pairs of widths ranging from around 100nm wide to around 200nm wide. The dimer antenna with wire width 100nm, separated by 140nm, was expected to be nearly resonant. Indeed, similar to the YIG structure shown in the main text, this device shows prominent Fourier peaks in the BLS spectra at frequencies corresponding to spin waves with wavevectors : $k = \pi/a$ and $k = 2\pi/a$, where the a is the gap between the wires. The other antennae with different dimensions generally exhibited BLS spectra with enhanced spectral range, independent of the polarization of the incident light, consistent with our analysis.

5.14 Results from Al/Py Device: Fourier Peaks and Broad BLS Sensitivity

We also made similar structures using Al instead of Ag. The simulated local electric field for wires of this configuration for various wire widths are shown in Fig 5.14, and indicate plasmonic resonance for 100nm wide wires. The experimental BLS spectra for a device expected to be resonant and non-resonant are shown

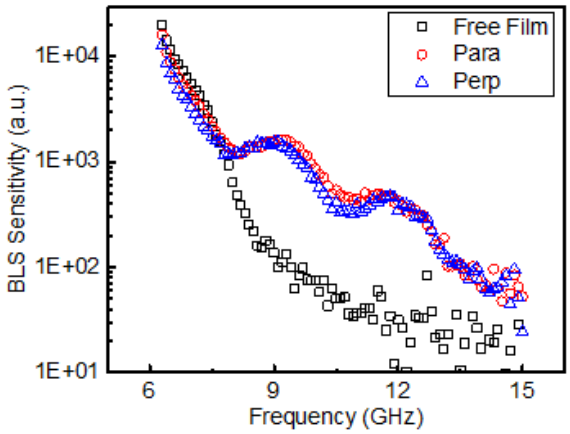

Figure 5.13: BLS sensitivity (intensity divided by density of magnons) plotted as a function of frequency, with incident wavelength λ=532nm. The black squares are from the Py(5) film with no antennae. The data captured when the incident beam is focused onto the 100nm wide Ag dimer antennae is shown by the red circles and blue triangles, corresponding to incident polarization parallel to and perpendicular to the length of the wires respectively.

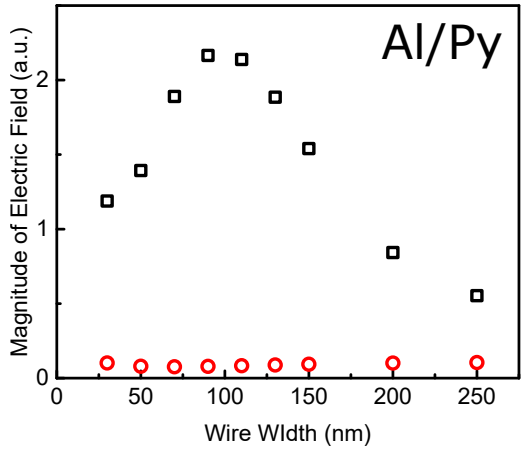

Figure 5.14: (a) Simulated local electric field 6nm under the inner edge of a pair of 30nm thick Al wires, separated by 100nm for varied widths, illuminated by a diffraction limited, focused gaussian beam at wavelength λ=532nm. The wires are separated from a 5nm thick Py film by 4nm of SiO2. The black squares correspond to incident polarization perpendicular to the length of the wires, while the red circles correspond to polarization parallel to the wires. (b) The simulated magnitude of the electric field plotted as a function of in-plane wavevector. The black curve corresponds to wires 50nm wide, while the red curve corresponds to wires 200nm wide.

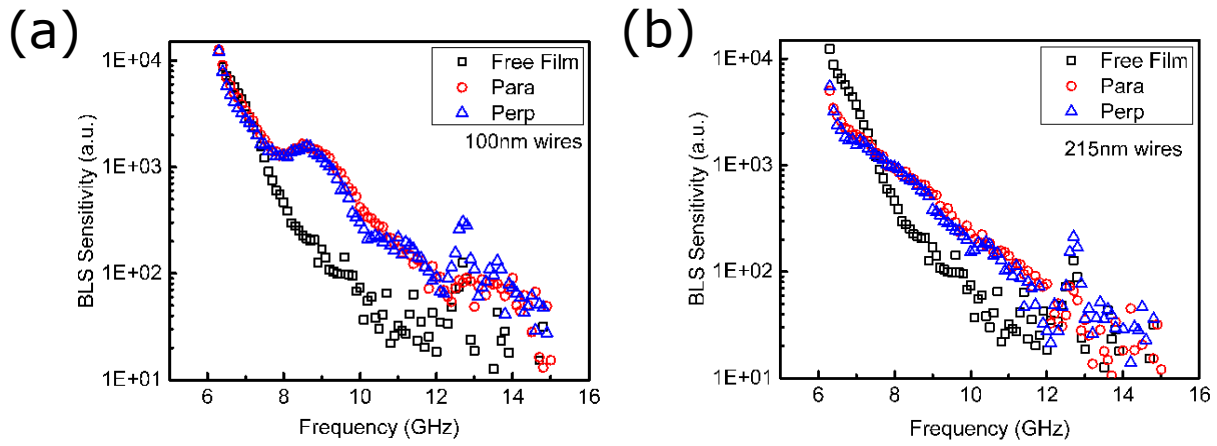

Figure 5.15: BLS sensitivity (intensity divided by density of magnons) plotted as a function of frequency, with incident wavelength λ=532nm. The black squares in both a) and b) are from the Py(5) film with no antennae. The data captured when the incident beam is focused onto the Al dimer antennae is shown by the red circles and blue triangles, corresponding to incident polarization parallel to and perpendicular to the length of the wires respectively. The antenna width in a) is 100nm, expected to be near plasmonic resonance, while the antenna width in b) is 215nm, expected to be far from resonance.

in Fig 5.15, exhibiting broad spectral sensitivity. The resonant device shows Fourier peaks in the sensitivity that are less pronounced as compared to the Ag/Py device. This difference could be due to the weaker absorption into the Al compared to Ag, resulting in weaker geometric shaping of the incident beam.

5.15 Results from Al/Py/Al Device: Broad BLS Sensitivity

To maximize the effects of plasmonic localization in the Py film, we fabricated and studied a Metal/Insulator/Metal (MIM) cavity device. This device is similar to the Al/Py device described previously, with a thin Py film, and an Al nanowire separated by a thin, insulating SiO_2 barrier. These samples feature the addition of an Al layer underneath the Py which acts as an electromagnetic mirror. When plasmons are excited in the wires above, image charges form in the underlying mirror layer, directing the local electric field out of plane and further localizing the plasmonic hotspot [188].

We also experimented with the idea of using a wire grating as an antenna, used in conjunction with the electromagnetic mirror. The grating was designed to act as a metallic photonic cavity (MPC), where the wavelength at which the incident free space light is diffracted along the grating surface (known sometimes as the Rayleigh Anomaly) and the wavelength at which the individual wires exhibit plasmonic resonance coincide. In the limit of a broad, weakly focused beam that exposes many wires in the grating, such a device was expected to lead to sharp peaks in the wavevector distribution of the resulting electric field at $k = 2n\pi//a$. In such a structure the BLS sensitivity could be tuned to particular spin wave modes. This

mode selectivity could be helpful in applications where a specific spin wave mode is being generated, such as caustics, where thermalization of spin waves in special waveguides leads to single modes that propagate in well-defined directions [189].

The idea of using geometry to selectively excite particular wavevectors of some dispersive mode is pervasive in modern physics and engineering. For instance, inter-digital transducers selectively generate specific wavevectors of phonons [190], and grating couplers select particular wavevectors of free-space light to couple to surface plasmons [191–193]. However, to the best of our knowledge this is the first time that a nanostructure has been used to generate particular Fourier harmonics of near-field, high wavevector photons for inelastic light scattering.

Generally, the Rayleigh Anomaly occurs at incident wavelength very near the periodicity of the grating, while the spectral position of the dipolar plasmonic resonance is dependent upon the geometry of the nanowire. When the two modes are spectrally separated, they manifest as a narrow resonance for the Rayleigh Anomaly and a broad resonance for the dipolar wire plasmon mode. When the two modes are brought closer together, the modes hybridize, which is spectrally indicated via an asymmetric, Fano resonance [194, 195]. We see this general behavior, both in our experimental spectra and the simulations. The experimental reflection spectra on wire gratings with periodicity 532nm and various wire widths is shown in Fig. 5.16. These spectra feature the two modes coming together as the wire width is decreased from 150 nm to 50 nm.

The mode hybridization is apparent in our simulations [Figure 5.17], by looking at the magnitude of the local electric field vs the wavelength of the incident beam. When the wires are 100nm wide and the grating periodicity is set to 532nm, the dipolar resonance is redshifted above the simulated wavelength range, and the Rayleigh anomaly is bared visible at $\lambda \sim$532nm [Fig 5.17(a)]. By decreasing the width to 75nm, the two begin to approach each other, and Rayleigh anomaly becomes more clear[Fig 5.17(b)]. When the wire width is set to 50nm, the two modes strongly hybridize, showing two peaks of equal magnitude, approximately 30nm above and below λ=532nm [Fig 5.17(c)]. We interpreted these peaks within the context of mode anti-crossing as an upper and lower branch of the hybridized MPC mode. In Fig 5.17(d), we show the results from a simulation of a single wire of width 50nm, showing the dipolar resonance at λ=550nm and no Rayleigh anomaly.

We performed Fourier transform analysis to the simulated electric field profiles of the grating MIM structures. Fig 5.18 shows the electric field plotted as a function of wavevector for a grating of 50nm wire separately periodically by 532nm. Two different illumination conditions are shown: illumination by a diffraction limited beam, and illumination by a broad beam (beam radius=4μm), while the overall power of the beam is held approximately constant. The broad beam allows for the excitation of the hybridized grating

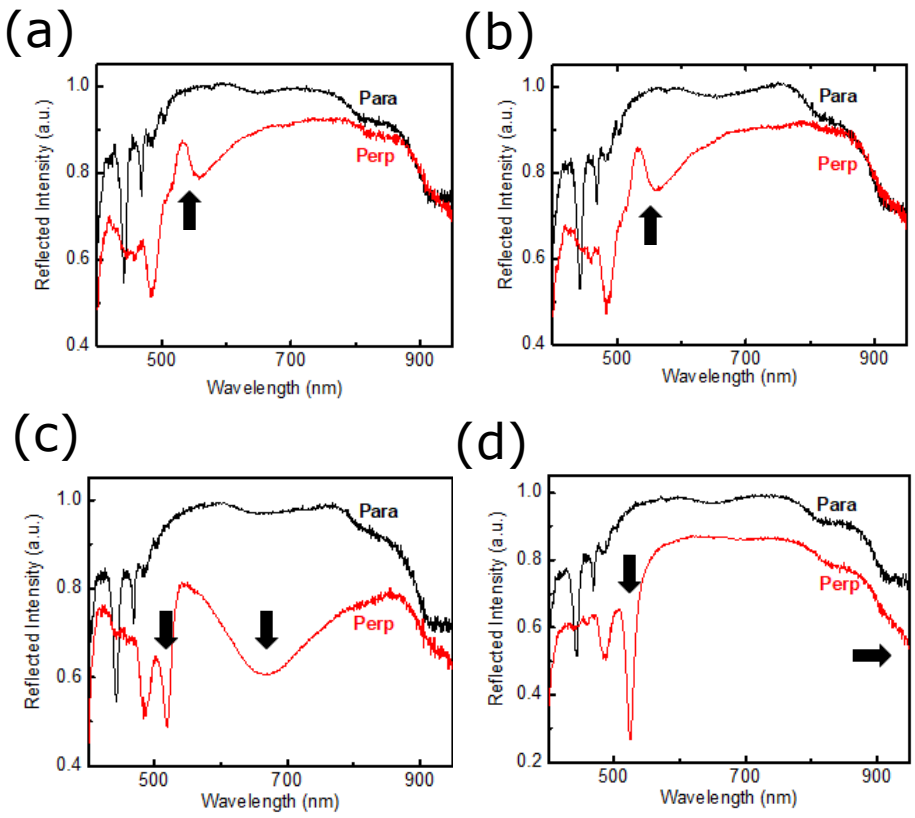

Figure 5.16: Reflected intensity plotted as a function of wavelength from Al/Py/Al wire gratings with light polarized parallel along (black) and perpendicular to (red) the wires. The wire width is varied from: (a) 50nm, (b) 75nm, (c) 100nm, and (d) 150nm. (a) and (b) features a Fano type, asymmetric resonance at around 520nm, indicative of a hybridized near-field photonic mode. As the wires are made larger, the two modes separate, shown in (c) and (d).

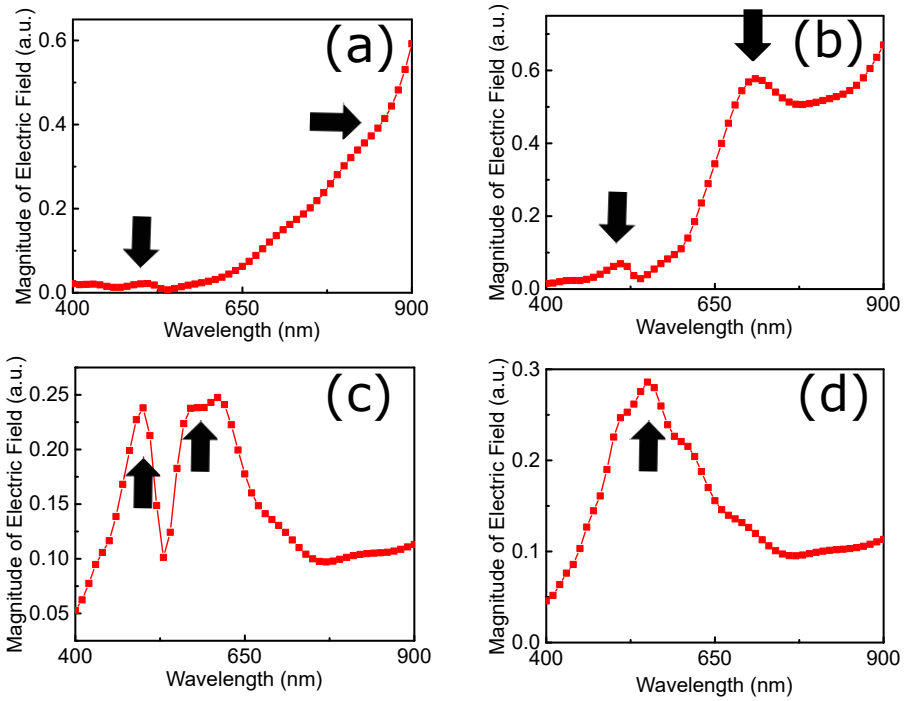

Figure 5.17: Simulated local electric field for All wire gratings of periodicity 532nm, illuminated by a broad beam, plotted as a function of the wavelength of the incident beam. Directly under the grating is a 4nm SiO2 insulating layer, a 5nm Py layer, and a 50nm Al electromagnetic mirror layer. Simulations for wires of width: (a) 100nm (b) 75nm (c) 50nm. (d) features a single wire (no grating) of width 50nm.

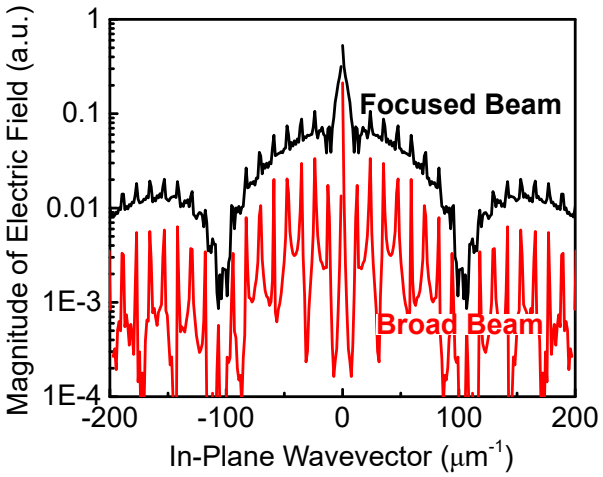

Figure 5.18: Simulated magnitude of electric field plotted as a function of in-plane wavevector for a grating of 50nm wide, 30nm thick Al wires separated periodically by 532nm. Directly underneath the wires are a 4nm SiO2 insulating layer, a 5nm Py magnetic layer, and a 50nm Al electromagnetic mirror layer. The black curve depicts the results from illumination with a beam focused on a single wire, while the red curve depicts the result with the beam widened to expose 9 wires in the grating.

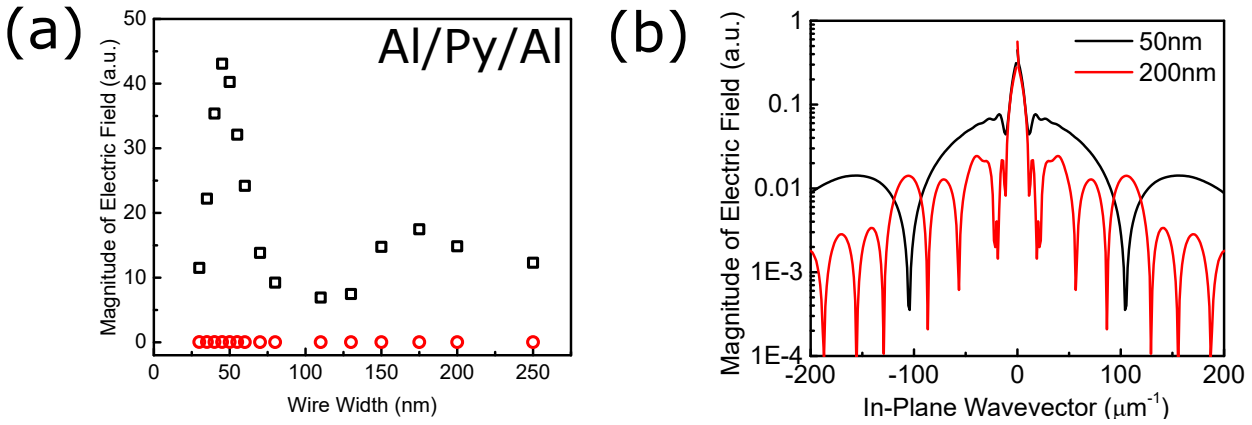

Figure 5.19: Simulated local electric field for a 30nm thick Al wire for varied widths, illuminated by a diffraction limited, focused gaussian beam at wavelength λ=532nm. Directly underneath the wire is a 4nm SiO2 insulating layer, a 5nm Py layer, and a 50nm Al electromagnetic mirror layer. The black squares correspond to incident polarization perpendicular to the length of the wires, while the red circles correspond to polarization parallel to the wires.

mode, where sharp Fourier peaks are present at k=n*2π/a, where a is the periodicity of the grating. The grating when illuminated by a beam focused onto a single wire exhibits weaker Fourier peaks, but a larger overall magnitude of the electric field. Since as a group, our primary goal was to extend the spectral range of BLS, the magnitude of the electric field was considered most important, and I was unable to convince our collaborators that the novelty of the MPC grating structure was worth modifying their BLS equipment to accommodate a broadly focused beam, so we measured the BLS spectra of these devices using a focused beam. Future studies could use similar MPCs to promote scattering from spin waves with with specific wavevectors . These Fourier peaks would only be relevant for scattering from spin waves travelling perpendicular to the length of the wires (the direction of broken symmetry). If an MPC was used to facilitate BLS in a 2D magnetic film, the spectra would contain contributions from spin waves of many different wavevectors and propagation directions. However, if a magnetic nanowire was placed underneath the MPC, perpendicular to the length of the wires, then spin wave confinement would quantize the modes along the lengths of the wires, and BLS experiments would be sensitive to specific wavevectors of spin waves, defined by the Fourier harmonics of the grating.

To fabricate the device for BLS measurements, we use magnetron sputtering to deposit the following multilayer (thicknesses in nm): Al(50)Py(5)SiO2(4), and use e-beam lithography and cryogenic evaporation to deposit onto the multilayer a 30nm thick Al nanowire. The dimensions of the device were chosen based on experimental testing and simulations in Comsol multiphysics. Figure 5.19(a) shows the magnitude of the electric field 6 nm under the inner edge of the 30nm thick Al wire is plotted as a function of the wire width, for incident polarization both perpendicular and parallel to the wires. The simulated local electric

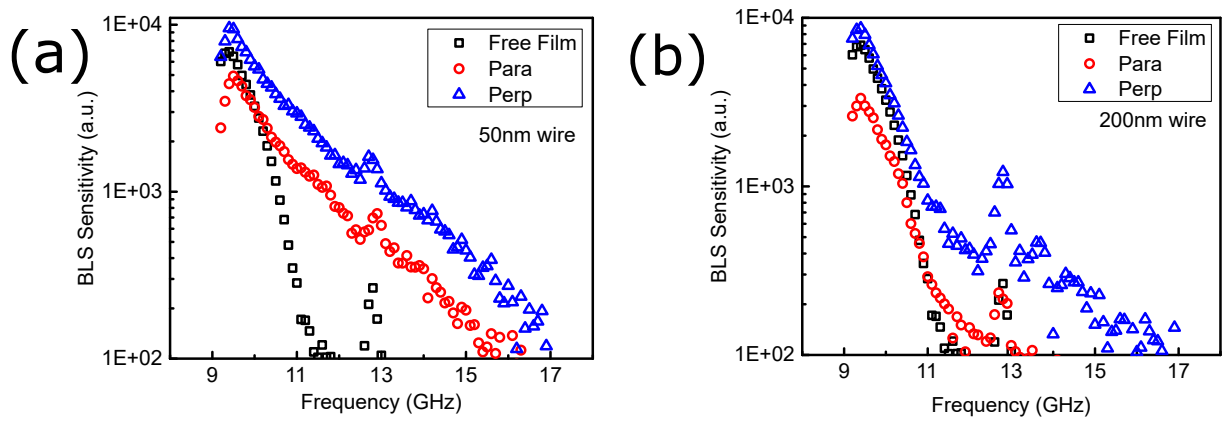

Figure 5.20: BLS sensitivity (intensity divided by density of magnons) plotted as a function of frequency, for a Py(5) film (black squares) and an Al wire, illuminated by a focused beam polarized parrallel (red circles) and perpendicular (blue triangles) to the length of the wire. (a) features a 50nm wide wire, expected to be near the dipolar plasmonic resonance. (b) features a grating with 200nm wide wires, expected to be far from the dipolar plasmonic resonance.

field is significantly larger than the other plasmonic devices studied in this work, and shows a strong dipolar resonance at wire width 50nm, and a small quadrupolar resonance at 175nm. Accordingly, we fabricated a grating of wires 50nm wide, separated by 532nm, expected to be near dipolar plasmonic resonance, and a similar grating with wires 200nm wide, expected to be far from the strong dipolar resonance. The simulated wavevector distribution of the near-field from both devices illuminated by a diffraction limited focused beam is shown in Fig 5.19(b). The experimental BLS spectra obtained from two devices with wires 50nm and 200nm wide respectively are shown in Fig. 5.20. The BLS spectra obtained from the device with the 200nm wide wire, expected to be far from the strong dipolar resonance, was not significantly different than that seen on the free Py film with no wires. However, the BLS spectra of the device with the 50nm wide wire was considerably broader. In particular, the spectral range was enhanced by a factor of 3 as compared to the free Py film, with a weak dependence on polarization.

Chapter 6

Unidirectional Magnetoresistance

6.1 Background and Mechanisms of Unidirectional Magnetoresistance

In this chapter, I will discuss experimental studies that I performed into the contributions of different mechanisms responsible for a newly discovered magneto-electronic effect known as Unidirectional Magnetoresistance (UMR) [196, 197]. This topic is valuable pedagogically for students interested in modern nanomagnetism research, because of the various physical phenomena that come together to create the effect. If one understands the UMR effect, then one understands most of the physics that underpins nanomagnetic research. Furthermore, although the work was never tidied up to a publication quality, in my opinion continuing these experiments is a relatively low hanging fruit that a new student could pick up and potentially turn into publishable results. For now, in no particular order, let us describe the various physical phenomena that make up the UMR effect.

Giant Magnetoresistance (GMR) was described extensively in a previous section; however, we can revisit it briefly here. GMR is observed as a spin polarization dependent resistance in magnetic materials. It occurs due to the different electronic density of states for majority and minority spin electrons, which results in spin-dependent scattering rates for electrons in bulk crystals, as well as at the interfaces between different crystals [76].

Anisotropic Magnetoresistance (AMR) is observed as the dependence of the resistance of a magnetic material on the angle between the current and the magnetization. It is a consequence of the spin-orbit interaction (SOI) allowing scattering between different specific electronic states. The exact mechanisms are different in different materials [18]. For most common magnetic materials, this SOI enabled scattering is

more probable when current is aligned with the magnetization of the material leading to a resistivity that depends on the angle α between the electron spin and its velocity as:

$$\rho(\alpha) = \rho_{\perp} + \Delta\rho \cos^2(\alpha) \tag{6.1}$$

where $\rho_{\perp}$ is the resistivity for current perpendicular to the magnetization [18].

The spin Hall effect (SHE) is also a critical component to the UMR effect. The SHE, explained elsewhere in this thesis, is also a consequence of SOI. When electrical current is driven through a material with SOI, majority and minority spin electrons develop opposing velocities transverse to the current. The result is a net flow of electron spin (spin current), in the directions transverse to the direction of current. There are various specific mechanisms that contribute to this effect: some that are mediated via electron scattering (extrinsic), and others that occur in the absence of electon scatering (intrinsic), either in bulk crystals or at their interfaces [32]. To make things more confusing for new students, the spin Hall effect has different names in different contexts. When it occurs in magnetic materials, it is known as the Anomalous Hall effect (AHE) [18], and when the current is generated by a thermal gradient instead of a voltage it is known as the spin-dependent Seebeck effect [117, 198]. The reverse of these processes can occur when spin currents pass through materials with strong SOI, generating electrical currents. In this reverse case, the effect is known as the Inverse spin Hall effect (ISHE).

The spin Hall effect leads to an accumulation of electrons of specific polarizations at the material interfaces transverse to the direction of current [82]. This spin accumulation can be dissipated either by spin-relaxation (see the chapter 'Spin Relaxation in Pt'), or if the source of SHE is interfaced with another material, the interfacial spin accumulation will leak into the adjacent material, which can be described as a spin current. If this material is magnetically ordered, the injected spin current can either excite magnetization dynamics (spin waves) or flip the magnetization orientation. This process is known as spin transfer, and will be discussed in more detail in a later chapter. With this, we have now introduced all of the topics necessary to explain the UMR effect.

Unidirectional Magnetoresistance is a magneto-electronic effect that has been studied primarily in nanoscale bilayers of nonmagnetic metals that feature a large SOI and ferromagnets (NM/FM), though it has also been seen in FM/semiconductor and FM/topological insulator bilayers [199–202]. It is observed as a small change in the AMR of the bilayer when the magnetization of the FM layer is reversed from along the direction of DC electrical current to opposite the direction of current: $R_{J\|M} \neq R_{J\|-M}$. Figure 6.1 shows perhaps the most straight forward way to observe the effect, the resistance of the bilayer (a 2μm x 1μm Py(5nm)/Pt(3nm) bar) as a function of the angle between the saturating magnetic field and the current. The difference between

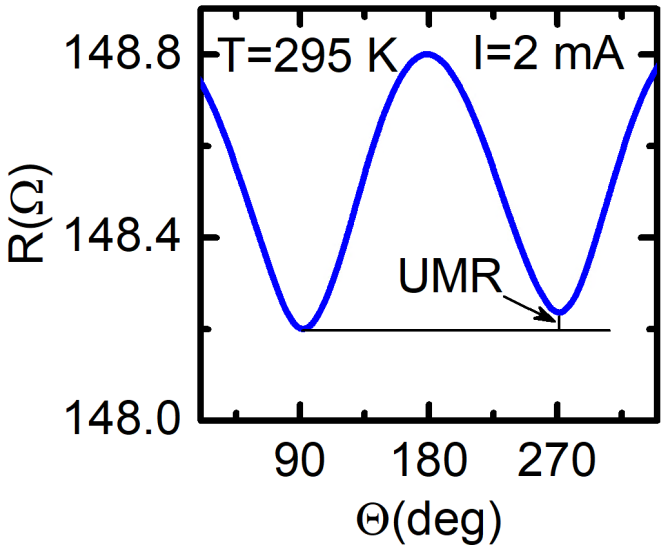

Figure 6.1: Resistance vs angle between the saturation magnetization and current in a 2μm x 1μm Py(5nm)/Pt(3nm) bar. The difference between the resistance at $\Theta = 90°$ and $\Theta = 270°$ is the UMR.

the resistance at $\Theta = 90°$ and $\Theta = 270°$ is the UMR: UMR=R($\Theta = 90°$)-R($\Theta = 270°$).

As seen in equation 6.1, the AMR effect is symmetric with respect to magnetization reversal, so the change in resistance was attributed to effects related to the spin Hall effect occuring in the nonmagnetic metal layer. This small effect (generally less than 20% of the AMR value) wasn't noticed for decades, even though these NM/FM bilayer devices are ubiquitous in nanomagnetism research. There are currently several proposed mechanisms that can contribute to this observed effect, and one mechanism that is sometimes mistakenly referred to as UMR, due to the prevalence of the many, similar acronyms that have been described in this chapter.

The first UMR mechanism that I will discuss has been called by several names, but I will refer to it here as the 'electronic mechanism'. When DC electrical current is driven through the bilayer, the SHE in the Pt layer generates a spin accumulation at both sides of the interface between the Pt and Py. This spin accumulation changes the net polarization of the conduction electrons passing through the Py layer. This may be a bit confusing to people without expertise in magnetism, so to clarify, conduction in ferromagnets is generally not carried only by electrons with spins aligned to the net magnetization. In fact, both majority and minority spin carriers often contribute to electrical current. The spin accumulation from the SHE changes the ratio of majority to minority carriers, the spin polarization. Because of the GMR effect, the resistivity of the Py layer is a function of the spin polarization of the conduction electrons. Since the SHE changes the polarization of the electrons passing through the Py layer, it also changes the resistivity of the Py. Scattering at interfaces is also spin-dependent, and corresponding, there are both bulk and interfacial

contributions to this 'electronic' UMR. The 'electronic' UMR mechanism, stemming from the SHE in Pt, is linear in current to lowest order.

The second UMR mechanism is related to the excitation of spin waves in the Py film, and thus I will refer to it as the 'spin wave' mechanism of UMR. When DC current is driven through the Py/Pt bilayer, the SHE drives spin current into the Py film, either exciting or suppressing spin waves depending on the direction of the current. The spins in the magnetic film precess around the equilibrium magnetization axis. The excitation (suppression) of spin waves increases (decreases) this angle of precession. Because spin waves are quantized excitations of angular momentum, this can equivalently be thought of as an increase or decrease in the number of magnons, the term for the quantized spin wave quasiparticle. Each magnon generated decreases the projection of the magnetization along the equilibrium axis (M_z) by $\mu_B V$, where μ_B is the bohr magneton and V is the volume of the magnetic element. This allows us to write a relationship between the number of magnons and the angle of precession:

$$MV\cos\theta = MV - N\mu_B \tag{6.2}$$

$$N = MV(1-\cos\theta)/\mu_B = 2MV/\mu_B \sin^2(\theta/2) \tag{6.3}$$

Due to anistropic magnetoresistance (AMR), the instantaneous angle between the electron spin and its velocity affects the scattering rate, as seen in equation 6.1. Therefore, the spin current from the SHE and the corresponding excitation of magnons directly affects the resistance measured experimentally. This 'spin wave' UMR mechanism scales linearly with the current that drives the SHE, just like the 'electronic' UMR mechanism.

Another mechanism is sometimes incorrectly described as UMR, but is officially known as spin Hall magnetoresistance (SMR). When spin waves are generated by the spin current driven into the FM, conservation of angular momentum requires spins in the NM to flip. This 'backflow' of spin current, back into the NM generates an electrical current via the inverse spin Hall effect (ISHE), opposite to the direction of the original driving electrical current. This effect is observed as a resistance that is linear in current, but is symmetric with respect to magnetization reversal: $R_{J\|M} \neq R_{J\|-M}$, different from UMR [196].

If you understood all of the acronyms and various magneto-electronic effects described above, then you are well on your way to understand the fundamentals of modern nanomagnetism. In the following section, I will describe the experiments that I performed to distinguish the 'electronic' and 'spin wave' contributions to UMR.

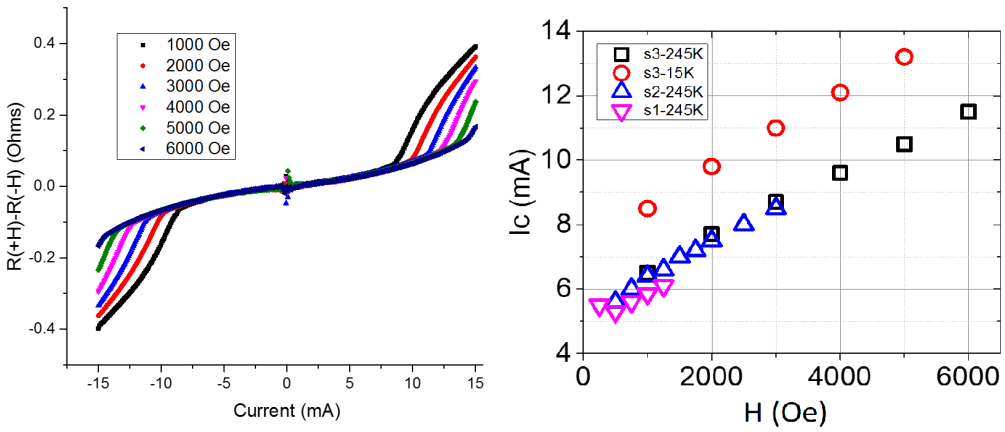

Figure 6.2: (a) UMR plotted from T=15K to T=295K for external fields ranging from 1000-6000 Oe. (b) Critical current as a function of external field, taken from several different samples, at T=15K and T=245K.

6.2 Current dependence of UMR

First, to show simply that the presence of spin waves generated by the spin Hall effect is responsible for at least some component of the observed UMR effect, I've performed measurements of the UMR on a 2μm x 1μm Py(5nm)Pt(3nm) bilayer as a function of the DC electrical current. The measurement was performed by measuring the resistance with the external magnetic field applied along and opposite to the direction of current, with UMR defined as the difference between the two: UMR=R(H)-R(-H). As shown in Figure 6.2(a), this measurement showed a linear increase in UMR with increasing current, up to a critical current above which the UMR increases dramatically. This critical current is a signature of spin waves generated by spin injection, and is a consequence of the generation of spin waves fully compensating the decay of spin waves due to damping. This topic is explained in detail in my thesis chapter on 'Coherent spin waves generated by spin current in the nonlinear regime'. Above this threshold current, increasing current leads to a nonlinearly increasing population of magnons. The fact that this is reflected in the measured UMR is evidence that the UMR effect is dependent on the population of magnons. In figure 6.2(b), the critical current is plotted as a function of the magnitude of the external field for several samples at T=245K and T=15K. As the external field is increased, the population of magnons decreases, resulting in a larger critical current at which damping is fully compensated.

6.3 Effect of Suppressed Magnon Population on UMR

The 'spin wave' contribution to UMR can be distinguished from the 'electronic' contribution by studying how the UMR effect changes when the measured samples are modified to significantly change the amplitude

of spin waves or equivalently the population of magnons. This can be done by either modifying the UMR devices themselves, or by modifying the environmental conditions in which the devices are measured.

To explain, let's first consider what happens when the strength of the external magnetic field, or the temperature are varied. In the absence of currents, spin or electrical, the magnons present in the magnetic system are excited by the thermal energy k_BT. The energy of each magnon is approximately the exchange energy between neighboring spins and the dipolar energy of the spins in the presence of the local magnetic field [1, 16]. By increasing (decreasing) the temperature of the device there is more (less) energy present to be converted into magnons, increasing (decreasing) the number of magnons. Alternatively, by increasing (decreasing) the strength of the magnetic field, the energy per magnon is increased (decreased), resulting in a fewer number of magnons present at a given temperature. This behavior allows us to study the UMR signal as the magnon population is continuously varied via temperature and external magnetic field strength. Specifically, the 'spin wave' mechanism of UMR would have a strong dependence on magnetic field strength, while the 'electronic' mechanism would not. Interestingly, while the spin wave mechanism would be 'frozen out' at low temperatures, the electronic mechanism will generally be larger at low temperatures due to the temperature dependence of the asymmetry of scattering rates between majority and minority electrons [85, 87, 88]. Thus, if the UMR effect disappears at low temperatures, then it can be inferred that the spin wave mechanism dominantly determines the measured UMR.

Now let's consider how one can modify the UMR devices to change the population of magnons. In these experiments I use two methods to achieve this. The first is by modifying the geometry of the electrical current that drives the SHE responsible for the generation and suppression of spin waves. In Fig. 6.3(a), I show a diagram of the Au electrodes placed on top of the UMR bilayer, facilitating an electrical voltage between a region of the UMR bilayer defined by the gap between the electrodes. For this electrode geometry, the electrical current, and resulting spin current, occurs primarily in the region under the gap between the electrodes. This results in spin waves being generated and suppressed in a small region underneath the gap between the electrodes. These spin waves, once generated, are propagate throughout the magnetic film, into regions far away from the electrode gap. Since the UMR measured in this geometry probes only the region between the measurement electrodes, the increased 'radiation damping' that occurs as the gap length is decreased, decreases the density of magnons present in the probed area. With this in mind, I manufactured 2μm x 1μm Py(5nm)Pt(3nm) bilayers with varying gap length between the electrodes. At an external magnetic field of H=1000 Oe, the UMR was measured and normalized by the standard electrical resistance of the device to compensate for path length difference between samples. Since the UMR is primarily linear in current: $UMR(I) = a \cdot I$, the UMR was measured as a function of current and the slope of this dependence was recorded to quantify the UMR while decreasing the influence of measurement noise. This normalized

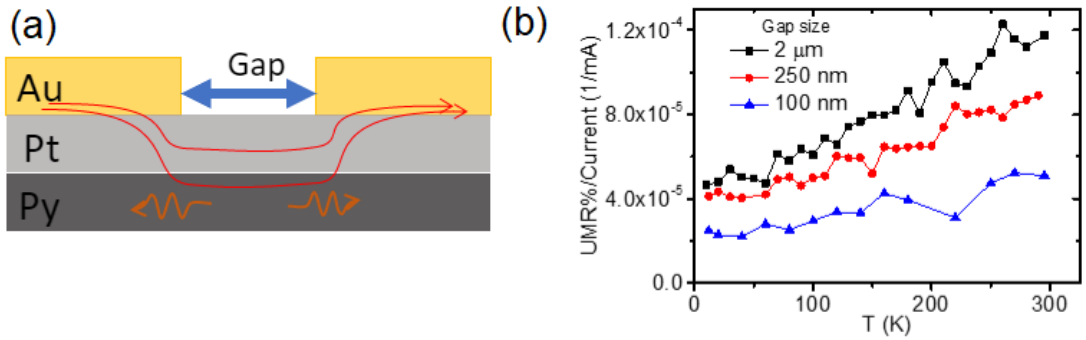

Figure 6.3: (a) schematic depicting the UMR samples: Py(5)Pt(3) bilayers underneath Au electrodes separated by varying gap length. (b) The normalized UMR plotted as a function of temperature for samples of varying gap length.

value of UMR: $UMR/(R*I)$ is plotted in figure 6.3(b) as a function of temperature from T=15K to T=295K, for gap lengths of 2μm, 250nm, and 100nm. This figure shows the normalized UMR decreasing as the gap length is decreased. The effect is larger at high temperatures, consistent with the temperature dependence of magnon population. However, to bring this result to the level necessary for publication, more work would need to be done. The field dependence of the normalized UMR of these samples should be characterized. The density of magnons as a function of gap length should also be calculated or potentially modelled using micromagnetic simulations.

The second way that I've modified the population of magnons is by doping the magnetic material with an impurity with strong spin-orbit interaction (SOI). In this implementation, the number of magnons is reduced not by radiative damping, but by magnetic damping, where the energy and angular momentum of the magnons are lost to the lattice, or directly into the dopants, via SOI. The first of these experiments were performed with PyPt alloys, but large concentrations of Pt were required to significantly increase the magnetic damping, drastically affecting various magnetic properties of the alloy. Alternatively, it has been shown that light doping (1-5%) of Py with rare earth metals can increase the magnetic damping by over 2 orders of magnitude, with only marginal effects on the other magnetic properties of the alloy [203–205]. For Tb, these effects stem from the large SOI, as well as the orientation of the Tb spins anti-parallel to the Py moments. In Fig. 6.4, I show the ferromagnetic resonance (FMR) spectra of a Py(20) film (a) compared to the FMR spectra of a $Py_{98}Tb_2(20)$ film (b). This spectra represents the microwave power at a given frequency transmitted through the film plotted as a function of the external field strength, where the large dip in transmitted power corresponds to the absorption of microwave energy into the lowest energy spin wave modes. The frequency dependence of the linewidth of these curves is related to the magnetic damping in the film: $\Delta H = \Delta H_0 + 2\alpha \cdot f/\gamma$, where ΔH is the linewidth, ΔH_0 is the intercept at zero frequency

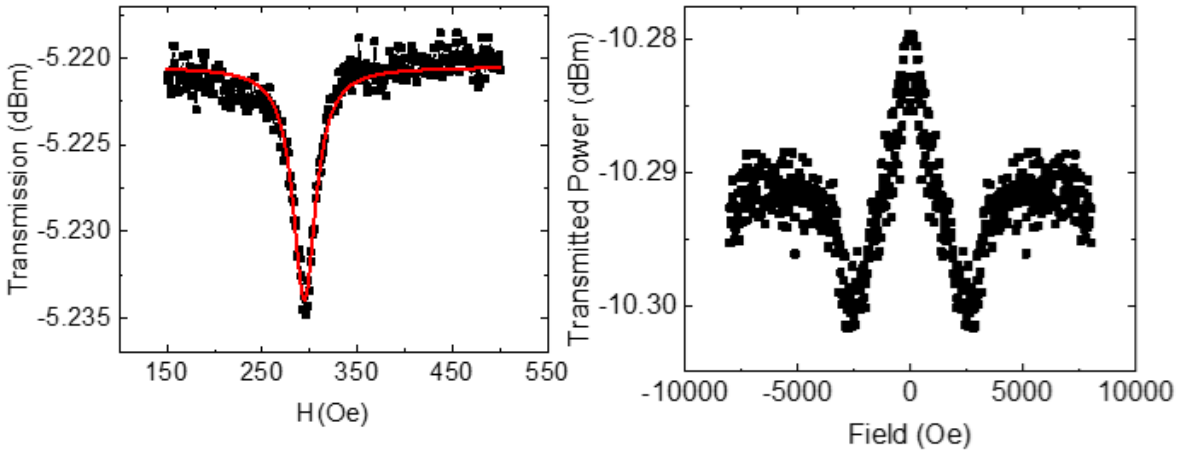

Figure 6.4: (a) Representative FMR spectra of a Py(20) film: transmitted microwave power vs external field, at a driving frequency of 5.6GHz. (b) FMR spectra of a $Py_{98}Tb_2$ film, at a driving frequency of 13 GHz. The frequency of magnetic resonance is related to the external field via the Kittle formula [16]. The FMR dip for this film was so broad that the measurements needed to be performed at a higher frequencies compared to (a) in order to resolve the dip in transmission.

due to inhomogeneous broadening, α is the damping constant, and $\gamma = 28.025$GHz/T is the gyromagnetic ratio [16, 18]. This relationship gives a damping constant $\alpha = 0.0078$ for the Py film and a damping constant of approximately $\alpha = 0.5$ for the $Py_{98}Tb_2$ film, though the unusual shape of the $Py_{98}Tb_2$ spectra makes the analysis less exact.

With this materials science work done, I was able to proceed with UMR measurements of 2μm x 1μm bilayers of $Py_{98}Tb_2$(5nm)Pt(3nm). In Fig. 6.5, I show the UMR of the $Py_{98}Tb_2$ device compared to the pure Py device, measured at 5mA and H=1000 Oe, for T=15-295K. The PyTb device, expected to have a significantly reduced population of magnons, exhibited a UMR approximately 4 times smaller than the pure Py device. These results suggest that the spin wave mechanism of UMR is dominant over the electronic mechanisms, but in order for the work to be publishable, more work would have to be done to characterize the temperature dependent magnon density for the Py and PyTb films, as well as the expected temperature dependence of the electronic UMR mechanism.

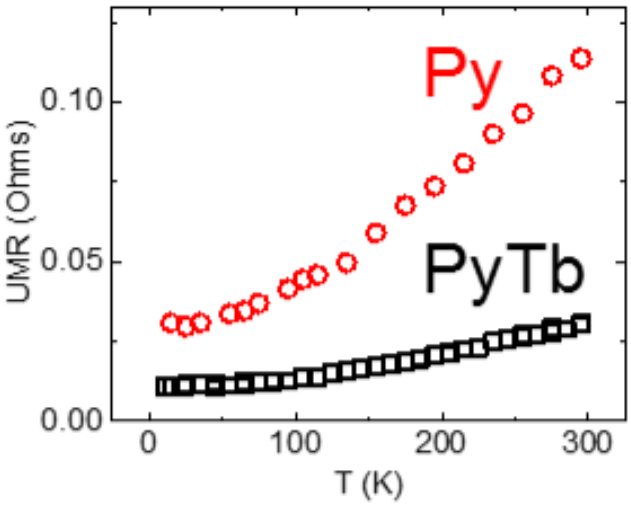

Figure 6.5: UMR as a function of temperature for a Py(20) film compared to a similar device that is doped with 2% Tb.

Chapter 7

Coherent Spin Waves Generated by Spin Current in the Nonlinear Regime

7.1 Background on 'auto-oscillation' spin wave modes

In the course of my PhD, I was also involved in two publications that are a part of an active general area of research: the design of nanostructures that efficiently excite and/or guide propagating spin waves (also known as magnons) [206–211]. The long-term technical goal for these studies is the creation of efficient sources of coherent spin waves and waveguides that allow for their propagation over long distances. These devices are hoped to be used in next generation computing technologies [212–216], and more recently have been used as physical models for neural networks [217–219]. Currently, these devices allow for the transmission of spin waves over relatively short length scales, generally a few μm. A large portion of the research in the field is based around understanding the spectral characteristics and mechanisms of spin wave generation, the nonlinear interactions between magnons, and increasing the length scale over which the spin waves can be coherently transmitted [31, 220]. I will not review the field as a whole, but an interested reader can look at the above citations to learn more.

The two projects in which I was involved were focused on a common nanomagnetic system: the spin Hall/FM bilayer, where current driven through the spin Hall material drives spin current into the FM layer, exciting spin waves. In these projects we studied the generation of magnons by spin currents in the nonlinear regime: i.e. at currents larger than the threshold current above which the excitation of spin waves fully compensates the decay of spin waves due to damping, as shown in figure 7.1. In this high current, 'auto-oscillation', regime, the amplitude of the excited spin wave modes increases dramatically higher as a

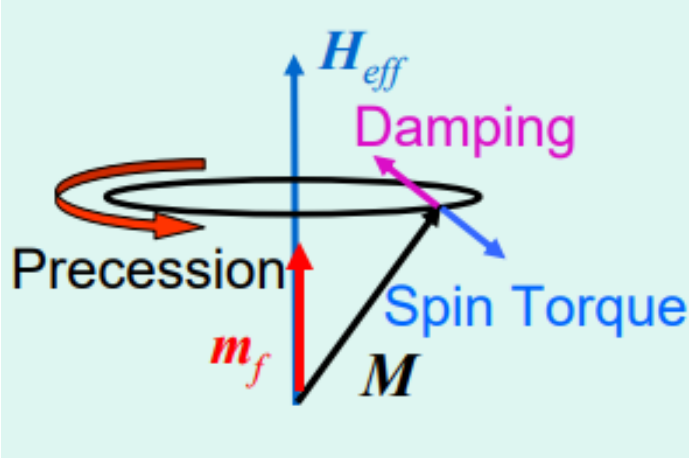

Figure 7.1: Schematic depicting the motion of a spin in a nanomagnetic film in contact with a source of spin current. The spin precesses around the equilibrium magnetization direction, often described as $\hat{M}_z$. Interactions with systems that can take energy and angular momentum out of the spin waves cause damping, a torque that acts on the magnetization to decreasing the amplitude of the spin wave (equivalently decreasing the number of magnons) over time. Spin current driven into the nanomagnetic system excites magnons (or equivalently increases the amplitude of the spin waves). This can be described as an 'anti-damping' torque that is directly opposite to the damping torque. When the spin current reaches a large enough value for the anti-damping torque to completely compensate the damping torque, the nonlinear regime of 'auto-oscillation' is reached, where large populations of coherent magnons are generated. Schematic generated from [17]

function of current compared to the low current regime [17, 32, 221–224]. Colloquially, this means that you 'get more bang for your buck', exciting more spin waves per unit current than in the low current regime. Furthermore, the magnon modes generated in this high current regime are coherent, i.e. in phase with each other.

The difficulty in working in this nonlinear regime is that the physics of how spin waves interact, propagate, and evolve in this regime is not well understood. As the amplitude of spin waves excited increases (i.e. the number of magnons excited increases), the interactions between magnons increase as well, and these self-interactions increasingly dominate the spatial propagation and time evolution of the excited spin wave modes [39, 40, 225, 226].

At low currents, the spin waves that are excited by spin currents are expected to be well-described by linear spin wave theory. These spin wave modes exhibit frequency-wavevector relationships that are well known and can be written in terms of the external magnetic field strength, magnetic properties of the film, and its geometry [1, 16]. Above the threshold current, or critical current, the spectral properties of the magnon populations starts to deviate significantly from what is described by linear spin wave theory.

A common device that allows for efficient generation of spin waves in the nonlinear regime is the spin Hall nano-oscillator (SHNO) [206–208], where two electrodes are placed on top of a bilayer of a spin Hall material and a magnetic film, as shown schematically in figure 7.2. Generally, Pt is used as the source of

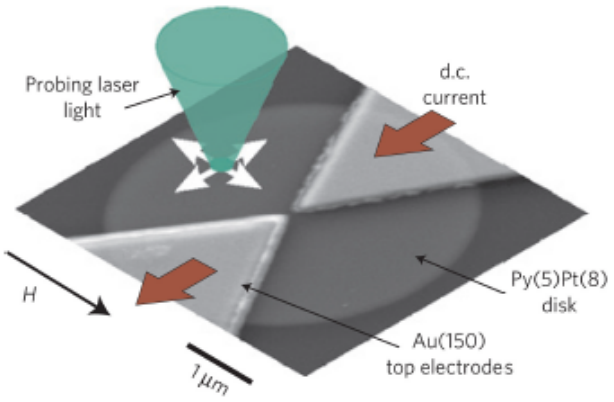

Figure 7.2: Schematic depicting spin Hall nano-oscillator (SHNO), a common nanomagnetic device, generally featuring two electrodes in close proximity to each other, directly in contact with a spin Hall material (e.g. Pt), interfaced with a magnetic material (e.g. Py). The device is capable of generating large populations of coherent magnons, generally confined near the region between the two electrodes.

spin current, and Py is used as the magnetic material. The electrodes are very close (less than 250nm), and come to a point, leading to very large current densities, and correspondingly very large spin current densities generated in the Pt layer, in the vicinity of the gap between the electrodes. This large spin current density allows for the generation of spin waves in the Py film in the nonlinear regime, where the amplitude of spin waves dramatically increases as the driving current is increased. However, the primary spin wave mode that is excited in this geometry is what is known as a spin wave 'bullet' or 'soliton' mode. Although the amplitude of the mode can be driven to be quite large, it cannot propagate.

The existence of this 'bullet' mode was predicted in [227] in 2005, due to the similarities between the nonlinear Schrodinger equation and the equation that describes the time evolution of the spin wave amplitude when accounting for nonlinear interactions between magnons. The nonlinear Schrodinger equation describes slowly evolving quasi-monochromatic wave packets that interact nonlinearly in a dispersive media [228]. One of the solutions to this equation is what is known as a 'soliton' or 'bullet' mode, characterized by an imaginary wavevector (i.e. evanescently decaying away from the region of excitation).

While this bullet mode is interesting on its own, the fact that it cannot propagate makes it incompatible with the technical goal of launching coherent, long range spin waves. In this following, I describe work in which I was involved characterizing spin waves excited in this nonlinear regime. One of the projects is more fundamental, characterizing the time evolution and spectral properties of these spin wave modes [40]. The other project is a technical achievement, showing a device that simultaneously excites spin waves in the nonlinear regime, and launches them into a spin waveguide allowing them to propagate [39].

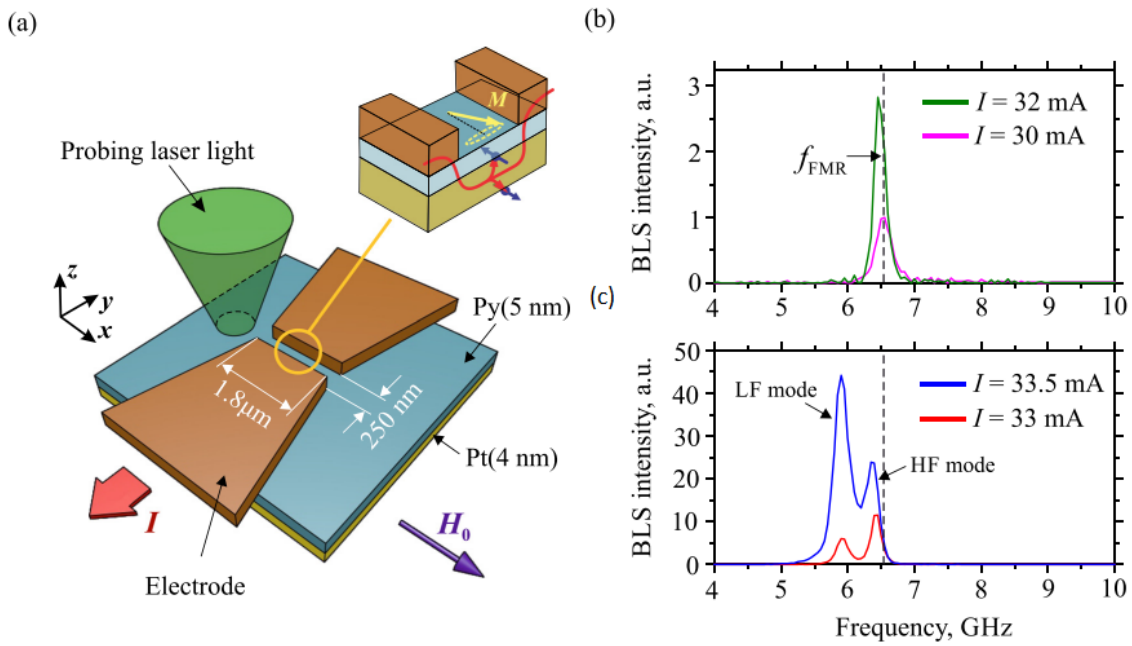

Figure 7.3: (a) Schematic of nano-gap spin Hall nano-oscillator (SHNO). The gap between the electrodes is 250nm by 1.8μm. The Py(5)Pt(4) bilayer is directly underneath the electrodes. (b-c) The BLS intensity vs frequency for DC currents under (b) and over (c) the critical current threshold. Under the critical current, only the linear FMR mode is excited. As the critical current is approached, the amplitude of the FMR mode is increased. Above the critical current, two spectrally distinct modes are excited.

7.2 Controllable excitation of quasi-linear and bullet modes in a spin-Hall nano-oscillator

As described in the previous section, the SHNO is a well-known device used to excited spin waves in the nonlinear, 'auto-oscillation', regime [figure 7.2]. The large spin current density in the region near the gap between the electrodes efficiently excites a spin wave 'bullet' mode localized to the region near the gap. In the limit of low DC current densities, the spin waves that are excited by spin current can propagate over microscopic distances and are well described by the standard, 'linear', spin wave theories [1], but are generally of much lower amplitude than the bullet mode. In this project, we use the standard and effective magneto-optical technique μ-BLS to characterize a device in which the geometry of the electrodes creates a spin current density in between these two regimes, with a spatial profile that allows for the generation of both the bullet mode and the linear, propagating spin wave modes. These measurements allow us to describe the spectral properties of these modes, their behavior as a function of the driving DC current, and their time evolution.

A schematic of this device is shown in Figure 7.3(a), where the electrodes on top of the Py(5nm)Pt(4nm)

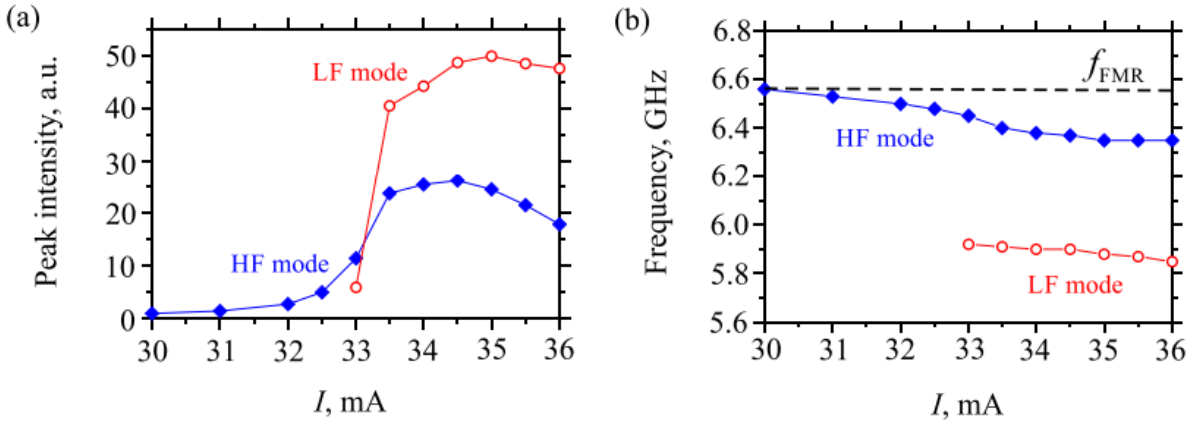

Figure 7.4: (a) The DC current dependence of the peak intensity of the two modes excited above the critical current threshold. (b) The DC current dependence of the central frequency of the two spin wave modes.The high frequency 'quasi-linear' mode continuously evolves from the linear FMR mode as the current is increased. The low frequency 'bullet' mode abruptly appears at currents above the critical current.

film are trapezoidal in shape, with the inner edges being 1.8μm long, separated by a gap of 250nm. In μ-BLS, the reflected intensity of the probing laser spot characterizes the magnon population (equivalently the spin wave amplitude) as a function of the spin wave frequency. For more information on this optical technique, visit the chapter on BLS from optically inaccesible spin waves. The BLS spectra shown in figure 7.3(b) and (c) show respectively the spectral distribution of spin wave generated below and above the critical current threshold. Below the critical current threshold, the large peak in intensity corresponds with ferromagnetic resonance (FMR), representing the lowest energy, k=0 mode from the linear spin wave dispersion, i.e. uniform precession of the magnetic moments in the Py film. Above the critical current, in the nonlinear regime, two spectrally distinct modes are observed, one clearly below the FMR frequency, and one near the FMR frequency. This low-frequency mode is the spin wave bullet mode, while the higher frequency mode is referred to as the 'quasi-linear' mode, due to its spectral proximity to the FMR frequency.

The characteristics of these modes is elucidated further by looking at the spectral properties of the two modes as a function of the driving DC current, shown in figure 7.4(a). As the DC current is increased near the threshold current, the amplitude of the quasi-linear mode gradually increases, whereas the bullet mode rapidly appears and increases in amplitude above the threshold current. Figure 7.4(b) shows the current dependence of the central frequencies of these two peaks. From this plot it is clear to see that as the current is increased the 'linear' FMR mode shifts to lower frequencies, becoming the 'quasi-linear' mode. This may seem like a pedantic difference, but the difference in terminology points to the fact that the FMR frequency is robustly and simply determined by the well-known linear spin wave theory, whereas the injection of spin current above the critical current threshold significantly modifies the spin wave dispersion. In figure 7.4(b),

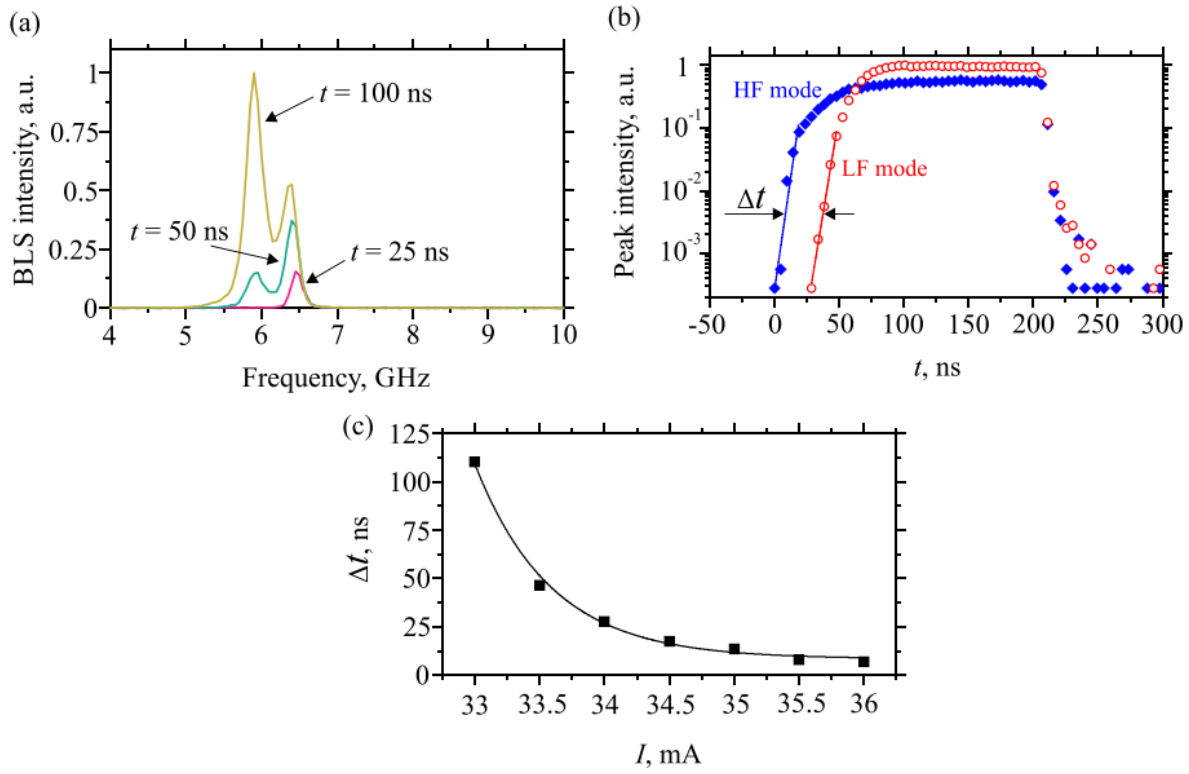

Figure 7.5: (a) BLS spectra measured at I_DC=34mA, at different time delays with respect to the start of the driving current pulse, as labeled. (b) Time evolution of the two nonlinear modes, at I_{DC}=34mA. Curves show the exponential fits for the leading edge of the time dependence of dynamic magnetization. (c) Current dependence of the delay time Δt. The curve is a guide to the eye. The data were obtained at H=500 Oe.

it is also clear that the bullet mode is spectrally separate from the linear and quasi-linear modes.

The qualitative differences between the two modes are further elucidated by the time-domain evolution of the current induced dynamics. Figure 7.5(a) shows the BLS spectra corresponding to different delay times t relative to the start of the pulse of the driving current I = 34 mA. At t = 25 ns, only the high frequency, quasi-linear mode is present in the spectrum. The low frequency bullet mode emerges at longer delays, suggesting that the mechanism responsible for the formation of this mode is substantially different. This is further illustrated by Fig. 7.5(b), which shows the time dependences of the intensities of the two modes on the log-linear scale. The intensities of both modes increase with time exponentially, at a similar rate. However, the HF mode emerges from the linear spin wave fluctuation background starting at t = 0, immediately after the onset of the current pulse, while the LF mode starts to emerge with a significant delay Δt of about 27 ns. The observation that the LF mode requires a certain time for its formation indicates that the nonlinear self-localization is facilitated by the initial increase in the dynamical amplitude of the quasi-linear mode. Figure 7.5(c) shows the current dependence of the time Δt required for the bullet formation. As the driving current I_{DC} is increased from 33mA to 36mA, the value of Δt monotonically decreases from

100 ns to about 10 ns.

7.3 Nanomagnetic device capable of nonlinear generation and propagation of coherent spin wave modes

In this section, we show a similar FM/NM bilayer device in which the spin Hall effect generates the nonlinear, coherent 'auto-oscillation' modes described above, with the additional ability to launch them into a waveguide in which they can propagate. These capabilities are a result of several physical effects related to the carefully chosen geometry of the device. The device consists of a 5μm long, 180nm wide, Pt(4nm)Py(15nm) wire. Near the center of this wire, there is a region 200nm long in which the Py layer has been ion-milled down to a thickness of only 5nm, as shown schematically and with SEM micrographs in figure 7.6. It is the interaction between the coherent spin waves generated in this 'nano-notch' region and the extended magnetic wire that allow for the simultaneous generation and propagation of the coherent 'auto-oscillation' spin wave modes.

First, let's discuss the relevant spin wave physics in the 'nano-notch' region. The thinner magnetic layer in this region of the device exhibits two primary effects. One is that for this thinner geometry, more magnons can be generated for a given magnitude of spin current. Essentially, by decreasing the thickness of the magnetic element, but keeping the thickness of the spin Hall material the same, the total number of spins in the magnetic layer is decreased, but the spin accumulation from the spin Hall effect is kept constant. This leads to a larger effect from the spin current, and allows for considerably lower critical currents than what was seen in the devices described in the previous section.

The second effect is that as the magnetic film is made smaller, the characteristic frequencies of the spin wave modes in the film are pushed higher [1]. In the previous section, we saw that the nonlinear 'auto-oscillation' modes appear at frequencies near and below the lowest frequencies present in the linear spin wave spectrum [40], as seen in figure 7.4. Spin waves from the linear spin wave spectrum at these low frequencies are characterized by small wavevectors and group velocities, meaning that they do not travel very far before dissipating. Once excited, the nonlinear modes can couple to the modes from the linear spectrum, following energy and momentum conservation. However, any spin waves from the linear spin wave spectrum that are excited via coupling to the nonlinear modes will not propagate far, because of their low wavevectors and group velocities.

This limitation is overcome by using the 'nano-notch' geometry. Generally, as magnetic films are made thinner, the characteristic frequencies of the spin wave modes in the films are pushed higher. In this device, the nonlinear modes excited in the nano-notch have a relatively high frequency, near 10 GHz, as seen in

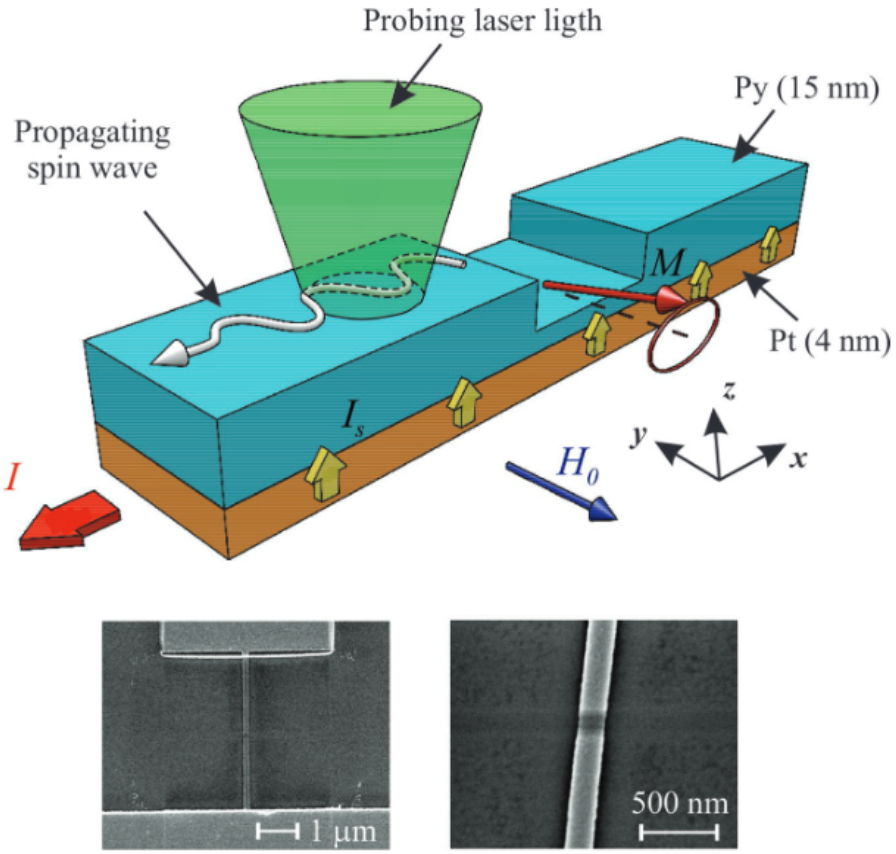

Figure 7.6: Schematic depicting the experiment. The sample is a 180nm wide, 5μm long Pt(4nm)Py(15nm) wire. There is a 200nm long region in the center of the wire where the Py layer is ion-milled down to a thickness of 5nm.

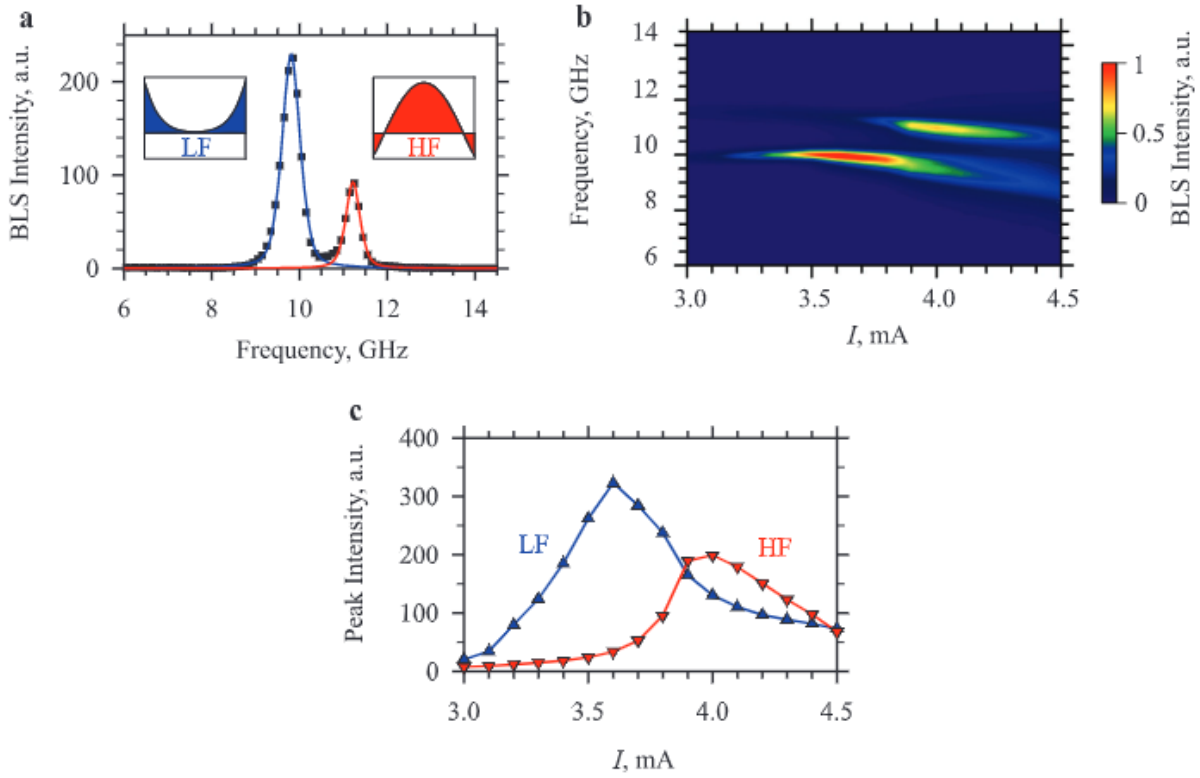

Figure 7.7: Spectral characteristics of the 'auto-oscillation' modes excited in the nano-notch region of the magnetic nanowire. Representative BLS spectrum of auto-oscillations measured at I= 3.8 mA with the probing spot positioned on the nanonotch. Symbols: experimental data, lines: Lorentzian fits of the spectral peaks. Insets schematically show the transverse profiles of the dynamic magnetization corresponding to the low-frequency (LF) and the high-frequency (HF) mode. b) Normalized color-coded map of the BLS intensity in the frequency–current coordinates. c) Current dependences of the peak intensity for the LF and the HF mode. Symbols: experimental data; lines: guides for the eye. The measurements were performed at $H_0 = 2000$ Oe.

figure 7.7. Let's call it f_0. The spin waves with frequency f_0 from the linear spectrum in the wire are characterized by larger wavevectors and group velocities, compared to the lowest frequency modes. Once the nonlinear, coherent spin wave modes are excited in the nano-notch, they can couple to the modes from the linear spectrum in the wire with frequencies near f_0. Compared to the devices described in the previous section, these indirectly excited linear spin wave modes will travel farther due to the larger wavevector and group velocity of the spin waves.

So to recap, large amplitudes of moderately high frequency, coherent spin waves are generated in the nano-notch region. These spin waves couple to the linear spin wave spectrum in the wire, allowing for the propagation of the coherent spin waves along the wire. There is one final physical effect that enhances the propagation of these spin waves. The spin current driven into the wire, while not strong enough to induce auto-oscillations, does partially compensate the magnetic damping [figure 7.1]. This allows the coherent spin

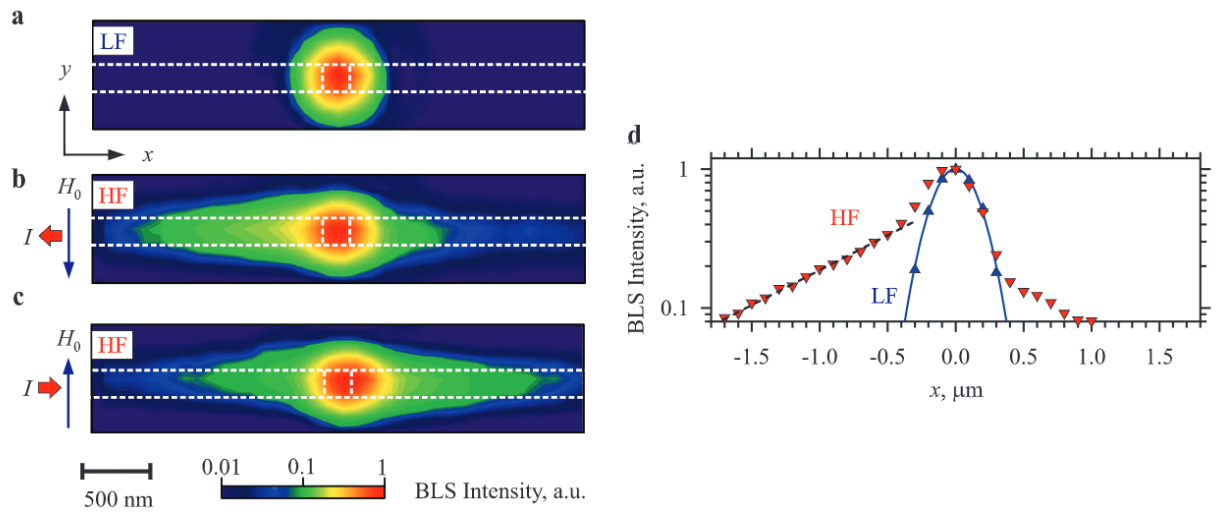

Figure 7.8: Coherent spin wave emission by the nanonotch oscillator. a,b) Color-coded spatial maps of the BLS intensity measured at the frequency of the LF and the HF mode, as labeled. The maps were recorded at I= 4.0 mA and $H_0 = 2000$. Dashed lines on the maps show the outlines of the waveguide and of the nanonotch. c) Same as (b), measured with reversed directions of the static magnetic field and of the driving current. d) Symbols: dependence of the BLS intensity for LF and HF modes, as labeled, on the propagation coordinate. Note the logarithmic intensity scale. Solid curve: Gaussian fit of the data for the LF mode; dashed line: exponential fit of the data for the HF mode at x < -0.5 μm.

waves to propagate farther along the wire before dissipating.

In figure 7.8, the spatial profiles of the spin wave amplitudes are shown, indicating that the low frequency 'bullet' mode is localized near the nano-notch region, while the higher frequency 'quasi-linear' mode propagates along the wire. As expected from linear spin wave theory, the propagation direction of this mode can be reversed by reversing the direction of the external field. The interested reader can read about 'Damon-Eshbach' modes in [1] for derivations and details about this effect.

However, even with all of these fancy geometric tricks to enable and enhance the propagation of the coherent spin waves, the propagation length is still quite small, as seen in figure 7.8(d). These data clearly demonstrate that the spin waves emitted by the HF mode exponentially decay away from the nanonotch. By fitting the data with the exponential function, we find the decay length L = 1.5μm, at which the amplitude of the wave decreases by a factor of three. By comparing the intensities of the waves emitted to the left and to the right, we also determine that the decay length is the same for the two directions, but the intensities differ by about a factor of three. This finite, albeit small propagation length for coherent, high amplitude spin waves, excited at low currents is a notable technical achievement. It points to the difficulties that must be overcome before coherent spin waves can become a major component of computing technologies, as well as the open research opportunities present around the generation and propagation of coherent spin waves.

Chapter 8

Conclusion

In this thesis, I've outlined 6 research directions in which I was involved during my PhD research in Dr. Urazhdin's lab. The work was driven by experiments, mostly electronic and optical, but were supplemented with simulations and some theory. My PhD had a broad focus, compared to many other physics PhDs, so it can be beneficial to break down the general directions of research that my projects can be broken down into, the key results of my PhD, and how they fit into their respective research communities.

Each of my projects involved some combination of three topics: magnetism, electron dynamics, and optical metamaterials, allowing our group to study several different aspects of electromagnetism. We studied how electrons could be manipulated at different voltages and under different external conditions (temperature, external magnetic field etc.) to interact with magnetic materials. With the optical metamaterials, we studied how the properties of light can be modified by materials with carefully chosen material properties and geometries to change how the light interacts with magnetic materials.

Specifically, one of the big questions that our group was interested in answering was, "What is the relationship between magnetism and spin-orbit effects?" This was especially central to my work on spin relaxation in Pt. Projects like this one are important to the nanomagnetism research community, because it is often difficult to distinguish, both conceptually and experimentally, the effects of different types of magnetic moments and fields. For instance, the spin Hall effect is thought to have some contribution from the orbital angular momentum of electrons, and some contribution from their spins, but experimentally one is usually only sensitive to the net flow of angular momentum. Furthermore, the spin Hall effect is attributed to spin-orbit interaction in bulk materials, which cannot be described as the effects of an effective magnetic field, but often contains contributions from the actual magnetic fields present at interfaces due to the spin-orbit interaction. Consequently, much of the nanomagnetism community holds pretty simplified

understandings of the relevant magnetic effects, without always understanding key underlying details.

My work on Pt [36] was a small puzzle piece helping to clarify the influence of magnetic fields and spin-orbit interaction on electron spins. I saw experimental results that could not be explained my modern theories and proposed a new spin-orbit mechanism by which electron spins can depolarize. One of the key results in that project was that this spin relaxation mechanism seemed to be suppressed by the presence of the exchange field when Pt is directly interfaced with a magnetic material. In this way, we saw a direct competition between the effects of magnetism and spin-orbit interaction on the dynamics of the spins in the studied circuit. To drive home this analogy, we approximated the newly discovered spin-orbit effect relaxation mechanism as a magnetic field and showed that the behavior of the electron spins were qualitatively different in the limits of strong or weak local magnetic fields. However, as we continued to think about this project, it became clear that analogy is only a cartoon, and its limitations actually show a key difference between magnetism and some spin-orbit effects. This has to do with symmetry. Spins precess around magnetic fields, because there is a well defined vector nature to the field: in some way the spatial symmetry around the spin is broken. Some spin-orbit effects are a direct consequence of broken spatial symmetries (Dzyaloshinskii-Moriya interaction, Rashba fields, Dresselhaus effect, etc.) and therefore lead to spin-orbit fields with well defined vector natures. However, the spin-orbit effect that we discussed was a band-structure effect, and while it directly influenced the state of the electron spin, it was not associated with a particular broken spatial symmetry. Consequently there is no vector field about which the spins can precess. The spin-orbit interaction in this case acted to mix up spin-up and spin-down bands, leading to depolarized spin states. As nanomagnetism research continues to grow, it will be important for the community to carefully understand the differences between the spin and orbital degrees of freedom of electrons.

I was involved in varying degrees with the other projects discussed in my PhD, but as a contributing author, do not wish to take too much credit for making major contributions to the respective research communities. However, the major results for those projects can be still be stated here. In "Spin-Transfer due to quantum magnetization fluctuations" [37], we showed that the process of spin transfer, while often approximated as a semi-classical effect, has some aspects that are strictly quantum and do not have classical analogies. Specifically, we showed that electrons scattering with magnetic systems generate magnons by both spontaneous and stimulated emission, like the process underlying lasing, and that this process is relevant at temperatures much higher than most people in the magnetism research community expected. In "Anti-reflection coating design for metallic terahertz meta-materials" [38] we showed that the drastic difference in wavelengths between the THz 'pump' and optical 'probe' beams in many THz experiments can be exploited to significantly enhance the capabilities of the experimental technique. By implementing an optical quarter-wave interference coating, we drastically increased the signal to noise ratio of the experiment without influencing

the THz physics that the experiment was probing. In the papers related to nonlinear spin wave modes [39, 40], we studied how to generate and control spin waves in the high current density, nonlinear regime, where interactions between magnons have strong effects on the dynamics of the spin wave modes. These projects helped the research community understand how these modes are formed, the time scales over which they evolve, and their spectral properties. By creating a special magnetoelectronic circuit, one of the key aspects of these spin wave modes that limits their application was overcome. Generally, these nonlinear modes are localized due to the bosonic attraction between magnons, meaning that they cannot be launched down waveguides. The circuit studied in the paper overcomes this limitation by locally generating the nonlinear spin wave mode and launching it down a waveguide with a carefully chosen geometry. In this waveguide, the spin wave spectrum matches up with the frequency of the nonlinear mode. This allows the nonlinear mode to be excited locally, then couple to the linear spin wave spectrum in the waveguide that is allowed to propagate. If spin waves are to be used in next generation information transfer technologies, the ability to create large amplitude propagating spin waves will be key.

Finally, I was the primary author on "Brillouin light spectroscopy from optically inaccessible spin waves" (submitted to Physical Review Letters). The original goal of this work was technical and applied, "increase the intensity and spectral resolution of BLS". BLS suffers from both a low signal to noise ratio and a low spectral range. We attempted to overcome this limitation by using a nanoscale conductive antenna, to localize the energy of the incident light, and broaden the wavevector distribution of the local field. While working on this project, we were able to clarify physics about light scattering at nanoscale that had not been previously understood. This is interesting, because in many way light scattering seems like old news. There are whole textbooks discussing the subject. However, many of these textbooks were written before modern nanolithography techniques were invented, and consequently, the way that they discuss the subject usually contains the underlying assumption that the spatial profile of the incident beam is mostly uniform. However, in our project, we use a nanoscale conductive antenna specifically to modulate the spatial profile of the incident beam. This is further complicated by the fact that light rotates its polarization upon scattering with spin waves. The antenna that localizes the incident field also acts to re-radiate the photons after scattering, however, the properties of the antenna are strongly polarization dependent. These ingredients combined together to create a unique light scattering problem that hadn't explicitly been clarified in textbooks. Ultimately, we were able to account for these effects by an equation for the spectra of spin waves scattered by light facilitated by the nano-antenna. This expression is similar to what is found in Landau-Lifshitz "Electrodynamics of Continuous Media", but is written in a way that carefully accounts for the spatial modulation of the incident field and the polarization-dependent field localization and re-radiation.

This expression was not known to the community of researchers that perform and study Brillouin light

spectroscopy. Of note, there is a key detail in the expression that can be taken advantage of in future implementations of BLS: the local electric field before and after scattering are both equally important to the light scattering process. The antenna that we used was designed to be plasmonically resonant. However, most applications of plasmonically resonant antennas don't involve a process that rotates the polarization of light, so the antenna was only designed to be resonant for a single polarization of incident field. Our expression for the BLS cross-section shows that an antenna that is resonant for both the polarization of incident and the rotated polarization of the re-radiated light would be dramatically more effective. Our work clearly delineates new knowledge that can be utilized for various applications that involve light scattering and/or plasmonic resonances. Plasmonically resonant nanoparticles would, in theory, be the next step of nanostructure assisted light scattering, as their symmetry allows them to both resonantly localize and radiate the light involved in scattering. This could be a major step for spectroscopy in general. We showed some preliminary results along this direction, and they were quite promising, showing no discernible decrease in the light scattering cross section over the entire frequency range at which we measured. By clarifying these important details of nano-optics, we have shown how spatially modulating incident light with metamaterials can dramtically change the light-matter interactions, and paved the way for future researchers to implement similar nano-antenna and nanoparticles to dramatically alter the light-matter interaction in ways that could be useful for a variety of applications.

I'm happy with how my PhD turned out. I've learned quite a lot, and have made specific significant contributions to modern fields of physics. Thanks to everyone who was involved in each step along the way!

Bibliography

[1] D. Stancil and A. Prabhakar, *Spin Waves - Theory and Applications*. Springer, 2009.

[2] I. Abdullah, "Phd of iman abdullah," 2016.

[3] Gorchy, "neodymium magnetic domains," 2004.

[4] M. GmbH, "Magnetic bubble domains," 2011.

[5] S. O. Demokritov, B. Hillebrands, and A. N. Slavin, "Brillouin light scattering studies of confined spin waves: linear and nonlinear confinement," *Physics Reports*, vol. 348, no. 6, pp. 441–489, 2001.

[6] A. Hoffmann, "Spin hall effects in metals," *IEEE transactions on magnetics*, vol. 49, no. 10, pp. 5172–5193, 2013.

[7] K. Ando, S. Takahashi, J. Ieda, H. Kurebayashi, T. Trypiniotis, C. Barnes, S. Maekawa, and E. Saitoh, "Electrically tunable spin injector free from the impedance mismatch problem," *Nature materials*, vol. 10, no. 9, pp. 655–659, 2011.

[8] E. Y. Tsymbal and D. G. Pettifor, "Perspectives of giant magnetoresistance," in *Solid state physics*, vol. 56, pp. 113–237, Elsevier, 2001.

[9] "About lock-in amplifiers," *Stanford Research Instruments*.

[10] P. Boross, B. Dora, A. Kiss, and F. Simon, "A unified theory of spin-relaxation due to spin-orbit coupling in metals and semiconductors," *Scientific Reports*, vol. 3, nov 2013.

[11] M. Gradhand, D. V. Fedorov, F. Pientka, P. Zahn, I. Mertig, and B. L. Györffy, "First-principle calculations of the berry curvature of bloch states for charge and spin transport of electrons," *Journal of Physics: Condensed Matter*, vol. 24, no. 21, p. 213202, 2012.

[12] G. Y. Guo, S. Murakami, T.-W. Chen, and N. Nagaosa, "Intrinsic spin hall effect in platinum: First-principles calculations," *Physical Review Letters*, vol. 100, mar 2008.

[13] W. L. Lim, N. Ebrahim-Zadeh, J. C. Owens, H. G. E. Hentschel, and S. Urazhdin, "Temperature-dependent proximity magnetism in pt," *Applied Physics Letters*, vol. 102, p. 162404, apr 2013.

[14] A. Zholud, *Andrei Zholud's PhD thesis - Effect of current of spin current on magnetization dynamics.* 2017.

[15] See the supplementary materials that accompany this article.

[16] C. Kittel, *Introduction to solid state physics. Fifth edition.* John Wiley and Sons, Jan 1976.

[17] S. T. T. for Dummies *PPT on NIST website:.*

[18] R. O'Handley, *Modern Magnetic Materials: Principles and Applications.* John Wiley and Sons, 2000.

[19] S. O. Demokritov, *Spin wave confinement.* Pan Stanford Publishing, 2009.

[20] R. M. White, *Quantum Theory of Magnetism.* Springer Berlin Heidelberg, 2007.

[21] W. Nolting and A. Ramakanth, *Quantum theory of magnetism.* Springer Science & Business Media, 2009.

[22] H. Yang, A. Thiaville, S. Rohart, A. Fert, and M. Chshiev, "Anatomy of dzyaloshinskii-moriya interaction at co/pt interfaces," *Physical review letters*, vol. 115, no. 26, p. 267210, 2015.

[23] S.-G. Je, D.-H. Kim, S.-C. Yoo, B.-C. Min, K.-J. Lee, and S.-B. Choe, "Asymmetric magnetic domain-wall motion by the dzyaloshinskii-moriya interaction," *Physical Review B*, vol. 88, no. 21, p. 214401, 2013.

[24] P. Carcia, A. Meinhaldt, and A. Suna, "Perpendicular magnetic anisotropy in pd/co thin film layered structures," *Applied Physics Letters*, vol. 47, no. 2, pp. 178–180, 1985.

[25] A. Fert, V. Cros, and J. Sampaio, "Skyrmions on the track," *Nature nanotechnology*, vol. 8, no. 3, pp. 152–156, 2013.

[26] A. Malozemoff, "Random-field model of exchange anisotropy at rough ferromagnetic-antiferromagnetic interfaces," *Physical review B*, vol. 35, no. 7, p. 3679, 1987.

[27] S. Miura, M. Mino, and H. Yamazaki, "Relaxation of labyrinth domain structure of ferromagnetic thin film under field cycles," *Journal of the Physical Society of Japan*, vol. 70, no. 10, pp. 2821–2824, 2001.

[28] S. Urazhdin and U. Danilenko, "Cooperative multiscale aging in a ferromagnet/antiferromagnet bilayer," *Physical Review B*, vol. 92, no. 17, p. 174416, 2015.

[29] T. Ma and S. Urazhdin, "Spin glass transition in a thin-film nio/permalloy bilayer," *Physical Review B*, vol. 97, no. 5, p. 054402, 2018.

[30] S. O. Demokritov, *Spin wave confinement*. Jenny Stanford Publishing, 2019.

[31] S. O. Demokritov, V. E. Demidov, O. Dzyapko, G. A. Melkov, A. A. Serga, B. Hillebrands, and A. N. Slavin, "Bose–einstein condensation of quasi-equilibrium magnons at room temperature under pumping," *Nature*, vol. 443, no. 7110, pp. 430–433, 2006.

[32] S. A. Wolf, D. D. Awschalom, R. A. Buhrman, J. M. Daughton, S. von Molnar, M. L. Roukes, A. Y. Chtchelkanova, and D. M. Treger, "Spintronics: A spin-based electronics vision for the future," *Science*, vol. 294, no. 5546, pp. 1488–1495, 2001.

[33] K. Ando, S. Takahashi, K. Harii, K. Sasage, J. Ieda, S. Maekawa, and E. Saitoh, "Electric manipulation of spin relaxation using the spin hall effect," *Physical review letters*, vol. 101, no. 3, p. 036601, 2008.

[34] C. Hahn, G. de Loubens, O. Klein, M. Viret, V. V. Naletov, and J. Ben Youssef, "Comparative measurements of inverse spin hall effects and magnetoresistance in yig/pt and yig/ta," *Phys. Rev. B*, vol. 87, p. 174417, May 2013.

[35] M. I. Dyakonov and V. Perel, "Current-induced spin orientation of electrons in semiconductors," *Physics Letters A*, vol. 35, no. 6, pp. 459–460, 1971.

[36] R. Freeman, A. Zholud, Z. Dun, H. Zhou, and S. Urazhdin, "Evidence for dyakonov-perel-like spin relaxation in pt," *Physical review letters*, vol. 120, no. 6, p. 067204, 2018.

[37] A. Zholud, R. Freeman, R. Cao, A. Srivastava, and S. Urazhdin, "Spin transfer due to quantum magnetization fluctuations," *Physical review letters*, vol. 119, no. 25, p. 257201, 2017.

[38] M. Pancaldi, R. Freeman, M. Hudl, M. C. Hoffmann, S. Urazhdin, P. Vavassori, and S. Bonetti, "Anti-reflection coating design for metallic terahertz meta-materials," *Optics express*, vol. 26, no. 3, pp. 2917–2927, 2018.

[39] B. Divinskiy, V. E. Demidov, S. Urazhdin, R. Freeman, A. B. Rinkevich, and S. O. Demokritov, "Excitation and amplification of spin waves by spin–orbit torque," *Advanced Materials*, vol. 30, no. 33, p. 1802837, 2018.

[40] B. Divinskiy, V. Demidov, S. Urazhdin, R. Freeman, A. Rinkevich, and S. Demokritov, "Controllable excitation of quasi-linear and bullet modes in a spin-hall nano-oscillator," *Applied Physics Letters*, vol. 114, no. 4, p. 042403, 2019.

[41] L. Novotny and B. Hect, *Principles of Nano-Optics*. Cambridge University Press, 2012.

[42] S. A. Maier, *Plasmonics: fundamentals and applications*. Springer Science & Business Media, 2007.

[43] C. Gerry, P. Knight, and P. L. Knight, *Introductory quantum optics*. Cambridge university press, 2005.

[44] I. Žutić, J. Fabian, and S. D. Sarma, "Spintronics: Fundamentals and applications," *Reviews of modern physics*, vol. 76, no. 2, p. 323, 2004.

[45] D. Ralph and M. Stiles, "Spin transfer torques," *Journal of Magnetism and Magnetic Materials*, vol. 320, no. 7, pp. 1190 – 1216, 2008.

[46] S. Bader and S. Parkin, "Spintronics," *Annual Review of Condensed Matter Physics*, vol. 1, no. 1, pp. 71–88, 2010.

[47] G. Bauer, E. Saitoh, and B. van Wees, "Spin calitronics," *Nature Materials*, vol. 11, pp. 391–399, 2012.

[48] A. Manchon, H. C. Koo, J. Nitta, S. M. Frolov, and R. A. Duine, "New perspectives for rashba spin–orbit coupling," *Nature Materials*, vol. 14, pp. 871–882, Aug. 2015.

[49] M. D'Yakonov and V. Perel, "Possibility of orienting electron spins with current," *Journal of Experimental and Theoretical Physics Letters*, vol. 13, jun 1971.

[50] L. Liu, O. J. Lee, T. J. Gudmundsen, D. C. Ralph, and R. A. Buhrman, "Current-induced switching of perpendicularly magnetized magnetic layers using spin torque from the spin hall effect," *Phys. Rev. Lett.*, vol. 109, p. 096602, Aug 2012.

[51] J. Wunderlich, "Spintronics: Current-switched magnetic insulators," *Nature Materials*, vol. 16, pp. 284–285, Feb 2017.

[52] L. L, R. Buhrman, and D. Ralph, "Review and analysis of measurements of the spin hall effect in platinum," *arXiv*, Nov 2011.

[53] L. Liu, C.-F. Pai, Y. Li, H. W. Tseng, D. C. Ralph, and R. A. Buhrman, "Spin-torque switching with the giant spin hall effect of tantalum," *Science*, vol. 336, no. 6081, pp. 555–558, 2012.

[54] C.-F. Pai, L. Liu, Y. Li, H. W. Tseng, D. C. Ralph, and R. A. Buhrman, "Spin transfer torque devices utilizing the giant spin hall effect of tungsten," *Applied Physics Letters*, vol. 101, no. 12, p. 122404, 2012.

[55] Y. Niimi, Y. Kawanishi, D. H. Wei, C. Deranlot, H. X. Yang, M. Chshiev, T. Valet, A. Fert, and Y. Otani, "Giant spin hall effect induced by skew scattering from bismuth impurities inside thin film cubi alloys," *Phys. Rev. Lett.*, vol. 109, p. 156602, Oct 2012.

[56] J.-C. Rojas-Sanchez, N. Reyren, P. Laczkowski, W. Savero, J.-P. Attane, C. Deranlot, M. Jamet, J.-M. George, L. Vila, and H. Jaffres, "Spin pumping and inverse spin hall effect in platinum: The essential role of spin-memory loss at metallic interfaces," *Physical Review Letters*, vol. 112, mar 2014.

[57] K. D. Belashchenko, A. A. Kovalev, and M. van Schilfgaarde, "Theory of spin loss at metallic interfaces," *Phys. Rev. Lett.*, vol. 117, p. 207204, Nov 2016.

[58] L. Liu, T. Moriyama, D. C. Ralph, and R. A. Buhrman, "Spin-torque ferromagnetic resonance induced by the spin hall effect," *Phys. Rev. Lett.*, vol. 106, p. 036601, Jan 2011.

[59] C. Jaworski, R. Myers, E. Johnston-Halperin, and J. Heremans, "Giant spin seebeck effect in a non-magnetic material," *Nature*, vol. 487, pp. 210–213, Jul 2012.

[60] J. Bass and W. P. Pratt, "Spin-diffusion lengths in metals and alloys, and spin-flipping at metal/metal interfaces: an experimentalist's critical review," *Journal of Physics: Condensed Matter*, vol. 19, p. 183201, Apr. 2007.

[61] F. D. Czeschka, L. Dreher, M. S. Brandt, M. Weiler, M. Althammer, I.-M. Imort, G. Reiss, A. Thomas, W. Schoch, W. Limmer, H. Huebl, R. Gross, and S. T. B. Goennenwein, "Scaling behavior of the spin pumping effect in ferromagnet-platinum bilayers," *Phys. Rev. Lett.*, vol. 107, p. 046601, Jul 2011.

[62] W. Zhang, V. Vlaminck, J. E. Pearson, R. Divan, S. D. Bader, and A. Hoffmann, "Determination of the pt spin diffusion length by spin-pumping and spin hall effect," *Applied Physics Letters*, vol. 103, no. 24, p. 242414, 2013.

[63] M. Isasa, E. Villamor, L. E. Hueso, M. Gradhand, and F. Casanova, "Temperature dependence of spin diffusion length and spin hall angle in au and pt," *Physical Review B*, vol. 91, jan 2015.

[64] C. Stamm, C. Murer, M. Berritta, J. Fang, M. Gabureac, P. Oppeneeer, and P. Gambardella, "Magneto-optical detection of the spin hall effect in pt and w thin films," *arXiv*, apr 2017.

[65] W. Zhang, W. Han, X. Jiang, S.-H. Yang, and S. S. P. Parkin, "Role of transparency of platinum-ferromagnet interfaces in determining the intrinsic magnitude of the spin hall effect," *Nature Physics*, vol. 11, pp. 496–502, apr 2015.

[66] K. Roy, "Estimating the spin diffusion length and spin hall angle from spin-pumping-induced inverse spin hall voltages," *arXiv*, mar 2017.

[67] H. Nguyen, W. P. Jr., and J. Bass, "Spin-flipping in pt and at co/pt interfaces," *Journal of Magnetism and Magnetic Materials*, vol. 361, pp. 30 – 33, 2014.

[68] M.-H. Nguyen, D. Ralph, and R. Buhrman, "Spin torque study of the spin hall conductivity and spin diffusion length in platinum thin films with varying resistivity," *Physical Review Letters*, vol. 116, mar 2016.

[69] I. Zutic, J. Fabian, and S. D. Sarma, "Spintronics: Fundamentals and applications," *Reviews of Modern Physics*, vol. 76, pp. 323–410, apr 2004.

[70] W. Zhang, M. B. Jungfleisch, W. Jiang, Y. Liu, J. E. Pearson, S. G. E. te Velthuis, A. Hoffmann, F. Freimuth, and Y. Mokrousov, "Reduced spin-hall effects from magnetic proximity," *Physical Review B*, vol. 91, mar 2015.

[71] F. Hellman, A. Hoffmann, Y. Tserkovnyak, G. S. D. Beach, E. E. Fullerton, C. Leighton, A. H. MacDonald, D. C. Ralph, D. A. Arena, H. A. Dürr, P. Fischer, J. Grollier, J. P. Heremans, T. Jungwirth, A. V. Kimel, B. Koopmans, I. N. Krivorotov, S. J. May, A. K. Petford-Long, J. M. Rondinelli, N. Samarth, I. K. Schuller, A. N. Slavin, M. D. Stiles, O. Tchernyshyov, A. Thiaville, and B. L. Zink, "Interface-induced phenomena in magnetism," *Rev. Mod. Phys.*, vol. 89, p. 025006, Jun 2017.

[72] J. Ryu, M. Kohda, and J. Nitta, "Observation of the d'yakonov-perel' spin relaxation in single-crystalline pt thin films," *Phys. Rev. Lett.*, vol. 116, p. 256802, Jun 2016.

[73] K. Belashchenko, A. A. Kovalev, and M. van Schilfgaarde, "Theory of spin loss at metallic interfaces," *Physical Review Letters*, vol. 117, Nov. 2016.

[74] V. P. Amin and M. D. Stiles, "Spin transport at interfaces with spin-orbit coupling: Formalism," *Physical Review B*, vol. 94, Sept. 2016.

[75] A. Brataas, Y. V. Nazarov, and G. E. Bauer, "Finite-element theory of transport in ferromagnet–normal metal systems," *Physical review letters*, vol. 84, no. 11, p. 2481, 2000.

[76] M. N. Baibich, J. M. Broto, A. Fert, F. N. Van Dau, F. Petroff, P. Etienne, G. Creuzet, A. Friederich, and J. Chazelas, "Giant magnetoresistance of (001)fe/(001)cr magnetic superlattices," *Phys. Rev. Lett.*, vol. 61, pp. 2472–2475, Nov 1988.

[77] E. N. Koukaras, "Fermi's golden rule," *Lecture Notes from University of Science and Technology of China*.

[78] S. Urazhdin, H. Kurt, W. Pratt Jr, and J. Bass, "Effect of antiferromagnetic interlayer coupling on current-assisted magnetization switching," *Applied physics letters*, vol. 83, no. 1, pp. 114–116, 2003.

[79] C.-F. Pai, Y. Ou, L. H. Vilela-Leao, D. C. Ralph, and R. A. Buhrman, "Dependence of the efficiency of spin hall torque on the transparency of pt/ferromagnetic layer interfaces," *Physical Review B*, vol. 92, aug 2015.

[80] T. Valet and A. Fert, "Theory of the perpendicular magnetoresistance in magnetic multilayers," *Phys. Rev. B*, vol. 48, pp. 7099–7113, Sep 1993.

[81] A. Fert and S.-F. Lee, "Theory of the bipolar spin switch," *Phys. Rev. B*, vol. 53, pp. 6554–6565, Mar 1996.

[82] P. C. van Son, H. van Kempen, and P. Wyder, "Boundary resistance of the ferromagnetic-nonferromagnetic metal interface," *Phys. Rev. Lett.*, vol. 58, pp. 2271–2273, May 1987.

[83] J. Bass and W. P. Jr., "Current-perpendicular (cpp) magnetoresistance in magnetic metallic multilayers," *Journal of Magnetism and Magnetic Materials*, vol. 200, no. 1–3, pp. 274 – 289, 1999.

[84] "Measured in our lab, using the approaches discussed in the text."

[85] S. Steenwyk, S. Hsu, R. Loloee, J. Bass, and W. P. Jr., "Perpendicular current exchange biased spin-valve evidence for a short spindiffusion length in permalloy," *Journal Magnetism and Magnetic Materials*, vol. 170, no. L1, 1997.

[86] H. Kurt, R. Loloee, K. Eid, W. P. Pratt, and J. Bass, "Spin-memory loss at 4.2 k in sputtered pd and pt and at pd/cu and pt/cu interfaces," *Applied Physics Letters*, vol. 81, pp. 4787–4789, Dec. 2002.

[87] L. Vila, W. Park, J. Cabellero, D. Bozek, R. Loloee, W. Pratt, and J. Bass, "Current perpendicular magnetoresistance of nicofe and nife 'permalloys'," *Journal of Applied Physics*, vol. 87, no. 8610, 2000.

[88] E. Villamor, M. Isasa, L. E. Hueso, and F. Casanova, "Temperature dependence of spin polarization in ferromagnetic metals using lateral spin valves," *Phys. Rev. B*, vol. 88, p. 184411, Nov 2013.

[89] E. Sondheimer, "The mean free path of electrons in metals," *Advances in Physics*, vol. 1, no. 1, pp. 1–42, 1952.

[90] N. Ashcroft and N. Mermin, *Solid State Physics*. Cengage Learning, 2011.

[91] M. Dyakonov and V. Perel, "Spin relaxation of conduction electrons in noncentrosymmetric semiconductors," *Soviet Physics Solid State, Ussr*, vol. 13, no. 12, pp. 3023–3026, 1972.

[92] P. M. Haney, H.-W. Lee, K.-J. Lee, A. Manchon, and M. D. Stiles, "Current induced torques and interfacial spin-orbit coupling: Semiclassical modeling," *Physical Review B*, vol. 87, May 2013.

[93] C. Fang, C. H. Wan, B. S. Yang, J. Y. Qin, B. S. Tao, H. Wu, X. Zhang, X. F. Han, A. Hoffmann, X. M. Liu, and Z. M. Jin, "Determination of spin relaxation times in heavy metals via second-harmonic spin injection magnetoresistance," *Phys. Rev. B*, vol. 96, p. 134421, Oct 2017.

[94] R. I. Dzhioev, K. V. Kavokin, V. L. Korenev, M. V. Lazarev, N. K. Poletaev, B. P. Zakharchenya, E. A. Stinaff, D. Gammon, A. S. Bracker, and M. E. Ware, "Suppression of dyakonov-perel spin relaxation in high-mobilityn-GaAs," *Physical Review Letters*, vol. 93, Nov. 2004.

[95] H. Idzuchi, Y. Fukuma, L. Wang, and Y. Otani, "Spin relaxation mechanism in silver nanowires covered with mgo protection layer," *Applied Physics Letters*, vol. 101, no. 2, p. 022415, 2012.

[96] G. Mihajlović, J. E. Pearson, S. D. Bader, and A. Hoffmann, "Surface spin flip probability of mesoscopic ag wires," *Phys. Rev. Lett.*, vol. 104, p. 237202, Jun 2010.

[97] T. Kimura, T. Sato, and Y. Otani, "Temperature evolution of spin relaxation in a NiFe/Cu lateral spin valve," *Phys. Rev. Lett.*, vol. 100, p. 066602, Feb 2008.

[98] H. Kontani, T. Tanaka, D. S. Hirashima, K. Yamada, and J. Inoue, "Giant orbital hall effect in transition metals: Origin of large spin and anomalous hall effects," *Physical Review Letters*, vol. 102, jan 2009.

[99] "Foucault's pendulum," *Wikipedia*.

[100] "Adiabatic theorem," *Wikipedia*.

[101] A. Delin and E. Tosatti, "Emergent magnetism in platinum nanowires," *Surface Science*, vol. 566-568, pp. 262–267, 2004.

[102] X. Teng, W.-Q. Han, W. Ku, and M. Hucker, "Synthesis of ultrathin palladium and platinum nanowires and a study of their magnetic properties," *Angewandte Chemie*, vol. 120, no. 11, pp. 2085–2088, 2008.

[103] J. Beille, D. Bloch, and M. J. Besnus, "Itinerant ferromagnetism and susceptibility of nickel-platinum alloys," *Journal of Physics F: Metal Physics*, vol. 4, no. 8, p. 1275, 1974.

[104] K.-W. Kim, L. O'Brien, P. A. Crowell, C. Leighton, and M. D. Stiles, "Theory of kondo suppression of spin polarization in nonlocal spin valves," *Phys. Rev. B*, vol. 95, p. 104404, Mar 2017.

[105] R. E. Parra and R. A. López, "Magnetic environment model of ferromagnetism in dilute ptco alloys," *Journal of Applied Physics*, vol. 61, no. 8, pp. 3989–3990, 1987.

[106] J. C. Slonczewski *et al.*, "Current-driven excitation of magnetic multilayers," *Journal of Magnetism and Magnetic Materials*, vol. 159, no. 1, p. L1, 1996.

[107] L. Berger, "Emission of spin waves by a magnetic multilayer traversed by a current," *Physical Review B*, vol. 54, no. 13, p. 9353, 1996.

[108] S. Urazhdin, "Current-driven magnetization dynamics in magnetic multilayers," *Physical Review B*, vol. 69, no. 13, p. 134430, 2004.

[109] Y. Wang and L. Sham, "Quantum dynamics of a nanomagnet driven by spin-polarized current," *Physical Review B*, vol. 85, no. 9, p. 092403, 2012.

[110] G. E. Bauer, Y. Tserkovnyak, D. Huertas-Hernando, and A. Brataas, "Universal angular magnetoresistance and spin torque in ferromagnetic/normal metal hybrids," *Physical Review B*, vol. 67, no. 9, p. 094421, 2003.

[111] L. Spietz, K. Lehnert, I. Siddiqi, and R. Schoelkopf, "Primary electronic thermometry using the shot noise of a tunnel junction," *Science*, vol. 300, no. 5627, pp. 1929–1932, 2003.

[112] M. Polianski and P. Brouwer, "Current-induced transverse spin-wave instability in a thin nanomagnet," *Physical review letters*, vol. 92, no. 2, p. 026602, 2004.

[113] S. Mangin, D. Ravelosona, J. Katine, M. Carey, B. Terris, and E. E. Fullerton, "Current-induced magnetization reversal in nanopillars with perpendicular anisotropy," *Nature materials*, vol. 5, no. 3, pp. 210–215, 2006.

[114] T. Jungwirth, X. Marti, P. Wadley, and J. Wunderlich, "Antiferromagnetic spintronics," *Nature nanotechnology*, vol. 11, no. 3, p. 231, 2016.

[115] Y. Tserkovnyak, A. Brataas, and G. E. Bauer, "Enhanced gilbert damping in thin ferromagnetic films," *Physical review letters*, vol. 88, no. 11, p. 117601, 2002.

[116] E. Turgut, D. Zusin, D. Legut, K. Carva, R. Knut, J. M. Shaw, C. Chen, Z. Tao, H. T. Nembach, T. J. Silva, *et al.*, "Stoner versus heisenberg: Ultrafast exchange reduction and magnon generation during laser-induced demagnetization," *Physical Review B*, vol. 94, no. 22, p. 220408, 2016.

[117] G. E. Bauer, E. Saitoh, and B. J. Van Wees, "Spin caloritronics," *Nature materials*, vol. 11, no. 5, pp. 391–399, 2012.

[118] A. G. Gurevich and G. A. Melkov, *Magnetization oscillations and waves*. CRC press, 1996.

[119] M. C. Hoffmann and J. A. Fülöp, "Intense ultrashort terahertz pulses: generation and applications," *Journal of Physics D: Applied Physics*, vol. 44, no. 8, p. 083001, 2011.

[120] S. Bonetti, M. Hoffmann, M.-J. Sher, Z. Chen, S.-H. Yang, M. Samant, S. Parkin, and H. Dürr, "Thz-driven ultrafast spin-lattice scattering in amorphous metallic ferromagnets," *Physical review letters*, vol. 117, no. 8, p. 087205, 2016.

[121] M. Trigo, Y. Sheu, D. Arms, J. Chen, S. Ghimire, R. Goldman, E. Landahl, R. Merlin, E. Peterson, M. Reason, *et al.*, "Probing unfolded acoustic phonons with x rays," *Physical review letters*, vol. 101, no. 2, p. 025505, 2008.

[122] M. Liu, H. Y. Hwang, H. Tao, A. C. Strikwerda, K. Fan, G. R. Keiser, A. J. Sternbach, K. G. West, S. Kittiwatanakul, J. Lu, *et al.*, "Terahertz-field-induced insulator-to-metal transition in vanadium dioxide metamaterial," *Nature*, vol. 487, no. 7407, pp. 345–348, 2012.

[123] D. Daranciang, M. J. Highland, H. Wen, S. M. Young, N. C. Brandt, H. Y. Hwang, M. Vattilana, M. Nicoul, F. Quirin, J. Goodfellow, *et al.*, "Ultrafast photovoltaic response in ferroelectric nanolayers," *Physical review letters*, vol. 108, no. 8, p. 087601, 2012.

[124] R. Mankowsky, A. Subedi, M. Först, S. O. Mariager, M. Chollet, H. Lemke, J. S. Robinson, J. M. Glownia, M. P. Minitti, A. Frano, *et al.*, "Nonlinear lattice dynamics as a basis for enhanced superconductivity in yba 2 cu 3 o 6.5," *Nature*, vol. 516, no. 7529, pp. 71–73, 2014.

[125] U. Staub, R. De Souza, P. Beaud, E. Möhr-Vorobeva, G. Ingold, A. Caviezel, V. Scagnoli, B. Delley, W. Schlotter, J. Turner, *et al.*, "Persistence of magnetic order in a highly excited cu 2+ state in cuo," *Physical Review B*, vol. 89, no. 22, p. 220401, 2014.

[126] P. Beaud, A. Caviezel, S. Mariager, L. Rettig, G. Ingold, C. Dornes, S. Huang, J. Johnson, M. Radovic, T. Huber, *et al.*, "A time-dependent order parameter for ultrafast photoinduced phase transitions," *Nature materials*, vol. 13, no. 10, pp. 923–927, 2014.

[127] T. Kubacka, J. A. Johnson, M. C. Hoffmann, C. Vicario, S. De Jong, P. Beaud, S. Grübel, S.-W. Huang, L. Huber, L. Patthey, *et al.*, "Large-amplitude spin dynamics driven by a thz pulse in resonance with an electromagnon," *Science*, vol. 343, no. 6177, pp. 1333–1336, 2014.

[128] G. L. Dakovski, W.-S. Lee, D. G. Hawthorn, N. Garner, D. Bonn, W. Hardy, R. Liang, M. C. Hoffmann, and J. J. Turner, "Enhanced coherent oscillations in the superconducting state of underdoped yb a 2 c u 3 o 6+ x induced via ultrafast terahertz excitation," *Physical Review B*, vol. 91, no. 22, p. 220506, 2015.

[129] M. P. Dean, Y. Cao, X. Liu, S. Wall, D. Zhu, R. Mankowsky, V. Thampy, X. Chen, J. G. Vale, D. Casa, *et al.*, "Ultrafast energy-and momentum-resolved dynamics of magnetic correlations in the photo-doped mott insulator sr 2 iro 4," *Nature materials*, vol. 15, no. 6, pp. 601–605, 2016.

[130] T. Henighan, M. Trigo, M. Chollet, J. Clark, S. Fahy, J. Glownia, M. Jiang, M. Kozina, H. Liu, S. Song, *et al.*, "Control of two-phonon correlations and the mechanism of high-wavevector phonon generation by ultrafast light pulses," *Physical Review B*, vol. 94, no. 2, p. 020302, 2016.

[131] S. Grübel, J. Johnson, P. Beaud, C. Dornes, A. Ferrer, V. Haborets, L. Huber, T. Huber, A. Kohutych, T. Kubacka, *et al.*, "Ultrafast x-ray diffraction of a ferroelectric soft mode driven by broadband terahertz pulses," *arXiv preprint arXiv:1602.05435*, 2016.

[132] F. Chen, Y. Zhu, S. Liu, Y. Qi, H. Hwang, N. Brandt, J. Lu, F. Quirin, H. Enquist, P. Zalden, *et al.*, "Ultrafast terahertz-field-driven ionic response in ferroelectric batio 3," *Physical Review B*, vol. 94, no. 18, p. 180104, 2016.

[133] C. J. Brennan and K. A. Nelson, "Direct time-resolved measurement of anharmonic lattice vibrations in ferroelectric crystals," *The Journal of chemical physics*, vol. 107, no. 22, pp. 9691–9694, 1997.

[134] H.-T. Chen, W. J. Padilla, J. M. Zide, A. C. Gossard, A. J. Taylor, and R. D. Averitt, "Active terahertz metamaterial devices," *Nature*, vol. 444, no. 7119, pp. 597–600, 2006.

[135] L. Razzari, A. Toma, M. Shalaby, M. Clerici, R. P. Zaccaria, C. Liberale, S. Marras, I. A. Al-Naib, G. Das, F. De Angelis, *et al.*, "Extremely large extinction efficiency and field enhancement in terahertz resonant dipole nanoantennas," *Optics express*, vol. 19, no. 27, pp. 26088–26094, 2011.

[136] C. A. Werley, K. Fan, A. C. Strikwerda, S. M. Teo, X. Zhang, R. D. Averitt, and K. A. Nelson, "Time-resolved imaging of near-fields in thz antennas and direct quantitative measurement of field enhancements," *Optics express*, vol. 20, no. 8, pp. 8551–8567, 2012.

[137] J. Zhang, X. Zhao, K. Fan, X. Wang, G.-F. Zhang, K. Geng, X. Zhang, and R. D. Averitt, "Terahertz radiation-induced sub-cycle field electron emission across a split-gap dipole antenna," *Applied Physics Letters*, vol. 107, no. 23, p. 231101, 2015.

[138] M. Savoini, S. Grübel, S. Bagiante, H. Sigg, T. Feurer, P. Beaud, and S. L. Johnson, "Thz near-field enhancement by means of isolated dipolar antennas: the effect of finite sample size," *Optics express*, vol. 24, no. 5, pp. 4552–4562, 2016.

[139] M. Kozina, M. Pancaldi, C. Bernhard, T. van Driel, J. M. Glownia, P. Marsik, M. Radovic, C. A. Vaz, D. Zhu, S. Bonetti, *et al.*, "Local terahertz field enhancement for time-resolved x-ray diffraction," *Applied Physics Letters*, vol. 110, no. 8, p. 081106, 2017.

[140] K. Balasubramanian, A. Marathay, and H. Macleod, "Modeling magneto-optical thin film media for optical data storage," *Thin Solid Films*, vol. 164, pp. 391–403, 1988.

[141] R. Atkinson, I. Salter, and J. Xu, "Quadrilayer magneto-optic enhancement with zero kerr ellipticity," *Journal of magnetism and magnetic materials*, vol. 102, no. 3, pp. 357–364, 1991.

[142] N. Qureshi, H. Schmidt, and A. Hawkins, "Cavity enhancement of the magneto-optic kerr effect for optical studies of magnetic nanostructures," *Applied Physics Letters*, vol. 85, no. 3, pp. 431–433, 2004.

[143] N. Qureshi, S. Wang, M. A. Lowther, A. R. Hawkins, S. Kwon, A. Liddle, J. Bokor, and H. Schmidt, "Cavity-enhanced magnetooptical observation of magnetization reversal in individual single-domain nanomagnets," *Nano letters*, vol. 5, no. 7, pp. 1413–1417, 2005.

[144] A. Barman, S. Wang, J. D. Maas, A. R. Hawkins, S. Kwon, A. Liddle, J. Bokor, and H. Schmidt, "Magneto-optical observation of picosecond dynamics of single nanomagnets," *Nano letters*, vol. 6, no. 12, pp. 2939–2944, 2006.

[145] S. Wang, A. Barman, H. Schmidt, J. Maas, A. Hawkins, S. Kwon, B. Harteneck, S. Cabrini, and J. Bokor, "Optimization of nano-magneto-optic sensitivity using dual dielectric layer enhancement," *Applied physics letters*, vol. 90, no. 25, p. 252504, 2007.

[146] P. Biagioni, J.-S. Huang, and B. Hecht, "Nanoantennas for visible and infrared radiation," *Reports on Progress in Physics*, vol. 75, no. 2, p. 024402, 2012.

[147] G. Hass, H. Schroeder, and A. Turner, "Mirror coatings for low visible and high infrared reflectance," *JOSA*, vol. 46, no. 1, pp. 31–35, 1956.

[148] S. Adachi and H. Mori, "Optical properties of fully amorphous silicon," *Physical Review B*, vol. 62, no. 15, p. 10158, 2000.

[149] M. Born and E. Wolf, *Principles of optics: electromagnetic theory of propagation, interference and diffraction of light*. Elsevier, 2013.

[150] F. D. Brunner, O.-P. Kwon, S.-J. Kwon, M. Jazbinšek, A. Schneider, and P. Günter, "A hydrogen-bonded organic nonlinear optical crystal for high-efficiency terahertz generation and detection," *Optics express*, vol. 16, no. 21, pp. 16496–16508, 2008.

[151] P. Vavassori, "Polarization modulation technique for magneto-optical quantitative vector magnetometry," *Applied Physics Letters*, vol. 77, no. 11, pp. 1605–1607, 2000.

[152] T. Sebastian, K. Schultheiss, B. Obry, B. Hillebrands, and H. Schultheiss, "Micro-focused brillouin light scattering: imaging spin waves at the nanoscale," *Frontiers in Physics*, vol. 3, p. 35, 2015.

[153] V. E. Demidov, S. Urazhdin, E. R. J. Edwards, M. D. Stiles, R. D. McMichael, and S. O. Demokritov, "Control of magnetic fluctuations by spin current," *Phys. Rev. Lett.*, vol. 107, p. 107204, Sep 2011.

[154] V. E. Demidov, S. Urazhdin, B. Divinskiy, V. D. Bessonov, A. B. Rinkevich, V. V. Ustinov, and S. O. Demokritov, "Chemical potential of quasi-equilibrium magnon gas driven by pure spin current," *Nature Communications*, vol. 8, Nov. 2017.

[155] W. Wettling, M. Cottam, and J. Sandercock, "The relation between one-magnon light scattering and the complex magneto-optic effects in yig," *Journal of Physics C: Solid State Physics*, vol. 8, no. 2, p. 211, 1975.

[156] R. Elliott and R. Loudon, "The possible observation of electronic raman transitions in crystals," *Physics Letters*, vol. 3, no. 4, pp. 189 – 191, 1963.

[157] E. C. Le Ru and P. G. Etchegoin, "Quantifying sers enhancements," *MRS Bulletin*, vol. 38, no. 8, 2013.

[158] E. L. Ru and P. Etchegoin, "Rigorous justification of the e4 enhancement factor in surface enhanced raman spectroscopy," *Chemical Physics Letters*, vol. 423, no. 1, pp. 63 – 66, 2006.

[159] M. Pelton, "Modified spontaneous emission in nanophotonic structures," *Nature Photonics*, vol. 9, pp. 427–435, 2015.

[160] E. Le Ru and P. G Etchegoin, "Surface-enhanced raman scattering (sers) and surface-enhanced fluorescence (sef) in the context of modified spontaneous emission," 10 2005.

[161] V. Amendola, R. Pilot, M. Frasconi, O. M. Maragò, and M. A. Iatì, "Surface plasmon resonance in gold nanoparticles: a review," *Journal of Physics: Condensed Matter*, vol. 29, p. 203002, apr 2017.

[162] L. Novotny, "Effective wavelength scaling for optical antennas," *Phys. Rev. Lett.*, vol. 98, p. 266802, Jun 2007.

[163] W. L. Johnson, S. A. Kim, Z. N. Utegulov, J. M. Shaw, and B. T. Draine, "Optimization of arrays of gold nanodisks for plasmon-mediated brillouin light scattering," *The Journal of Physical Chemistry C*, vol. 113, no. 33, pp. 14651–14657, 2009.

[164] A. L. Moretti, W. M. Robertson, B. Fisher, and R. Bray *Phys. Rev. B*, vol. 31, pp. 3361–3368, Mar 1985.

[165] T. Itoh, V. Biju, M. Ishikawa, Y. Kikkawa, K. Hashimoto, A. Ikehata, and Y. Ozaki, "Surface-enhanced resonance raman scattering and background light emission coupled with plasmon of single ag nanoaggregates," *The Journal of chemical physics*, vol. 124, no. 13, p. 134708, 2006.

[166] M. Noginov, G. Zhu, M. Bahoura, J. Adegoke, C. Small, B. Ritzo, V. Drachev, and V. Shalaev, "The effect of gain and absorption on surface plasmons in metal nanoparticles," *Applied Physics B*, vol. 86, no. 3, pp. 455–460, 2007.

[167] A. Akimov, A. Mukherjee, C. Yu, D. Chang, A. Zibrov, P. Hemmer, H. Park, and M. Lukin, "Generation of single optical plasmons in metallic nanowires coupled to quantum dots," *Nature*, vol. 450, no. 7168, pp. 402–406, 2007.

[168] P. Bharadwaj, P. Anger, and L. Novotny, "Nanoplasmonic enhancement of single-molecule fluorescence," *Nanotechnology*, vol. 18, no. 4, p. 044017, 2006.

[169] P. Johansson, H. Xu, and M. Käll, "Surface-enhanced raman scattering and fluorescence near metal nanoparticles," *Physical Review B*, vol. 72, no. 3, p. 035427, 2005.

[170] M. Gadenne, V. Podolskiy, P. Gadenne, P. Sheng, and V. Shalaev, "Plasmon-enhanced absorption by optical phonons in metal-dielectric composites," *EPL (Europhysics Letters)*, vol. 53, no. 3, p. 364, 2001.

[171] M. S. Anderson, "Surface enhanced infrared absorption by coupling phonon and plasma resonance," *Applied Physics Letters*, vol. 87, no. 14, p. 144102, 2005.

[172] V. E. Ferry, L. A. Sweatlock, D. Pacifici, and H. A. Atwater, "Plasmonic nanostructure design for efficient light coupling into solar cells," *Nano letters*, vol. 8, no. 12, pp. 4391–4397, 2008.

[173] G. Armelles, A. Cebollada, A. García-Martín, and M. U. González, "Magnetoplasmonics: Combining magnetic and plasmonic functionalities," *Advanced Optical Materials*, vol. 1, no. 1, pp. 10–35, 2013.

[174] I. D. et al, "Magneto-optical plasmonic heterostructure with ultranarrow resonance for sensing applications," *Scientific Reports*, vol. 6, no. 28077, 2016.

[175] S. D. Pappas, P. Lang, T. Eul, M. Hartelt, A. García-Martín, B. Hillebrands, M. Aeschlimann, and E. Papaioannou, "Broadband enhancement of the magneto-optical activity of hybrid au loaded bi:yig," 05 2019.

[176] N. Sousa, L. S. Froufe-Pérez, J. Sáenz, and A. García-Martín, "Magneto-optical activity in high index dielectric nanoantennas," *Scientific Reports*, vol. 6, 05 2016.

[177] J. e. a. Chin, "Nonreciprocal plasmonics enables giant enhancement of thin-film faraday rotation," *Nature Comms*, 2013.

[178] V. e. a. Belotelov, "Enhanced magneto-optical effects in magnetoplasmonic crystals," *Nature Nanotechnology*, 2011.

[179] K. e. a. Uchida, "Generation of spin currents by surface plasmon resonance," *Nature Comms*, 2015.

[180] I. Maksymov, "Magneto-plasmonics and resonant interaction of light with dynamic magnetisation in metallic and all-dielectric nanostructures (review)," *Nanomaterials*, vol. 5, 02 2015.

[181] H. Chang, L. Peng, W. Zhang, T. Liu, A. Hoffmann, L. Deng, and M. Wu, "Nanometer-thick yttrium iron garnet films with extremely low damping," *IEEE Magnetics Letters*, vol. 5, 2014.

[182] P. B. Johnson and R. W. Christy, "Optical constants of the noble metals," *Phys. Rev. B*, vol. 6, pp. 4370–4379, Dec 1972.

[183] S. K. Bandyopadhyay and A. K. Pal, "The effect of grain boundary scattering on the electron transport of aluminium films," *Journal of Physics D Applied Physics*, vol. 12, pp. 953–959, June 1979.

[184] H. Brune, "Microscopic view of epitaxial metal growth: nucleation and aggregation," *Surface Science Reports*, vol. 31, no. 4, pp. 125 – 229, 1998.

[185] H. Brune *Physics Today*, vol. 46, no. 11, 1993.

[186] J. J, H. Harutyunyan, D. Rosenmann, R. Divan, P. Wiederrecht, and S. Gray, "When are surface plasmon polaritons excited in the kretschmann-raether configuration?," *Scientific Reports*, vol. 5, 2015.

[187] J. D. Kraus and R. J. Marhefka, *Antennas*. McGraw-Hill Higher Education, 3 ed., 2001.

[188] S. Mubeen, S. Zhang, N. Kim, S. Lee, S. Krämer, H. Xu, and M. Moskovits, "Plasmonic properties of gold nanoparticles separated from a gold mirror by an ultrathin oxide," *Nano Letters*, vol. 12, no. 4, pp. 2088–2094, 2012.

[189] V. E. Demidov, S. O. Demokritov, D. Birt, B. O'Gorman, M. Tsoi, and X. Li, "Radiation of spin waves from the open end of a microscopic magnetic-film waveguide," *Physical Review B*, vol. 80, no. 1, p. 014429, 2009.

[190] R. F. Milsom, N. Reilly, and M. Redwood, "Analysis of generation and detection of surface and bulk acoustic waves by interdigital transducers," *IEEE Transactions on Sonics Ultrasonics*, vol. 24, pp. 147–166, 1977.

[191] A. Hessel and A. A. Oliner, "A new theory of wood's anomalies on optical gratings," *Appl. Opt.*, vol. 4, pp. 1275–1297, Oct 1965.

[192] V. O. Byelobrov, T. L. Zinenko, K. Kobayashi, and A. I. Nosich, "Periodicity matters: Grating or lattice resonances in the scattering by sparse arrays of subwavelength strips and wires.," *IEEE Antennas and Propagation Magazine*, vol. 57, pp. 34–45, Dec 2015.

[193] A. Christ, S. G. Tikhodeev, N. A. Gippius, J. Kuhl, and H. Giessen, "Waveguide-plasmon polaritons: Strong coupling of photonic and electronic resonances in a metallic photonic crystal slab," *Phys. Rev. Lett.*, vol. 91, p. 183901, Oct 2003.

[194] B. e. a. Luk-yanchuk, "The fano resonance in plasmonic nanostructures and metamaterials," *Nature Materials*, vol. 9, pp. 707–715, 2010.

[195] K. Lodewijks, J. Ryken, W. Van Roy, G. Borghs, L. Lagae, and P. Van Dorpe, "tuning the fano resonance between localized and propagating surface plasmon resonances for refractive index sensing applications," *Plasmonics*, vol. 8, pp. 1379–1385, 2013.

[196] C. O. Avci, K. Garello, A. Ghosh, M. Gabureac, S. F. Alvarado, and P. Gambardella, "Unidirectional spin hall magnetoresistance in ferromagnet/normal metal bilayers," *Nature Physics*, vol. 11, no. 7, pp. 570–575, 2015.

[197] C. O. Avci, J. Mendil, G. S. Beach, and P. Gambardella, "Origins of the unidirectional spin hall magnetoresistance in metallic bilayers," *Physical review letters*, vol. 121, no. 8, p. 087207, 2018.

[198] S. R. Boona, R. C. Myers, and J. P. Heremans, "Spin caloritronics," *Energy & Environmental Science*, vol. 7, no. 3, pp. 885–910, 2014.

[199] K. Olejník, V. Novák, J. Wunderlich, and T. Jungwirth, "Electrical detection of magnetization reversal without auxiliary magnets," *Physical Review B*, vol. 91, no. 18, p. 180402, 2015.

[200] K. Yasuda, A. Tsukazaki, R. Yoshimi, K. Takahashi, M. Kawasaki, and Y. Tokura, "Large unidirectional magnetoresistance in a magnetic topological insulator," *Physical review letters*, vol. 117, no. 12, p. 127202, 2016.

[201] K. Yasuda, A. Tsukazaki, R. Yoshimi, K. Kondou, K. Takahashi, Y. Otani, M. Kawasaki, and Y. Tokura, "Current-nonlinear hall effect and spin-orbit torque magnetization switching in a magnetic topological insulator," *Physical review letters*, vol. 119, no. 13, p. 137204, 2017.

[202] Y. Lv, J. Kally, D. Zhang, J. S. Lee, M. Jamali, N. Samarth, and J.-P. Wang, "Unidirectional spin-hall and rashba- edelstein magnetoresistance in topological insulator-ferromagnet layer heterostructures," *Nature communications*, vol. 9, no. 1, pp. 1–7, 2018.

[203] C. Luo, L. Sun, Y. Zhang, H. Huang, M. Yang, Y. Zhai, J. Du, and H. Zhai, "Investigations of magnetic properties of tb-doped ni78fe22 thin films," *physica status solidi c*, vol. 9, no. 1, pp. 81–84, 2012.

[204] W. Bailey, P. Kabos, F. Mancoff, and S. Russek, "Control of magnetization dynamics in ni/sub 81/fe/sub 19/thin films through the use of rare-earth dopants," *IEEE transactions on magnetics*, vol. 37, no. 4, pp. 1749–1754, 2001.

[205] E. Ryan and J. Katine, "Enhanced magnetic damping in spin-transfer excitation," in *APS Meeting Abstracts*, 2005.

[206] V. Demidov, S. Urazhdin, A. Zholud, A. Sadovnikov, and S. Demokritov, "Nanoconstriction-based spin-hall nano-oscillator," *Applied Physics Letters*, vol. 105, no. 17, p. 172410, 2014.

[207] V. Demidov, H. Ulrichs, S. Gurevich, S. Demokritov, V. Tiberkevich, A. Slavin, A. Zholud, and S. Urazhdin, "Synchronization of spin hall nano-oscillators to external microwave signals," *Nature communications*, vol. 5, no. 1, pp. 1–6, 2014.

[208] V. Demidov, S. Urazhdin, A. Zholud, A. Sadovnikov, A. Slavin, and S. Demokritov, "Spin-current nano-oscillator based on nonlocal spin injection," *Scientific reports*, vol. 5, p. 8578, 2015.

[209] A. Giordano, M. Carpentieri, A. Laudani, G. Gubbiotti, B. Azzerboni, and G. Finocchio, "Spin-hall nano-oscillator: A micromagnetic study," *Applied Physics Letters*, vol. 105, no. 4, p. 042412, 2014.

[210] V. E. Demidov, S. Urazhdin, H. Ulrichs, V. Tiberkevich, A. Slavin, D. Baither, G. Schmitz, and S. O. Demokritov, "Magnetic nano-oscillator driven by pure spin current," *Nature materials*, vol. 11, no. 12, pp. 1028–1031, 2012.

[211] T. Sebastian, T. Brächer, P. Pirro, A. Serga, B. Hillebrands, T. Kubota, H. Naganuma, M. Oogane, and Y. Ando, "Nonlinear emission of spin-wave caustics from an edge mode of a microstructured co 2 mn 0.6 fe 0.4 si waveguide," *Physical review letters*, vol. 110, no. 6, p. 067201, 2013.

[212] K. Vogt, F. Fradin, J. Pearson, T. Sebastian, S. Bader, B. Hillebrands, A. Hoffmann, and H. Schultheiss, "Realization of a spin-wave multiplexer," *Nature communications*, vol. 5, no. 1, pp. 1–5, 2014.

[213] S.-K. Kim, K.-S. Lee, and D.-S. Han, "A gigahertz-range spin-wave filter composed of width-modulated nanostrip magnonic-crystal waveguides," *Applied Physics Letters*, vol. 95, no. 8, p. 082507, 2009.

[214] A. Chumak, V. Vasyuchka, A. Serga, and B. Hillebrands, "Magnon spintronics," *Nature Physics*, vol. 11, no. 6, pp. 453–461, 2015.

[215] A. Khitun, M. Bao, and K. L. Wang, "Spin wave magnetic nanofabric: A new approach to spin-based logic circuitry," *IEEE Transactions on Magnetics*, vol. 44, no. 9, pp. 2141–2152, 2008.

[216] G. Csaba, Á. Papp, and W. Porod, "Perspectives of using spin waves for computing and signal processing," *Physics Letters A*, vol. 381, no. 17, pp. 1471–1476, 2017.

[217] T. Brächer and P. Pirro, "An analog magnon adder for all-magnonic neurons," *Journal of Applied Physics*, vol. 124, no. 15, p. 152119, 2018.

[218] M. Zahedinejad, A. A. Awad, S. Muralidhar, R. Khymyn, H. Fulara, H. Mazraati, M. Dvornik, and J. Åkerman, "Two-dimensional mutual synchronization in spin hall nano-oscillator arrays," *arXiv preprint arXiv:1812.09630*, 2018.

[219] M. Dvornik, A. A. Awad, P. Dürrenfeld, A. Houshang, E. Iacocca, R. K. Dumas, and J. Åkerman, "Mutually synchronized spin hall nano-oscillators for neuromorphic computing (conference presentation)," in *Spintronics X*, vol. 10357, p. 103572J, International Society for Optics and Photonics, 2017.

[220] V. Demidov, S. Urazhdin, B. Divinskiy, V. Bessonov, A. Rinkevich, V. Ustinov, and S. Demokritov, "Chemical potential of quasi-equilibrium magnon gas driven by pure spin current," *Nature communications*, vol. 8, no. 1, pp. 1–7, 2017.

[221] J. Yun, Y. Zuo, J. Mao, M. Chang, S. Zhang, J. Liu, and L. Xi, "Lowering critical current density for spin-orbit torque induced magnetization switching by ion irradiation," *Applied Physics Letters*, vol. 115, no. 3, p. 032404, 2019.

[222] A. Hirohata, "Book review: Spin current," *Frontiers in Physics*, vol. 6, p. 23, 2018.

[223] D. C. Ralph and M. D. Stiles, "Spin transfer torques," *Journal of Magnetism and Magnetic Materials*, vol. 320, no. 7, pp. 1190–1216, 2008.

[224] H. Zabel and M. Farle, *Magnetic nanostructures: spin dynamics and spin transport*, vol. 246. Springer, 2012.

[225] S. Bonetti, V. Tiberkevich, G. Consolo, G. Finocchio, P. Muduli, F. Mancoff, A. Slavin, and J. Åkerman, "Experimental evidence of self-localized and propagating spin wave modes in obliquely magnetized current-driven nanocontacts," *Physical review letters*, vol. 105, no. 21, p. 217204, 2010.

[226] B. Divinskiy, S. Urazhdin, S. O. Demokritov, and V. E. Demidov, "Controlled nonlinear magnetic damping in spin-hall nano-devices," *Nature communications*, vol. 10, no. 1, pp. 1–7, 2019.

[227] A. Slavin and V. Tiberkevich, "Spin wave mode excited by spin-polarized current in a magnetic nanocontact is a standing self-localized wave bullet," *Physical review letters*, vol. 95, no. 23, p. 237201, 2005.

[228] *Nonlinear Schrodinger Equation from Wikipedia.*